

The Pennsylvania State University  
The Graduate School  
Eberly College of Science

PHOSPHOLIPID HEAD GROUPS AND INTERACTIONS WITH TRANSITION METAL  
IONS

A Dissertation in  
Chemistry

by  
Anne Sendeki

© 2017 Anne Sendeki

Submitted in Partial Fulfillment  
of the Requirements  
for the Degree of  
Doctor of Philosophy

August 2017

The dissertation of Anne Sendecki was reviewed and approved\* by the following:

Paul S. Cremer

Professor of Chemistry, Biochemistry and Molecular Biology

Dissertation Advisor

Chair of Committee

Christine D. Keating

Professor of Chemistry

Alexey Silakov

Assistant Professor of Chemistry

Peter J. Butler

Professor of Biomedical Engineering

Associate Dean for Education in the College of Engineering

Thomas E. Mallouk

Head of the Chemistry Department

Evan Pugh University Professor of Chemistry, Biochemistry and Molecular Biology,  
Physics, and Engineering Science and Mechanics

\*Signatures are on file in the Graduate School

## ABSTRACT

Herein, the biophysical properties of lipid head groups is explored, with a focus on the effects of specific binding of transition metal ions  $\text{Ni}^{2+}$ ,  $\text{Cu}^{2+}$ , and  $\text{Zn}^{2+}$ . First, we incorporate high amounts of phosphatidylethanolamine (PE) into supported lipid bilayers (SLBs), which has proven historically difficult. Under certain conditions, interesting phase behavior such as domains formed from two-component systems or three-dimensional tubules are observed. Then, binding of  $\text{Ni}^{2+}$  and  $\text{Cu}^{2+}$  to deprotonated amines in the PE head groups is measured in microfluidic devices by fluorescence quenching. As copper is redox active, the effect of  $\text{Cu}^{2+}$ -PE on the oxidation of membrane species is explored, which could be important for neurodegenerative diseases. Next, we hypothesized that metal ion complexes with phosphatidylserine (PS) would disrupt domain formation. PS is a negatively charged lipid and has been shown to have tight binding with  $\text{Cu}^{2+}$  that does not change the net charge on the membrane, while  $\text{Zn}^{2+}$  interacts electrostatically with the phosphate and carboxylate moieties. While binding of  $\text{Cu}^{2+}$  seems to have no effect on PS domains, high concentration of  $\text{Zn}^{2+}$  appears to stabilize the domains. Another objective of this work was to clarify the mechanism of molecular chemotaxis to direct the motion of bulk lipid vesicles. These results suggest the roles of lipid head groups are diverse and varied, and are compounded by interactions with divalent transition metal ions.

## TABLE OF CONTENTS

LIST OF FIGURES .....	vi
LIST OF TABLES .....	xi
ACKNOWLEDGEMENTS .....	xii
Chapter 1 Introduction .....	1
Role of Phospholipids .....	1
Homogeneous and Heterogeneous Assays .....	3
Measuring Diffusion within a SLB .....	4
Metal Quenching Assays .....	5
Effect of Head Groups on Lipid Domain Formation .....	7
Chemotaxis of Vesicles for Drug Delivery Purposes .....	9
Chapter 2 Supported Lipid Bilayers with Phosphatidylethanolamine .....	10
Introduction .....	10
Materials and Methods .....	13
Results .....	17
POPE Bilayers at 23 °C .....	17
POPE Bilayers at 37 °C .....	21
DLPE Bilayers .....	22
Ni <sup>2+</sup> Binding Assay .....	23
Discussion .....	24
Supporting Figures .....	26
Chapter 3 Copper Binds to PE and Increases Lipid Oxidation .....	29
Introduction .....	29
Materials and Methods .....	30
Results .....	33
Dissociation Constant and Quenching Efficiency of Cu <sup>2+</sup> –PE .....	33
Membrane Species are Oxidized More Rapidly in the Presence of Cu <sup>2+</sup> –PE Complexes ..	37
Discussion .....	39
Chapter 4 Effect of Metal-Lipid Complexes on Lipid Domains Containing Phosphatidylserine	41

Introduction.....	41
Materials and Methods.....	44
Results.....	46
Cu <sup>2+</sup> -PS: SANS and DSC .....	46
Cu <sup>2+</sup> and Zn <sup>2+</sup> have Different Effects on PS Monolayers .....	49
Zn <sup>2+</sup> -PS: DSC.....	51
Discussion .....	53
Chapter 5 Chemotaxis of Small Molecules .....	58
Introduction.....	58
Materials and Methods.....	60
Results.....	63
Chemotaxis Counteracts Diffusion .....	63
Directed Chemotactic Migration.....	65
Chemotactic Determination of Binding Constants .....	66
No Chemotaxis Observed with Vesicle-Small Molecule Systems .....	67
Discussion .....	69
Chapter 6 Conclusions .....	72
References.....	74

## LIST OF FIGURES

Figure 1-1. Schematic of a SLB. Glass is a common choice for the support, and the thin water layer acts as a lubricant between the glass and the lipids. Bilayer height depends on the identity of the lipids, but is typically 40-50 Å.....	2
Figure 1-2. Head group structures of the relevant phospholipids and the fluorescent dye most commonly employed herein. R represents a carbon chain, or lipid tail, which can vary in length and sites of unsaturation.....	3
Figure 1-3. Representative FRAP curve of a 99.5 mol% POPC, 0.5 mol% TR-DHPE SLB. The images on the left show the bleach spot right after exposure to the laser (top), and the bilayer after recovery (bottom), where the dark line across the images is a scratch in the bilayer, where bilayer material was removed to create contrast. The graph on the right shows the normalized fluorescence recovery fit to a single exponential. ....	5
Figure 1-4. Metals bind to lipid head groups and quench nearby fluorophores. A) Divalent cations such as Cu <sup>2+</sup> and Ni <sup>2+</sup> can form lipid-metal complexes which can quench fluorophores through an energy transfer mechanism. This provides a label-free measurement of metals binding to the SLB. B) Fluorescence images of SLBs in microfluidic channels in the absence and presence on 100 μM Cu <sup>2+</sup> . The channel containing POPE is quenched when Cu <sup>2+</sup> is added, as can be seen in the linescans. C) Fluorescent linescans corresponding to the red dashed lines in the fluorescent images. Scale bar = 100 μm. ....	7
Figure 1-5. Lateral segregation of a SLB into liquid-ordered and liquid-disordered domains. The liquid-ordered domain is enriched in cholesterol and saturated lipids, and has tighter packing and slower diffusion. Liquid-disordered domains are enriched in unsaturated lipids and are similar to fluid phase SLBs. ....	8
Figure 2-1. Comparison of PC and PE lipids with schematic representations of the resulting supported lipid constructs for different lipids of interest at room temperature. A) Headgroup structures of PC and PE. B) Cylindrical PC lipids form fluid supported lipid bilayers. C) Lipids with high negative curvature such as DOPE form hexagonal phase structures. D) PE lipids with less curvature, such as POPE or DLPE, can form fluid supported lipid bilayers when mixed with small amounts of PC lipids, allowing for Ni <sup>+</sup> binding assays to be performed. ....	12
Figure 2-2. FRAP curves for two lipid compositions at 23 °C and 37 °C. A) Bilayers were formed with 0 mol% POPE, 99.5 mol% POPC and 0.5 mol% TR-DHPE. B) Bilayers were formed with 70 mol% POPE, 29.5 mol% POPC, and 0.5 mol% TR-DHPE. Lines are single exponential fits to the data. ....	17
Figure 2-3. Diffusivity of supported lipid bilayers containing POPE and POPC analyzed by FRAP at 23 °C and 37 °C. A) Mobile fraction. B) Diffusion coefficient.....	18

Figure 2-4. Fluorescent images of POPE-containing SLBs with oil-immersion 100x objective. As the amount of POPE is increased, the number of defects increased. The bright spot indicated by the arrow in the 50 mol% image is an unruptured vesicle, and the dark patch indicated by the arrow in the 70 mol% image is a liquid-ordered phase domain. For other mol% POPE SLBs, see Figure 2-9. ....	19
Figure 2-5. An extended-time FRAP study of 80 mol% POPE bilayers. A) Fluorescence images of the bilayer before bleaching, just after bleaching, after 4.5 hrs, and after 20 hrs. The bleached area is highlighted with a red circle. B) The corresponding FRAP recovery curve. The $D_{\text{recovery}}$ values were calculated from the initial rise ( $t=0-5$ hrs) and $D_{\text{decay}}$ from the subsequent decrease ( $t > 5$ hrs) in fluorescence intensity. Inset. Fluorescent image of tubules approximately 5 $\mu\text{m}$ above the surface. Arrows point out tubules that are bent so that they are more fully in the focal plane, other bright spots represent tubules extending through the focal plane. Scale bar = 10 $\mu\text{m}$ . ....	20
Figure 2-6. Properties of supported lipid bilayers with mixed DLPE and DLPC lipids at room temperature and physiological temperature as a function of DLPE concentration. A) Mobile fraction. B) Diffusion coefficient. ....	22
Figure 2-7. A) $\text{Ni}^{2+}$ binding titration curve measured at room temperature in 10 mM Tris buffer at pH 8.5 to 50 mol% POPE bilayer. B) Representation of $\text{Ni}^{2+}$ binding to two deprotonated PE head groups. Bivalent binding is expected at this density of PE. <b>Error! Bookmark not defined.</b> ....	24
Figure 2-8. (Top) Fluorescence image of a 70 mol% POPE SLB imaged with a 100x objective. The green box indicates the area of the SLB analyzed in the bottom image. (Bottom) Histogram of fluorescence showing three distinct regions. The blue line in the histogram indicates the fluorescence level of the scratch region, where no bilayer material is present. The large peak in the histogram reflects the intensity of the nearby bilayer, where the liquid-ordered domains are colored orange (top and bottom) and the surrounding liquid-disordered phase is grey. From the relative difference in fluorescence between the blue and orange regions, it is clear that the orange spots in the top image are liquid-ordered domains, and not holes in the bilayer .....	26
Figure 2-9. Images of POPE/POPC SLBs under two different magnifications (top, 10x; bottom, 100x). Dark lines are from scratches made with tweezers to remove lipid bilayer material and create contrast. ....	26
Figure 2-10. Fluorescent images of SLBs of various mol% of POPE that were formed at either 23 $^{\circ}\text{C}$ or 37 $^{\circ}\text{C}$ . The bilayers formed at 23 $^{\circ}\text{C}$ had more visible defects than those formed at 37 $^{\circ}\text{C}$ . Dark lines are scratches made by tweezers removing bilayer material to create contrast. ....	28
Figure 2-11. Comparison of two different fluorophores at room temperature and 37 $^{\circ}\text{C}$ in a POPC bilayer. Both probes used showed a significant increase in diffusion coefficient with the increase in temperature. ....	28

Figure 3-1. Schematic illustration of  $\text{Cu}^{2+}$  binding to the amine moieties on PE head groups. Once bound,  $\text{Cu}^{2+}$  participates in Fenton-like chemistry to produce ROS such as hydroxyl radicals and superoxide, which can oxidize double bonds within the membrane. .... 30

Figure 3-2. Normalized fluorescence intensity (Norm. Fluor.) from SLBs containing 0 to 70 mol % POPE with increasing concentrations of  $\text{Cu}^{2+}$ . The squares are data points and the solid curves represent least-squares fits to Langmuir isotherms. The error bars represent standard deviations from 6 independent measurements. .... 34

Figure 3-3. (A) Normalized fluorescence intensity from SLBs containing 70 mol% POPE, 29.5 mol% POPC, and 0.5 mol% TR-DHPE from pH 7.0 to 10.0. (B) Normalized fluorescence intensity from SLBs containing 0 to 70 mol% POPE at pH 10.0. The solid lines in each graph represent least-squares fits to a Langmuir isotherm. The error bars represent standard deviations from 6 independent measurements. .... 35

Figure 3-4. Fluorescence recovery after photobleaching data (FRAP) for 0-70 mol% POPE in POPC containing 0.5 mol% TR-DHPE at pH 10. The left graph shows the mobile fraction of each bilayer, whereas the graph on the right contains the measured diffusion coefficients. .... 37

Figure 3-5. Fluorescent images taken under 20x magnification of 70 mol% POPE, 29.5 mol% POPC, 0.5 mol% TR-DHPE bilayers. A) pH 7.4 clearly shows lateral phase segregation. B) pH 10 is absent of phase segregation. The dark lines are scratches made by tweezers to remove bilayer material to provide contrast. Scale bars = 50  $\mu\text{m}$ . .... 37

Figure 3-6. Fluorescence emission spectra of C11-BODIPY in lipid vesicle solutions composed of (A) 99.5 mol % POPC and 0.5% C11-BODIPY and (B) 70 mol % POPE, 29.5% POPC, and 0.5 mol % C11-BODIPY. The black lines represent fluorescence spectra taken immediately after the addition of 10 mM  $\text{H}_2\text{O}_2$  and 70  $\mu\text{M}$   $\text{Cu}^{2+}$ , while the red lines are from fluorescence spectra after 15 min have elapsed. .... 38

Figure 3-7. Change in the area of the 594 nm peak (Normalized A594) as a function of time for the conditions provided in the key. The  $\text{Cu}^{2+}$  and  $\text{H}_2\text{O}_2$  concentrations were 70  $\mu\text{M}$  and 10 mM, respectively, when these species were present. .... 39

Figure 4-1. Schematic of lipid domains within a membrane. Top shows phase segregation with cholesterol and lipids with saturated tails closely packed in the liquid ordered domains, and lipids with unsaturated tails in the liquid disordered domains. Middle shows a possible result of binding a divalent cation to the negatively charged PS head groups, which could shrink the size of the ordered domains. Bottom shows an alternative result that changes the partitioning coefficient of the PS lipids to the different domains, causing the ordered domains to enlarge. .... 43

Figure 4-2. Schematic showing the tuning of H/D ratio to customize what is measured using SANS. Differences in the scattering length density (SLD) give rise to signal, so in an ideal lipid mixing without domains, the three areas: head group, tails, and solvent, can be tuned to match each other. This is akin to heating the samples to melt the domains, and no signal should be seen at higher

temperatures. When there is phase separation, the different regions each have their own SLD, giving rise to signal. Adapted from Reference 86. .... 45

Figure 4-3. SANS intensity that comes from lateral scattering, i.e. domains, after subtraction of other contributions (see Figure S3), as a function of copper concentration. The physical length scales reflected by this spectra go from 6 nm ( $q = 0.1 \text{ \AA}^{-1}$ ) to 60 nm ( $q = 0.01 \text{ \AA}^{-1}$ ). The lipid composition in all samples is shown on the right. .... 48

Figure 4-4. DSC results of the same sample composition used in the SANS experiments as a function of copper concentration. The corresponding melting temperatures are shown in Table 4-1 below. .... 49

Figure 4-5.  $\pi$ -A diagram of a Langmuir monolayer compression study of DLPS (12:0, 12:0) at an air-water interface in the presence of different divalent cations. The dashed blue line shows the approximate pressure of a lipid bilayer. All were done with 10 mM Tris and 100 mM NaCl at pH 7.4. .... 50

Figure 4-6. DSC peaks showing the melting of DPPS:DOPC:chol in the presence of  $\text{Zn}^{2+}$ . A) At lower concentrations of zinc, more heat is required to melt the domains and no significant change in melting temperature is observed. B) At 2:1 PS: $\text{Zn}^{2+}$  concentrations, there is a second peak at higher temperature that emerges. The red lines represent the overall fit and the two individual peak fits. .... 51

Figure 4-7. DSC results for the PC control for the same concentrations of zinc. Similarly, there is an increase in heat needed to melt the domains, but there is no second peak evident at the highest concentrations of zinc. .... 52

Figure 4-8. DSC results showing the melting of domains with DPPC:DOPS:chol, where PS is now localized in the liquid disordered domains. There is not much difference from when it was in the liquid ordered domains. .... 53

Figure 4-9. SANS data of domains with no metal ions added. The decrease in overall intensity from 20 °C to 60 °C represents the demixing of domains, which results in an SLD designed to match the SLD of the solvent, giving less scattering. .... 56

Figure 4-10. SANS data for the  $\text{Cu}^{2+}$  series at both 20 °C and 60 °C, shown with the y-axis in log scale. The leftover scattering shown at 60 °C, at which the domains should be melted and therefore the intensity theoretically 0, is due to experimental error resulting in slight SLD mismatch between the various regions. The subtraction of which is shown in Figure 4-11 below. .... 56

Figure 4-11. Subtraction of the leftover scattering at 60 °C from the total scattering at 20 °C to find the scattering from lateral phase segregation due to domains that are present at 20 °C but not at 60 °C. The resulting data (blue line) is what is plotted in Figure 4-3. .... 57

Figure 4-12. Summary of enthalpy data measured by DSC for the three different lipid compositions. All were normalized so that the  $\Delta H$  without divalent cations is equal to 0. The y-axis represents the % increase in  $\Delta H$  that resulted from addition of zinc. .... 57

Figure 5-1. Schematic illustration of the reversible binding between ZnTSPP and imidazole inducing chemotaxis. A) Structures of ZnTSPP and imidazole, and the axial ligation. B) Schematic representation of the chemotaxis. An imidazole concentration gradient induces movement of the ZnTSPP up that concentration gradient to maximize binding interactions. .... 60

Figure 5-2. Proof of concept experimental setup and results. A) Diagram of three-inlet microfluidic channel. In this experiment, ZnTSPP was introduced into the center channel with or without imidazole. The resulting fluorescence line profiles show the position of the ZnTSPP in the channel, which is 234  $\mu\text{m}$  wide. Dashed line indicates the position of the maximum fluorescence intensity within the channel. B) The initial line profiles with or without imidazole are identical, proving the experimental conditions are kept constant. C) Near the outlet of the channel, the black line profile of the ZnTSPP alone has broadened significantly due to Fickian diffusion. The red line profile shows that in the presence of imidazole, diffusion occurs to a lesser extent, indicating an opposing chemotactic force. .... 64

Figure 5-3. Collective migrations of 10  $\mu\text{M}$  ZnTSPP in the presence of 100  $\mu\text{M}$  imidazole. The line profiles are measured near the outlet of the channel. A) Imidazole was introduced into the left inlet, and the ZnTSPP shifts to the left. B) Imidazole was introduced into the right inlet, making ZnTSPP shift to the right. .... 65

Figure 5-4. A) Plots of mean normalized fluorescence intensity profiles as a function of the lateral position along the width of the channel show shifts for 10  $\mu\text{M}$  ZnTSPP toward increasing concentrations of imidazole. B) Net chemotaxis shift of the peak maxima in A from the center of the channel as a function of the concentration of imidazole. The line is a fit to a Langmuir binding isotherm..... 66

Figure 5-5. Vesicle binding system did not exhibit chemotaxis. A) Schematic illustration of ibuprofen binding to a POPC vesicle. B) Fluorescence images of a two-inlet microfluidic device. Vesicles were introduced into the left inlet, and buffer or ibuprofen was introduced in the right inlet, but did not change the fluorescence. Top. Image taken near the inlets and junction. Bottom. Image taken near the outlet of the channel. C) Fluorescence line profiles taken in the presence and absence of ibuprofen at the position of the red lines drawn in B. Top. Line profiles from near the inlet. Bottom. Line profiles taken near the outlet. .... 68

## LIST OF TABLES

Table 2-1. Summary of ATR-FTIR results of three high mole percentage POPE bilayers. Bilayers were formed using chain perdeuterated POPE, where the saturated tail was deuterated and the unsaturated tail was hydrogenated. The theoretical percentage of IR signal was calculated considering the full structures of both POPC and POPE, as well as the relative amounts of each. The vesicles were introduced and incubated into the cell, and the signal was recorded to obtain a “bulk” reading. Then the excess vesicles were flushed out and the reading taken again, this time only measuring what was left on the surface. These experiments were conducted on separate bilayers at two different temperatures.....	27
Table 4-1. Gel-to-liquid phase transition temperatures of the individual lipid components used in this study. ....	46
Table 4-2. Melting temperatures obtained from DSC fits to the data shown in Figure 4.4. The slight decrease in $T_m$ is not necessarily significant, given the low signal to noise.....	49
Table 4-3. Summary of melting temperatures of different vesicle compositions in the presence of $Zn^{2+}$ as measured by DSC. All lipid molar ratios were 1:1:1. ....	55

## ACKNOWLEDGEMENTS

Many people contributed to the work that went into this thesis. First, I would like to thank Dr. Matthew Poyton, Dr. Halil Okur, and Dr. Kelvin Rembert, for years of support, advice, and example. Next, Simou Sun, Saranya Pullanchery, Virginia Greenberger, and Brad Rogers, for being wonderful friends and coworkers, and for going above and beyond and actually reading parts of this thesis. Thank you for your patience, your feedback, and your willingness to go get ice cream with me. I'd also like to thank Alexis Baxter, Dr. Shengyuan Deng, and Codey Henderson, for being terrific coauthors. Seung-Yi Lee, Dr. Xiao Cong, Dr. Tao Zhao, and Yi-Ting Liao, thank you and I hope to see you all again one day. A big thank you to Dana Hosko for doing everything we ask for, and an even bigger thanks for Dr. Tinglu Steve Yang, for challenging me and supporting me in equal parts, and for teaching me how to mispronounce various Chinese words. Thank you to everyone else in the Cremer group, and of course, my advisor Dr. Cremer, who made all of this possible.

I would also like to acknowledge the support of my family and friends. My parents, Carol and Leon, for always being there when I needed you, and my brothers, Matt and Lee, for never asking me a science question. Thank you to my friends, especially the ones who visited me here in the middle of nowhere, whether for tailgates, Galentine's Day, or just for mimosas. And thank you to everyone else, everyone who was ever proud of me or thought what I was doing was cool, because it helped. Couldn't have done it without you.

## Chapter 1 Introduction

### Role of Phospholipids

Phospholipids are more than passive, structural components of cell membranes. They are involved in a variety of cellular processes, such as apoptotic signaling,<sup>1</sup> fission and fusion,<sup>2</sup> and organization of membrane proteins,<sup>3</sup> depending on their head group chemistries or number of sites of unsaturation within the lipid tails. While biochemical assays can determine if the lipid of interest plays a part in a process, it can be difficult to isolate what that role is and what is happening at a mechanistic level.<sup>4</sup> To better understand their individual contributions, researchers have turned to simple model systems to eliminate the biological complexity of the plasma membrane.<sup>5,6</sup>

Commonly used model systems include vesicles or liposomes,<sup>6,7</sup> supported lipid bilayers,<sup>5,8,9</sup> black lipid membranes,<sup>10</sup> and lipid monolayers,<sup>11,12</sup> each system offering its own particular advantages. The Cremer group specialized in making supported lipid bilayers (SLBs) via the vesicle fusion method,<sup>7,13</sup> and has used these extensively in microfluidic devices to measure binding of ions,<sup>14,15</sup> small molecules,<sup>16</sup> and proteins<sup>17,18</sup> to lipid bilayers (Figure 1-1). This is done by making vesicles of the desired composition, often incorporating a separate fluorescent tag for label-free measurement, and then exposing vesicle solution to a clean and smooth piece of glass.<sup>9</sup> The vesicles will spontaneously rupture to carpet the glass, forming a SLB that, when kept hydrated, can be stable for days.<sup>19</sup> In addition to being easy to make and to customize their lipid composition, they maintain the two-dimensional fluidity of a cell membrane, thanks to a thin water layer between the underlying support and the bilayer.<sup>20</sup> This is crucial as many processes either involve multivalent binding to two or more lipids or somehow cause a reordering of lipids within the bilayer.<sup>14,20</sup>

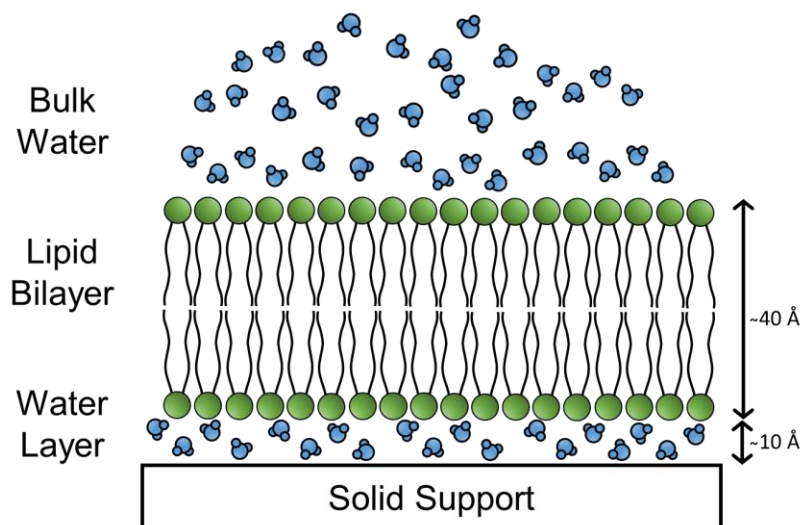


Figure 1-1. Schematic of a SLB. Glass is a common choice for the support, and the thin water layer acts as a lubricant between the glass and the lipids. Bilayer height depends on the identity of the lipids, but is typically 40-50 Å.

The relevant lipid head group structures are shown in Figure 1-2. Phosphatidylcholine (PC) is the most abundant phospholipid in eukaryotic cells and is zwitterionic.<sup>4</sup> Phosphatidylethanolamine (PE) is also zwitterionic but has a primary amine, which can act as a hydrogen bond donor.<sup>21</sup> It has also been known as a nonbilayer lipid, as it can form curved structures more readily than other lipids.<sup>22</sup> Phosphatidylserine (PS) is negatively charged and preferentially located on the inner leaflet of the plasma membrane, and is known to flip to the outer leaflet to signal for clearance of apoptotic cells by macrophages.<sup>1</sup> Finally, Texas Red DHPE is a fluorophore covalently bound to a PE lipid head group, and can be used as a reporter for interactions at the membrane surface.<sup>14,15</sup>

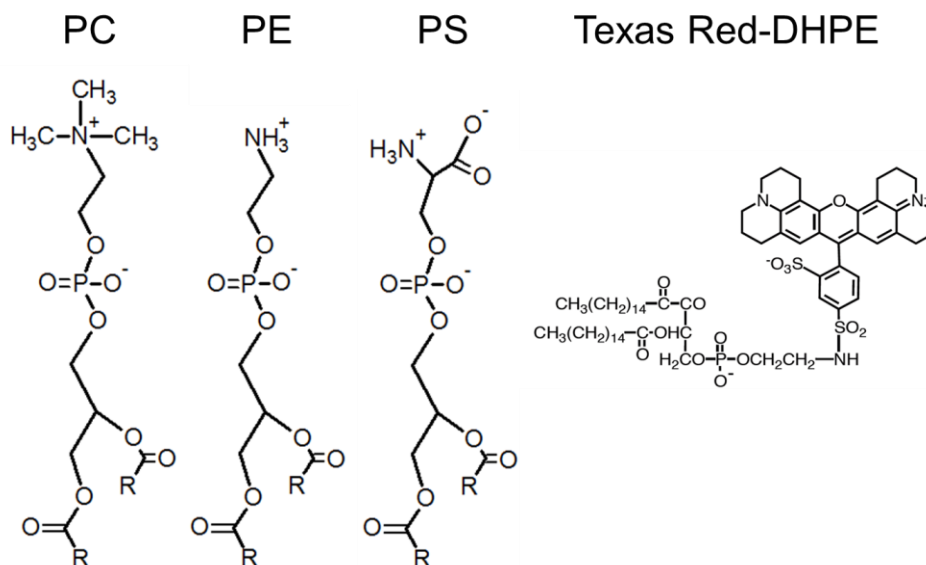


Figure 1-2. Head group structures of the relevant phospholipids and the fluorescent dye most commonly employed herein. R represents a carbon chain, or lipid tail, which can vary in length and sites of unsaturation.

## Homogeneous and Heterogeneous Assays

SLB model systems present several important advantages over lipid vesicle model systems. Foremost, SLBs in microfluidic devices allow for heterogeneous analysis, in which solutions containing analyte are flowed over the bilayer. Therefore, multiple solutions can be introduced sequentially to the same surface using the same equipment, reducing experimental variation and amount of sample needed.<sup>14</sup> It is also possible to measure different compositions of lipids and/or analytes in channels side-by-side, making direct comparisons fast and simple.<sup>20</sup> Continuous flow of fresh solution eliminates the need to calculate the concentrations of “free” and “bound” analyte, as is necessary with vesicle systems.<sup>20</sup> Vesicle experiments are homogeneous assays, which require higher sample volumes, are incompatible with sequential assays, contain populations of multilamellar vesicles,<sup>6</sup> and can be unstable depending on the lipid composition.<sup>23</sup>

SLBs offer other advantages in addition to those associated with heterogeneous assays. An important one is that the glass substrate mimics the cell cytoskeleton, and therefore the lateral

diffusion of lipids in an SLB is similar to the diffusion of lipids in a live cell,<sup>24</sup> while diffusion in vesicles is much faster. Similarly, the curvature of a cell is often better mimicked by an SLB, as they are both relatively flat and vesicles are highly curved. The curvature of the membrane can be very important for multivalent binding of an analyte to the surface.<sup>5</sup> Giant unilamellar vesicles (usually  $\mu\text{m}$  diameters) obviate this problem, but lack the advantages of heterogeneous assays. Finally, SLBs are compatible with other techniques besides fluorescence, such as atomic force microscopy and sum frequency generation spectroscopy.<sup>8</sup> These surface-specific techniques are incompatible with vesicle model systems.

#### Measuring Diffusion within a SLB

Fluorescence Recovery after Photobleaching (FRAP) is a technique used to measure the fluidity of a SLB.<sup>25,26</sup> Developed by Axelrod et. al. in the 1970s, it provides two quantitative measures of fluidity: the mobile fraction, or how much of the bilayer is able to laterally diffuse, and the diffusion coefficient, which represents how quickly the diffusion occurs (Figure 1-3). The experiment is done by focusing a small laser spot on a SLB and photobleaching a fraction of the fluorophores in that area. Fluorescence images are taken over time as the bleached fluorophores diffuse out of the area and other, unbleached fluorophores take their place, due to Brownian diffusion in two dimensions. The fluorescence of the bleached spot is normalized according to the equation:

$$F(t) = \frac{F_t - F_0}{1 - F_0}$$

where  $F_t$  is the fluorescence at time  $t$  and  $F_0$  is the fluorescence right after photobleaching. When plotted over time, a typical recovery curve like the one in Figure 1-3 is obtained (black squares). FRAP data can be fit to various models, and Figure 1-3 shows a fit to a simple single exponential,

which allows for an empirical approximation of the mobile fraction,  $a$ , and the time constant,  $b$ , used to calculate the amount of time it takes to recover halfway,  $t_{1/2}$ , and from that the diffusion coefficient,  $D$ . Mobile fractions of well-formed SLBs are typically around  $0.95 \pm 0.03$ . Diffusion coefficients are dependent on the fluorophore used, but are typically in the range of  $1\text{--}3 \mu\text{m}^2/\text{s}$  for fluid SLBs. Decreases and deviations from these typical values can indicate the formation of lipid phase domains, an increase presence of unruptured vesicles or other defects, or if the bilayer is in the gel phase. Chapter 2 details the effects of increasing the amount of PE head groups on the fluidity of the bilayer, which give rise to these inhomogeneities.

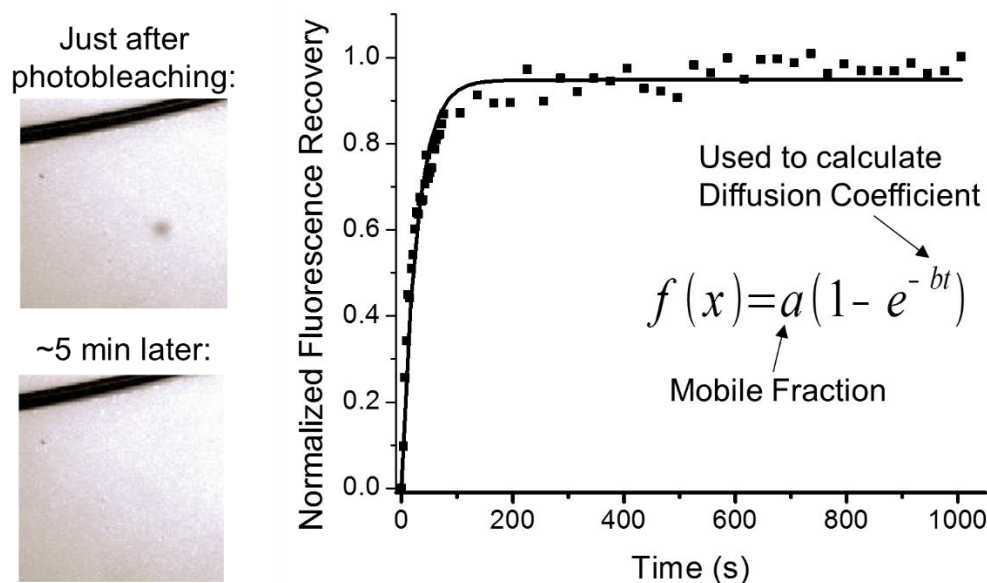


Figure 1-3. Representative FRAP curve of a 99.5 mol% POPC, 0.5 mol% TR-DHPE SLB. The images on the left show the bleach spot right after exposure to the laser (top), and the bilayer after recovery (bottom), where the dark line across the images is a scratch in the bilayer, where bilayer material was removed to create contrast. The graph on the right shows the normalized fluorescence recovery fit to a single exponential.

### Metal Quenching Assays

Another fluorescence technique used extensively in our group takes advantage of fluorescence quenching observed by many transition metal ions.<sup>27</sup> As shown in Figure 1-4A, the

formation of a metal-lipid complex on the surface of the bilayer can quench nearby fluorophores through an energy transfer mechanism. The binding is usually pH dependent, as the divalent cation binds to deprotonated amine moieties on the PS<sup>14,15</sup> or PE<sup>28</sup> lipid head groups. Binding experiments are conducted with SLBs formed in microfluidic channels as seen in Figure 1-4B, which shows side by side microfluidic channels with different lipid compositions, one containing 70 mol% PE, 29.5 mol% PC, and 0.5 mol% Texas Red DHPE, and the other containing only 99.5 mol% PC and 0.5 mol% Texas Red DHPE. When no copper is added and only buffer is flowing over the bilayers, both the SLBs have high fluorescence (Figure 1-4C, black line). When they are both exposed to 100  $\mu\text{M}$   $\text{Cu}^{2+}$ , there is a slight decrease in fluorescence of the channel containing PE (red line). This strategy was used to measure binding constants of copper to PE at different pH values, and is described in depth in Chapter 3. It also explores how the binding of copper, a redox active metal, could affect the rate of membrane oxidation, which could be important in various neurodegenerative diseases.

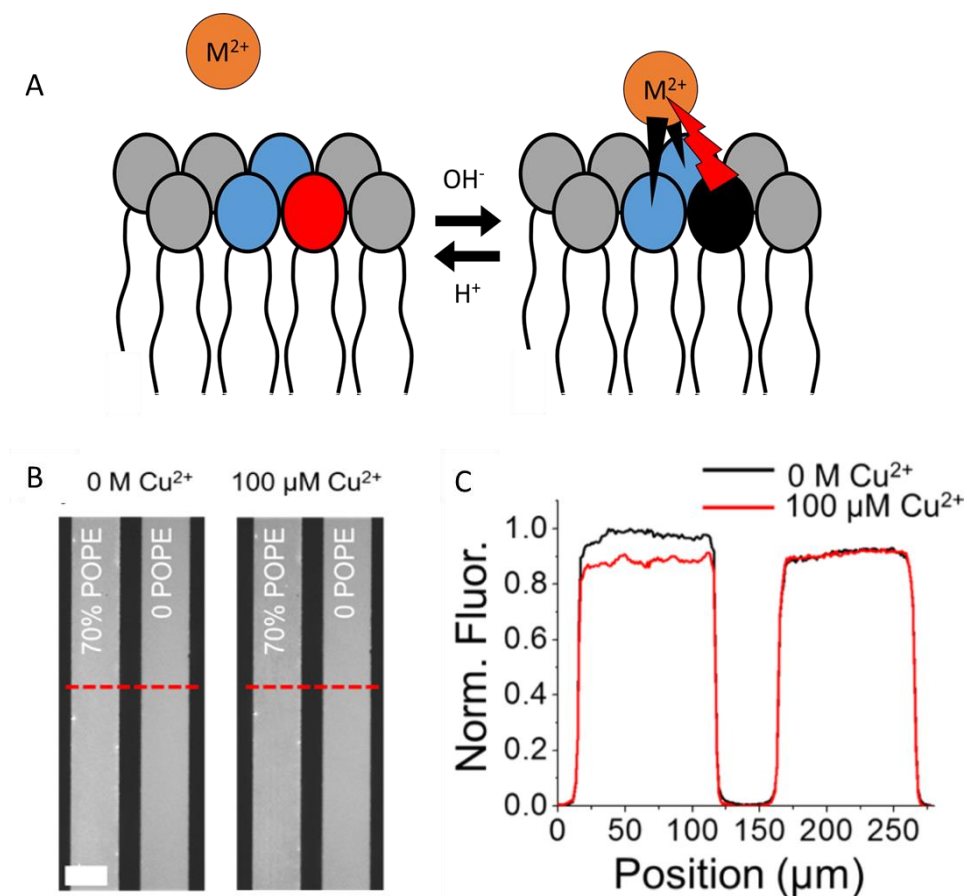


Figure 1-4. Metals bind to lipid head groups and quench nearby fluorophores. A) Divalent cations such as  $Cu^{2+}$  and  $Ni^{2+}$  can form lipid-metal complexes which can quench fluorophores through an energy transfer mechanism. This provides a label-free measurement of metals binding to the SLB. B) Fluorescence images of SLBs in microfluidic channels in the absence and presence on 100  $\mu M$   $Cu^{2+}$ . The channel containing POPE is quenched when  $Cu^{2+}$  is added, as can be seen in the linescans. C) Fluorescent linescans corresponding to the red dashed lines in the fluorescent images. Scale bar = 100  $\mu m$ .

### Effect of Head Groups on Lipid Domain Formation

Binding interactions between divalent cations and lipid head groups may also be important to the formation of lipid domains.<sup>29</sup> Lipid domains, or lipid rafts, are a controversial topic among the biophysical membrane community.<sup>30</sup> They have been extensively studied and documented in model systems, but existence, size, and lifetime *in vivo* is still disputed.<sup>31,32</sup> They are thought to be important organizers of lipids and protein in biological membranes.<sup>3</sup> In model systems, they are formed from mixing a gel phase lipid, a fluid phase lipid, and cholesterol, and the resulting SLB

is laterally separated into domains of different phases<sup>31</sup> (Figure 1-5). The gel phase lipid, which usually has saturated lipid tails, and the cholesterol preferentially partition into the liquid-ordered domains. The lipids pack together more tightly, slowing down the diffusion by roughly an order of magnitude from a fluid phase bilayer. The fluid phase lipid usually has sites of unsaturation within the lipid tails, and so partitions into the liquid-disordered domains. These diffuse much the same as a homogeneous fluid phase bilayer. Indeed, the identity of the lipid tails appear to dominate the phase behavior, and the effect of lipid head group is less well understood.

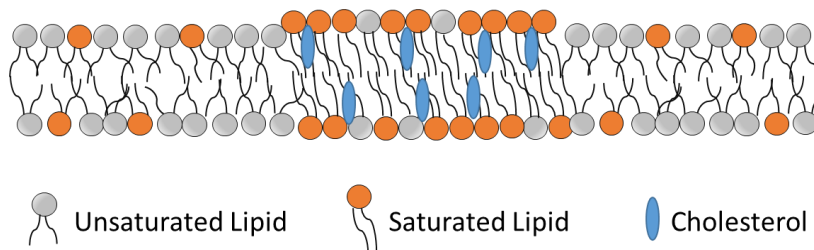


Figure 1-5. Lateral segregation of a SLB into liquid-ordered and liquid-disordered domains. The liquid-ordered domain is enriched in cholesterol and saturated lipids, and has tighter packing and slower diffusion. Liquid-disordered domains are enriched in unsaturated lipids and are similar to fluid phase SLBs.

Some work has been done to explore the effect of varying the head groups. In switching from PC to PS, the domain formation becomes salt dependent, as the electrostatic repulsions between the negative charges on PS resist the tighter packing of a liquid-ordered domain.<sup>33</sup> Others have shown that the presence of millimolar concentrations of calcium can induce domain formation with PS head groups, by electrostatically binding to the phosphate groups of neighboring lipids and gluing them together.<sup>29,34,35</sup> We hypothesized that the tighter binding of  $\text{Cu}^{2+}$ -PS complex, which can have apparent dissociation constants as tight as picomolar, depending on PS concentration,<sup>14,15</sup> could have a stronger effect than  $\text{Ca}^{2+}$ . This is the focus of Chapter 4. The effect of zinc on PS-containing domains is also investigated.  $\text{Zn}^{2+}$  is similar to  $\text{Cu}^{2+}$  in that it is a first

row transition metal ion, but it has a full  $d^{10}$  shell, and so behaves more like  $\text{Ca}^{2+}$ .<sup>36</sup> Instead of using fluorescence techniques, small angle neutron scattering (SANS) and differential scanning calorimetry (DSC) were used on bulk vesicle systems to study the effect of divalent cations on PS-containing domains.

### Chemotaxis of Vesicles for Drug Delivery Purposes

Chapter 5 moves away from studying the biophysical properties of lipid head groups, and instead treats bilayers as a material. Bilayers are well-suited for biosensors, due to their biocompatibility, customizability, and resistance to biofouling, and have been used by our group and others for these purposes.<sup>8,37</sup> More recently, these qualities have made them an attractive option for drug delivery vehicles, mimicking cellular endosomes and vesicles used as transport within cells.<sup>38</sup> A general motif encapsulates the drug inside a vesicle, which can be decorated to include proteins or linkers to help target the vesicle. Then a stimulus can be applied, such as heat, to release the contents of the vesicle when it arrives at the desired site.<sup>39</sup> Chapter 5 reports efforts to use small molecule chemotaxis to direct the movement of vesicles, and includes a proof of concept study using a separate zinc porphyrin system. While the chemotaxis of the porphyrin system represents an exciting step towards understanding the mechanism of molecular chemotaxis, the difficulties translating this to a system with a direct application highlights the work still left to be done.

## Chapter 2 Supported Lipid Bilayers with Phosphatidylethanolamine

### Introduction

The headgroup structure of phospholipids is one of the main factors that determines their biological role and function. The zwitterionic phospholipids, phosphatidylethanolamine (PE) and phosphatidylcholine (PC), have almost identical structures, except for the methylation of the amine (Figure 2-1A), which leads to significant differences in their respective behaviors.<sup>4</sup> While PC has been known as a relatively inert lipid, PE can act as a hydrogen bond donor and its amine can be deprotonated, giving it unique interactions, not only with other bilayer components,<sup>21</sup> but with ions and molecules from the bulk solution.<sup>28</sup> PE also has intrinsic curvature, which affects its role within biological membranes as a stabilizer of membrane proteins.<sup>40</sup> Despite these unique interactions, PC, being easier to work with, has historically been used as the predominate phospholipid in model system studies, and has even been used as a substitute for PE or treated as interchangeable with PE.<sup>41,42,43</sup> This has unfortunately limited the information available about PE's biophysical properties.

PE is the second most abundant phospholipid in eukaryotic cells, representing 25 mol% of the overall lipid content and can comprise up to 45 mol% of the phospholipids in nervous tissue.<sup>44,45</sup> It is also the most abundant phospholipid in many bacteria, primarily Gram negative bacteria, where it makes up 70-80 mol% of membrane lipids.<sup>4,46</sup> It has various biological functions, such as serving as a protein cofactor<sup>46,47</sup> and as an accessory for protein folding.<sup>42</sup> It has also been shown to bind to copper ions, which can enhance the rate of lipid oxidation.<sup>28</sup> Due to its biological importance and abundance, creating model lipid bilayer systems that contain physiologically relevant concentrations of PE would be very advantageous. While it is possible to make spherical lipid vesicles that contain a high mol% of PE, they are typically unstable and likely to precipitate

out of solution in a matter of hours or days.<sup>28,48</sup> Using a second type of model membrane system, the supported lipid bilayer (SLB), could obviate this complication. Creating fluid SLBs with high, physiologically relevant concentrations of PE lipids, however, has been a challenge. For example, Hamai et. al. demonstrated that using 20 mol% or more of a PE lipid, 1,2-dioleoyl-*sn*-glycero-3-phosphoethanolamine (DOPE), in supported bilayers also containing 1,2-dioleoyl-*sn*-glycero-3-phosphocholine (DOPC), led to incomplete bilayer formation.<sup>49</sup>

Forming stable SLBs via the vesicle fusion method depends upon the intrinsic curvature of the individual lipids.<sup>49</sup> Many phospholipids, such as PC, have two tails and an overall cylindrical shape, and can readily form planar bilayers (Figure 2-1B). Typical intrinsic curvature values for PC are close to 0 nm<sup>-1</sup>. In fact, DOPC is 0.1 nm<sup>-1</sup>,<sup>50</sup> and 1-palmitoyl-2-oleoyl-*sn*-glycero-3-phosphocholine (POPC)<sup>50</sup> as well as 1,2-dilauroyl-*sn*-glycero-3-phosphocholine (DLPC) are exactly 0.0 nm<sup>-1</sup>.<sup>51</sup> By contrast, PE has a significantly smaller headgroup (Figure 2-1A, right), giving it a more conical shape. The intrinsic curvature is -0.4 nm<sup>-1</sup> for DOPE<sup>50</sup> and -0.3 nm<sup>-1</sup> for both 1-palmitoyl-2-oleoyl-*sn*-glycero-3-phosphoethanolamine (POPE)<sup>50</sup> and 1,2-dilauroyl-*sn*-glycero-3-phosphoethanolamine (DLPE).<sup>52</sup>

The negative curvature of PE lipids leads to unique phase behavior that is not observed with PC lipids. Specifically, the addition of double bonds into the alkyl chains of PE lipids leads to a conically-shaped molecule that will not readily assemble into a planar sheet (lamellar phase), due to the strain introduced by the curvature of each lipid (Figure 2-1C).<sup>49</sup> Instead, a hexagonal phase is often favored in which the head groups face toward the center and the tails are splayed outward. PE lipids undergo a transition from the lamellar to the hexagonal phase at a temperature dependent on the length of the tails and the number of sites of unsaturation.<sup>22</sup> For example, DOPE, which has two 18:1 lipid tails, has a hexagonal phase transition temperature,  $T_h$ , of 10 °C.

Therefore, it is not possible to form a homogeneous supported lipid bilayer at room temperature with physiologically relevant amounts of DOPE. By contrast, POPE (16:0, 18:1) and DLPE (12:0, 12:0), which contain 1 and 0 sites of unsaturation, respectively, have gel-to-liquid phase transition temperatures ( $T_m$ ) at 25 °C and 29 °C,<sup>53</sup> and  $T_h$  temperatures of 70 °C and 130 °C<sup>54</sup>, respectively. As such, they are significantly better candidates to form planar lipid bilayers. Herein, we show that fluid SLBs containing up to 70 mol% POPE in POPC or 50 mol% DLPE in DLPC can be made at room temperature. Moreover, fluid SLBs containing 90 mol% of these PE lipids in PC can be assembled at 37 °C. Finally, a fluorescence assay to measure nickel binding was performed with 50 mol% POPE in the bilayer (Figure 2-1D). It was found that  $\text{Ni}^{2+}$  bound to POPE with an apparent dissociation constant,  $K_D$ , value of 0.38 mM. This value is several orders of magnitude tighter than this same transition metal ion interacts with PC lipids.

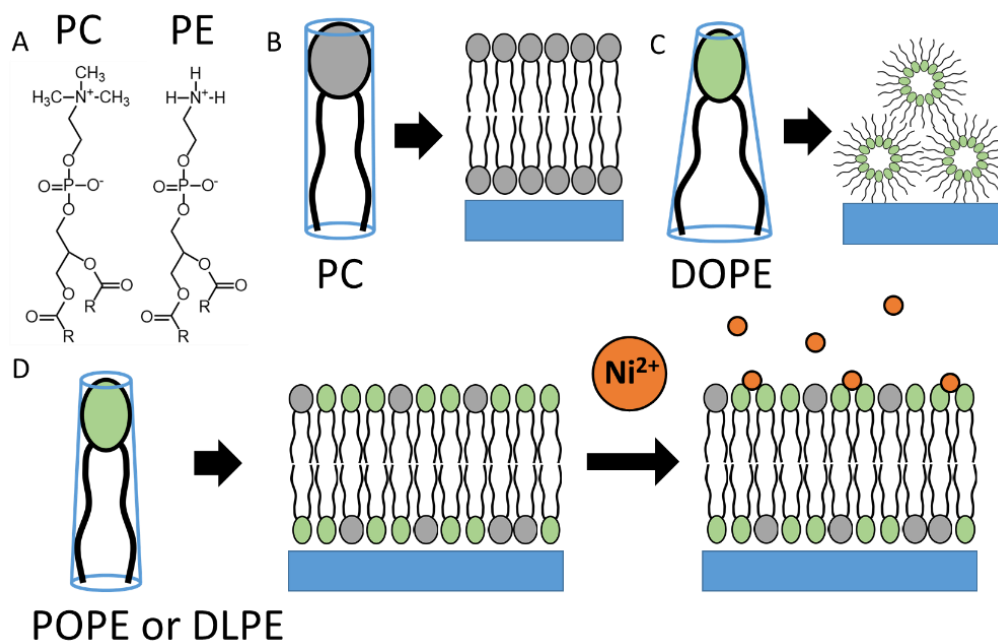


Figure 2-1. Comparison of PC and PE lipids with schematic representations of the resulting supported lipid constructs for different lipids of interest at room temperature. A) Headgroup structures of PC and PE. B) Cylindrical PC lipids form fluid supported lipid bilayers. C) Lipids with high negative curvature such as DOPE form hexagonal phase structures. D) PE lipids with less curvature, such as POPE or DLPE, can form fluid supported lipid bilayers when mixed with small amounts of PC lipids, allowing for  $\text{Ni}^{2+}$  binding assays to be performed.

## Materials and Methods

### ***Materials***

All phospholipids were purchased from Avanti Polar Lipids (Alabaster, AL). Texas Red 1,2-dihexadecanoyl-*sn*-glycero-3-phosphoethanolamine, triethylammonium salt (Texas Red DHPE) was purchased from Life Technologies (Grand Island, NY). Poly(dimethylsiloxane) (PDMS) was obtained from Dow Corning (Sylgard, silicone elastomer-184).

### ***Lipid Vesicle Preparation***

Small unilamellar vesicles (SUVs) were made by the freeze-thaw extrusion method.<sup>7,13</sup> Briefly, the lipids were mixed at the desired ratio in chloroform, dried with nitrogen, and then placed under vacuum for 1.5 hrs. The lipid film was rehydrated to a density of 1 mg/mL in aqueous buffer containing 10 mM dibasic sodium phosphate and 100 mM NaCl at pH 7.4 and sonicated for 20 min. They were then subjected to ten freeze-thaw cycles and extruded through a filter with 100 nm pores. Vesicles containing 70 mol% PE or higher were extruded at ~40 °C to ensure they were in the fluid phase. Vesicles containing less than 25 mol% PE were able to be stored at 4 °C, and vesicles containing 25 mol% or more were stored at room temperature. All vesicles were used within 7 days of preparation.

### ***SLB Formation***

SLBs were formed in PDMS wells on borosilicate glass (Fisher Scientific, Pittsburgh, PA). The glass was first cleaned in a detergent solution of 1:7 7X (BP Biomedicals) and 18.2 MΩ water, rinsed copiously with 18.2 MΩ water, dried with compressed nitrogen gas, and finally annealed at

530 °C for 5 hrs. This preparation rendered the glass surface hydrophilic. A well was made by sticking a reusable PDMS ring onto the clean and annealed glass. To form an SLB, 75  $\mu$ L of the vesicle solution was added and incubated for 20 min before rinsing excess vesicles away using 18.2 M $\Omega$  water.

### ***Temperature Control***

For experiments conducted at 37 °C, a programmable temperature controller (VWR) was employed directly on the microscope stage to heat the glass slide, which served as an underlying substrate for the bilayer. The temperature was monitored on the side of the glass opposite to the bilayer. Vesicles were added to preheated wells and incubated while heated, then rinsed with heated 18.2 M $\Omega$  water. The well was finally covered with a glass coverslip to prevent evaporation and the temperature was allowed to re-equilibrate for 20 min before being used.

### ***Fluorescence Recovery after Photobleaching (FRAP)***

FRAP<sup>25,26</sup> experiments were carried out with a Nikon Eclipse TE-2000-U inverted microscope through a 10x objective. A 532 nm 300 mW solid state laser (Dragon Lasers) was used to bleach Texas Red-DHPE with a power averaging 5 mW for 1 s at the sample. The average diameter of the laser beam was 20  $\mu$ m, giving 0.016 mW/ $\mu$ m<sup>2</sup>/s as the power per unit area. The average fluorescence intensity of the spot was analyzed over time as the bleached fluorophores diffused out and unbleached fluorophores took their place. Images were initially taken every 3 seconds, until the fluorescence in the bleached area no longer visually appeared to change, and then the time interval was switched to every 30 or 60 seconds to minimize photobleaching. The fluorescence of

the bleached spot was normalized to an unbleached reference spot, and the percentage recovery was plotted over time after photobleaching,

$$F(t) = \frac{F_t - F_0}{1 - F_0}$$

where  $F_t$  is the normalized fluorescence at time  $t$ , and  $F_0$  is the normalized fluorescence at  $t = 0$ .

The results were fit to a single exponential:

$$y = A(1 - e^{-bx})$$

where  $A$  corresponds to the mobile fraction (i.e. percentage of the bilayer able to recover) and  $b$  was used to calculate the diffusion coefficient  $D$  (how quickly the bilayer recovered):

$$\tau_{1/2} = \frac{\ln(2)}{b} \quad D = \frac{w^2}{4\tau_{1/2}} * \gamma$$

where  $w$  is the diameter of the laser beam and  $\gamma = 0.88$ .

### ***Attenuated Total Reflection Infrared Spectroscopy***

Corroborating data using attenuated total reflection infrared spectroscopy (ATR-IR) was taken to confirm that the SLBs contained similar amounts of POPE and POPC to the corresponding vesicles used in their formation. Briefly, chain perdeuterated POPE (d31-palmitoyl) was mixed with POPC and used to make vesicles as described above. The vesicles were then injected into a home-built ATR flow cell, and formed a SLB on a silicon wafer. IR spectra were taken before and after rinsing away the excess bulk vesicles, and the relative signal from the CD and CH stretch regions was compared against their expected ratio in the vesicles to determine if the bilayer formed had the intended composition.

### ***Nickel Titration Measurements***

Microfluidic devices were assembled with PDMS/glass composite as described in previous publications.<sup>17</sup> 10  $\mu$ L of the desired vesicle solution was introduced into each microfluidic channel and incubated for 30 min. Buffer containing 10 mM Tris and 100 mM NaCl at pH 8.5 was introduced into the channels first to rinse away the excess vesicles and this buffer was used throughout the experiment. Buffer with increasing concentrations of NiCl<sub>2</sub> was introduced through plastic tubing, with each solution given at least one hour to equilibrate before measuring the fluorescence. Then the tubing at the inlet was removed, drained of solution, and the next solution was drawn through, and the tubing reinserted. The background fluorescence was subtracted from the average fluorescence of each channel, and was normalized to the initial fluorescence before the addition of NiCl<sub>2</sub>. Due to significant collisional quenching of generic bilayers at millimolar concentrations of heavy metal cations, the fluorescence change from POPC bilayers was subtracted by adapted the Stern-Volmer equation to include both quenching contributions:

$$\frac{F_0^{total}}{F^{total}} = 1 + k_{binding}\tau_0[Ni^{2+} - PE] + k_{collisional}\tau_0[Ni^{2+}]$$

where  $F_0^{total}$  is the fluorescence intensity of the POPE bilayers with no added nickel,  $F^{total}$  is the fluorescence intensity in the presence of nickel,  $k_{binding}$  is the quencher rate coefficient due to Ni<sup>2+</sup>-PE binding,  $\tau_0$  is the fluorescence lifetime, and  $k_{collisional}$  is the quencher rate coefficient due to collisional quenching. Rearrangement of this equation allows for isolation of the quenching due to the Ni<sup>2+</sup>-PE complex, which can then be fit to a Langmuir isotherm to extract the  $K_D$ .

## Results

### *POPE Bilayers at 23 °C*

In a first set of experiments, we investigated SLBs formed by the vesicle fusion method at 23 °C that contained various concentrations of POPE in POPC. All membranes contained 0.5 mol% Texas Red 1,2-dihexadecanoyl-*sn*-glycero-3-phosphoethanolamine (TR-DHPE) to visualize the SLBs by epifluorescence microscopy. The SLBs were quantitatively analyzed by FRAP. Figure 2-2 shows representative FRAP curves for supported bilayers made with (A) 99.5 mol% POPC and with (B) 70 mol% POPE and 29.5 mol% POPC at both 23 °C and 37 °C. Without POPE, a single exponential offered a reasonable approximation to the fluorescence recovery curves at both temperatures. At 70 mol% POPE, however, the data diverged significantly from an exponential fit at room temperature, reflecting a decrease in homogeneity, but was improved at 37 °C, as will be discussed later.

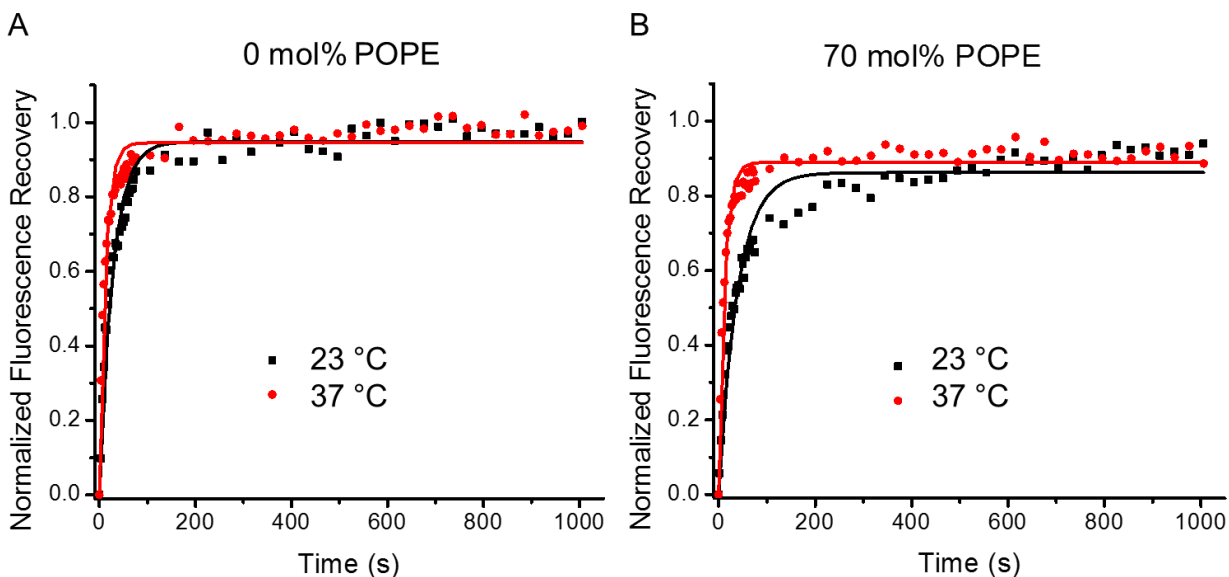


Figure 2-2. FRAP curves for two lipid compositions at 23 °C and 37 °C. A) Bilayers were formed with 0 mol% POPE, 99.5 mol% POPC and 0.5 mol% TR-DHPE. B) Bilayers were formed with 70 mol% POPE, 29.5 mol% POPC, and 0.5 mol% TR-DHPE. Lines are single exponential fits to the data.

FRAP results for POPE/POPC compositions ranging from 0 to 90 mol% PE are summarized in Figure 2-3. Both the fraction of mobile dye molecules in the membrane (A) and the associated diffusion constants (B) are provided. When mixed with POPC, which has a  $T_m$  of  $-2\text{ }^{\circ}\text{C}$ ,<sup>53</sup> supported lipid bilayers could be formed with an approximately 90% mobile dye fraction for PE content as high as 70 mol% at both 23 and 37  $^{\circ}\text{C}$ . Moreover, the dye molecules displayed diffusion constants near to or above  $2\text{ }\mu\text{m}^2/\text{sec}$  with up to 70 mol% POPE. Together, these metrics demonstrate that the supported bilayers were in the fluid phase with up to 70 mol% POPE.

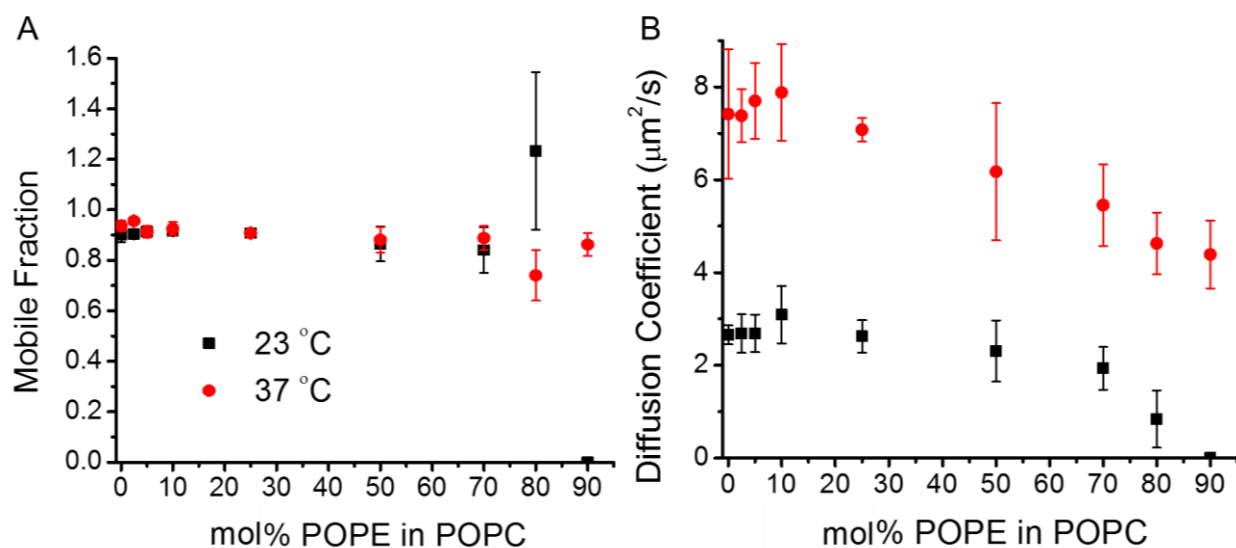


Figure 2-3. Diffusivity of supported lipid bilayers containing POPE and POPC analyzed by FRAP at 23  $^{\circ}\text{C}$  and 37  $^{\circ}\text{C}$ . A) Mobile fraction. B) Diffusion coefficient.

Under close inspection, it was possible to see small defects in the bilayer, such as unruptured vesicles, and these increased in number with increasing amounts of PE (Figure 2-4). At 70 mol% POPE, higher magnification revealed phase domain formation with characteristic domain sizes on the order of 1 micron in diameter (Figure 2-8). This was to be expected as Cannon

et. al., have shown the melting transition for vesicles composed of 70 mol% POPE and 30 mol% POPC is just below room temperature at 22 °C.<sup>28,55</sup>

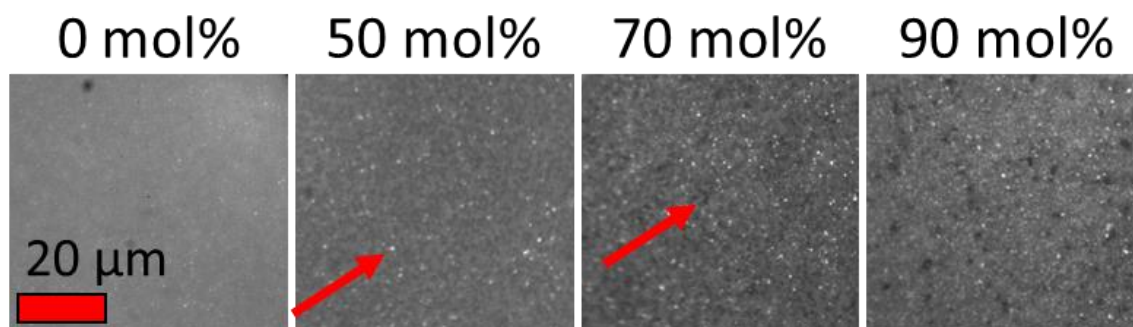


Figure 2-4. Fluorescent images of POPE-containing SLBs with oil-immersion 100x objective. As the amount of POPE is increased, the number of defects increased. The bright spot indicated by the arrow in the 50 mol% image is an unruptured vesicle, and the dark patch indicated by the arrow in the 70 mol% image is a liquid-ordered phase domain. For other mol% POPE SLBs, see Figure 2-9.

With 80 mol% POPE, the bilayers behaved more unusually, as reflected in their FRAP and ATR-IR data. The data at 80 mol% showed an apparent mobile fraction above 1 (Figure 2-3A). Such anomalous behavior arose because the dye molecule, TR-DHPE, was sequestered into small areas where it was highly concentrated, resulting in self-quenching.<sup>56</sup> When the bilayer was bleached, a fraction of the fluorophores were damaged and self-quenching was reduced, which allowed the bilayer to show recovery above 100% in the 4.5 hour image (Figure 2-5A). The over recovery occurred because the 80 mol% SLBs were inhomogeneous. Not only do they have domains, but high magnification revealed three-dimensional tubules extended out from the bilayer. These were highly curved structures with diameters below the diffraction limit of light that were anchored to the SLB at one end and extended several microns above the surface. POPE formed highly curved structures<sup>4</sup> and was presumed to be enriched in the tubules. This idea was supported by ATR-IR data (Table 2-1), which showed considerably less POPE than predicted at the surface, as the tubules extend beyond the penetration depth of the ATR measurement ( $\sim 0.35 \mu\text{m}$ ).

TR-DHPE is also known to prefer highly curved structures because of its bulky headgroup,<sup>57</sup> and the tubules were clearly visible against the SLB fluorescence from below (Figure 2-5B, inset). During FRAP, both the bilayer and the tubules were bleached simultaneously. As shown in Figure 2-5B, the initial increase and subsequent leveling off of the recovery curve was fit to extract the mobile fraction and diffusion coefficient reported in Figure 3, as this most closely reflects the diffusion of the lipids in the two-dimensional bilayer with domain structures. However, when monitored over much longer time periods, the fluorescence began to decrease again (20 hrs image in Figure 2-5A). In fact, the fluorescence attenuated by about one-third over a time scale of approximately 15 hours. This slower time constant most likely reflected diffusion of dye along the tubules in the z-direction. As the tubules extended approximately 20  $\mu\text{m}$  above the SLB, well outside of the microscope's depth of view ( $\sim 0.5 \mu\text{m}$ ), the dye needed to diffuse back to the surface through the tubules above. Indeed, the tubules acted as a sink for the dyes, requiring significantly more dye and longer times to reestablish self-quenching.

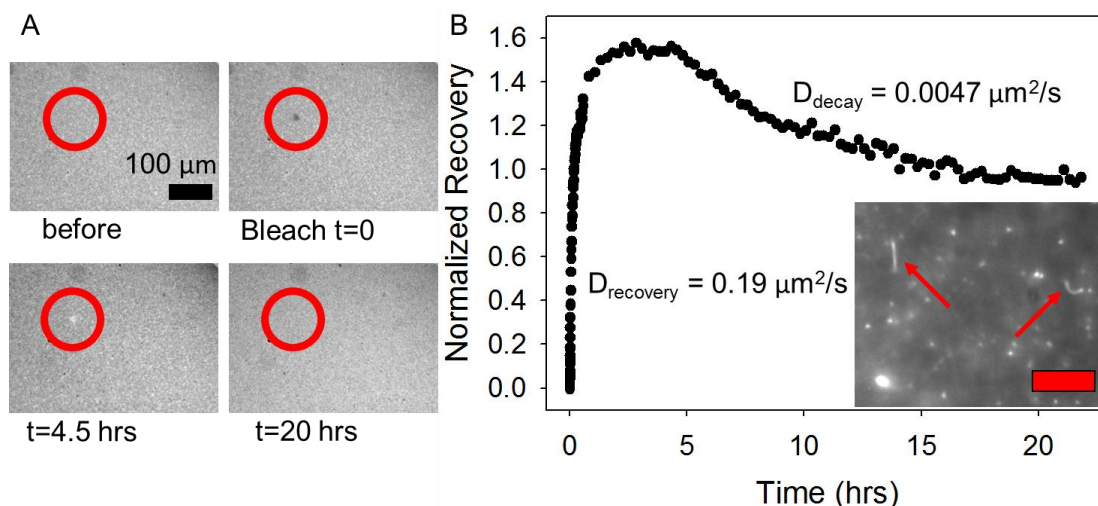


Figure 2-5. An extended-time FRAP study of 80 mol% POPE bilayers. A) Fluorescence images of the bilayer before bleaching, just after bleaching, after 4.5 hrs, and after 20 hrs. The bleached area is highlighted with a red circle. B) The corresponding FRAP recovery curve. The  $D_{\text{recovery}}$  values were calculated from the initial rise ( $t=0-5$  hrs) and  $D_{\text{decay}}$  from the subsequent decrease ( $t > 5$  hrs) in fluorescence intensity. Inset. Fluorescent image of tubules approximately 5  $\mu\text{m}$  above the surface. Arrows point out tubules that are bent so that they are more fully in the focal plane, other bright spots represent tubules extending through the focal plane. Scale bar = 10  $\mu\text{m}$ .

At 90 mol% POPE, the mobile fraction and diffusion coefficient were both zero at 23 °C (Figure 2-3). Under these circumstances, the level of fluorescence intensity from the surface was quite low. In fact, it does not appear that the surface was well-covered with bilayer material, (Figure 2-4) and the residual fluorescence arose from adhered vesicles. We also attempted to form bilayers with 99 mol% POPE and 1 mol% of a variety of other fluorophores. This was not possible due to poor incorporation of the fluorophores into the bilayer.

### ***POPE Bilayers at 37 °C***

Selecting tails for PE lipids that have less intrinsic negative curvature clearly increased the amount of PE that could be incorporated into fluid SLBs at room temperature. However, membranes formed with POPE lipids still have a relatively high  $T_m$  value. As such, one should expect to encounter issues with fluidity at higher PE concentrations when working at room temperature. Raising the temperature to 37 °C, which is above the  $T_m$  of POPE, should allow fluidity to be restored to the SLBs. Indeed, qualitatively, the visible defects and domains that appeared at room temperature were no longer evident or greatly reduced at 37 °C (Figure 2-10). Moreover, with 80 and 90 mol% PE, the bilayers started out with defects that annealed over time. The mobile fractions of the 37 °C bilayers were all at least slightly higher than the corresponding ones at room temperature (red data points, Figure 2-3). The only exception to this was 80 mol% POPE, which had a mobile fraction above 1 at 23 °C due to bilayer inhomogeneities. At 37 °C, they no longer showed over-recovery, and no tubules or domains were observed under these conditions. ATR-FTIR confirmed the lipid composition of the SLBs matched the nominal composition up to 90 mol%. (Table 2-1).

## DLPE Bilayers

To further explore the effects of unsaturation in lipid tails and corroborate the results seen with POPE SLBs, we conducted FRAP experiments using DLPE, which eliminated all double bonds and had phase transition temperatures comparable to POPE.<sup>53</sup> Generally, similar results were seen with DLPE as for POPE (Figure 2-6). The SLBs maintained high mobility and diffusion coefficients with up to 50 mol% PE at 23 °C, while higher mol% PE exhibited defects and irreproducibility. At 37 °C, the DLPE bilayers behaved similarly to POPE, showing increased mobile fractions, less visible defects, and brighter fluorescence (Figure 2-6, red points). In fact, the mobile fraction for 90 mol% DLPE bilayers was 95% at 37 °C. As such, fluid SLBs with high mobile fraction for either POPE or DLPE can be made when working near physiological temperatures. The diffusion coefficients of both POPE and DLPE bilayers showed a temperature dependence, which was independent of the fluorophore used (Figure 2-10).

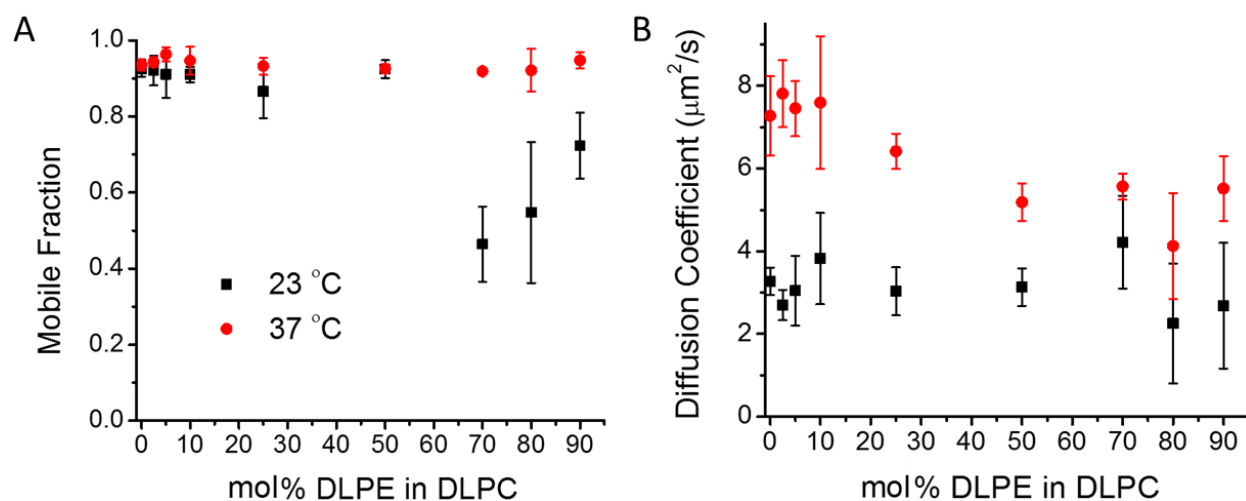


Figure 2-6. Properties of supported lipid bilayers with mixed DLPE and DLPC lipids at room temperature and physiological temperature as a function of DLPE concentration. A) Mobile fraction. B) Diffusion coefficient.

### ***Ni<sup>2+</sup> Binding Assay***

PE-containing bilayers can be used to investigate a variety of physical properties with PE lipids. Unlike PC, PE's primary amine can be deprotonated, and therefore can form metal-ligand binding complexes. Previously, it has been shown that Cu<sup>2+</sup> forms complexes with lipid head groups by directly binding to amines on phosphatidylserine<sup>14,15</sup> as well as with PE.<sup>28</sup> Specifically, the primary amine from PE can directly bind to transition metals to form a metal coordination complex in its deprotonated form. As such, we hypothesized that other transition metals from the Irving-Williams series should also be able to bind.<sup>58,59</sup> To test this hypothesis, we have performed experiments with NiCl<sub>2</sub> using SLBs in a microfluidic device, where increasing concentrations of Ni<sup>2+</sup> were introduced above an SLB. When Ni<sup>2+</sup> bound to PE, it quenched nearby fluorophores through an energy transfer mechanism.<sup>27,60</sup> This provided a direct measure of Ni<sup>2+</sup> binding to the SLB. Figure 2-7a shows a Ni<sup>2+</sup> binding curve for a bilayer containing 50 mol% POPE at room temperature, with a fitted  $K_D$  value of 0.38 mM. This is in stark contrast to Ni<sup>2+</sup> binding to a PC headgroup, which has been reported to have a  $K_D$  value of 1.2 M,<sup>61</sup> a value that was more than a factor of 3000 weaker. Since deprotonation of the amine was a crucial step in binding (Fig 2-7b), the binding curve was measured at pH 8.5, which increased the available binding sites, but should not affect the intrinsic  $K_D$  value.<sup>28</sup> This experiment represents a clear, but simple demonstration of the differences in behavior for membranes containing significant concentrations of PE compared to ones that contain just PC.

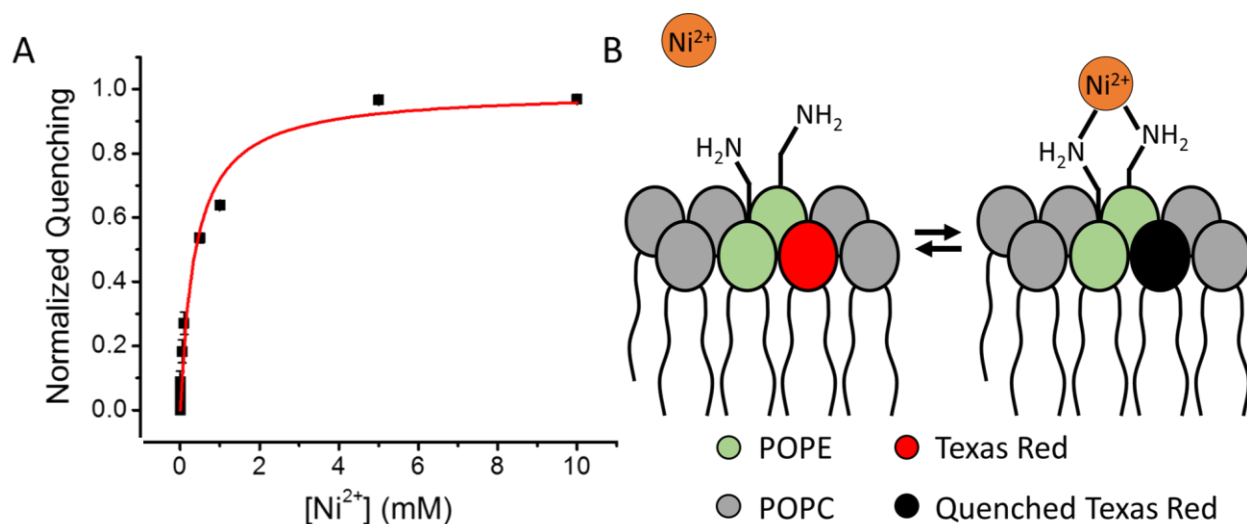


Figure 2-7. A)  $Ni^{2+}$  binding titration curve measured at room temperature in 10 mM Tris buffer at pH 8.5 to 50 mol% POPE bilayer. B) Representation of  $Ni^{2+}$  binding to two deprotonated PE head groups. Bivalent binding is expected at this density of PE. Error! Bookmark not defined.

## Discussion

PE can be employed in supported lipid bilayer studies despite its negative curvature. PE lipids have often been classified as nonbilayer lipids due to their conical shape,<sup>4</sup> though they can be incorporated into unilamellar gel phases or liquid-ordered phases.<sup>62,63</sup> Indeed, many studies use PE only to introduce membrane curvature, ignoring possible effects of hydrogen-bonding. By incorporating PE into a flat SLB, it is possible to focus on headgroup interactions instead and minimize curvature effects.

PE is both a hydrogen-bond donor and acceptor, while PC is only a hydrogen-bond acceptor. This capability opens up a host of potential interactions, both with other membrane components and with molecules or proteins in the bulk solution. It is known that PE can hydrogen-bond with the phosphate and carbonyl groups of neighboring PE lipids,<sup>21,64</sup> and has been predicted to hydrogen-bond with other lipids such as phosphatidylglycerol (PG).<sup>65</sup> PE can also form

hydrogen-bonds with water, causing differences in hydration as well as allowing water molecules to bridge neighboring lipids.<sup>66</sup> Such intra-bilayer hydrogen bonds could direct the organization of lipid domains.<sup>21</sup> As demonstrated above, PE can be used to form domains of either gel or liquid ordered phases in two component systems, where presumably the PE-rich domains contain many intermolecular hydrogen bonds. Similarly, these hydrogen-bonding networks likely extend to PE-PG interactions, impacting the organization of PG.<sup>67</sup> With the capability to study PE enriched SLBs, it should be possible to gain a better understanding of the role of PE in two or more component systems that exhibit phase separation.

There are many basic physiological properties of biological membranes that exploit PE rather than PC lipids. We expect that these model systems will be extremely useful for measuring the affinity of small molecules which bind to membranes containing PE lipids. One example involves the use of PE-enriched SLBs to study the effects of antimicrobial peptides. Antimicrobial peptides are an important developing area of research as antibiotic resistant bacteria.<sup>68</sup> The effectiveness of antimicrobial peptides is dependent upon lipid composition,<sup>69,70</sup> and simple model system are needed to elucidate the individual contributions of different lipids. PE is the major component of many bacterial membranes, such as *E. coli*. As such, it is vital to study the interactions of PE with antimicrobial peptides to understand the binding and trans-bilayer penetration of peptides to formulate improved peptides for biomedical uses. PE-containing SLBs provide a direct route to systematic studies of these and other interactions.

## Supporting Figures

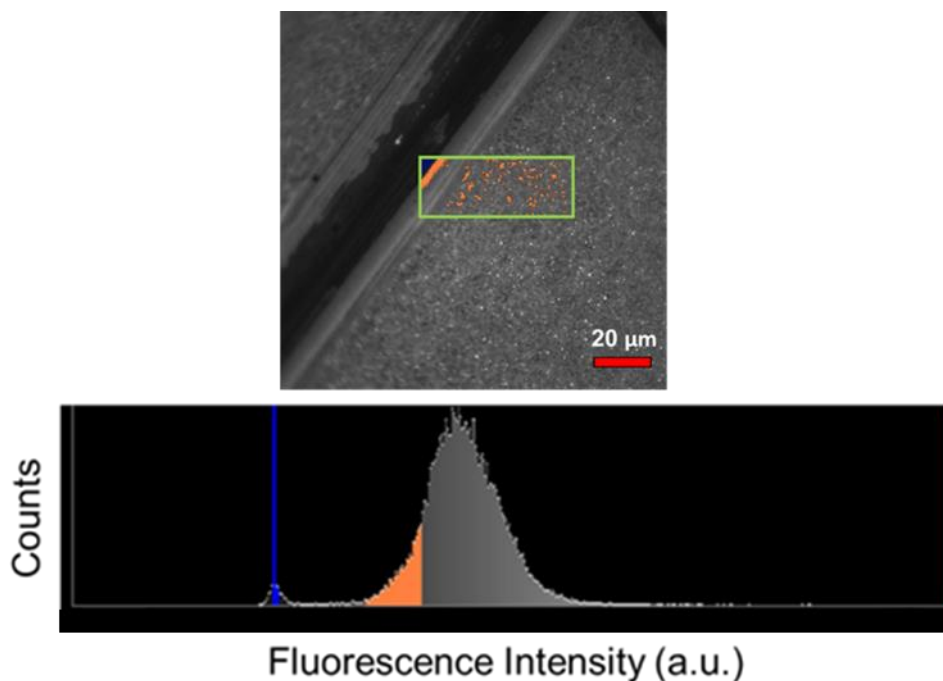


Figure 2-8. (Top) Fluorescence image of a 70 mol% POPE SLB imaged with a 100x objective. The green box indicates the area of the SLB analyzed in the bottom image. (Bottom) Histogram of fluorescence showing three distinct regions. The blue line in the histogram indicates the fluorescence level of the scratch region, where no bilayer material is present. The large peak in the histogram reflects the intensity of the nearby bilayer, where the liquid-ordered domains are colored orange (top and bottom) and the surrounding liquid-disordered phase is grey. From the relative difference in fluorescence between the blue and orange regions, it is clear that the orange spots in the top image are liquid-ordered domains, and not holes in the bilayer

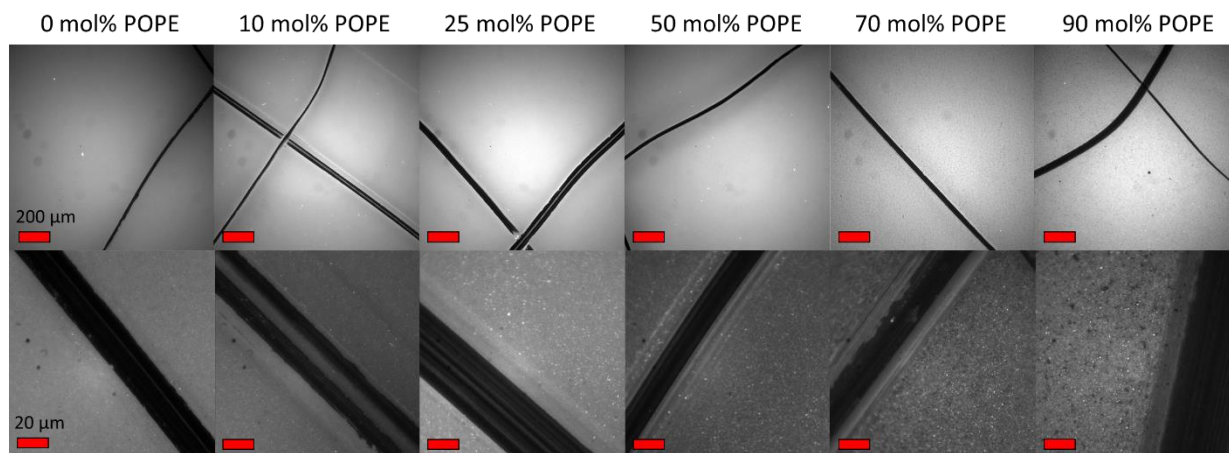


Figure 2-9. Images of POPE/POPC SLBs under two different magnifications (top, 10x; bottom, 100x). Dark lines are from scratches made with tweezers to remove lipid bilayer material and create contrast.

70 mol % of PE <sub>d31</sub>			
	Theoretical % of IR Signal	IR Signal for SLB & Bulk	IR Signal for SLB
23 °C	31 %	30% ± 2.5%	30% ± 3.4%
37 °C	31 %	31% ± 1.8%	31% ± 3.7%
80 mol % of PE <sub>d31</sub>			
	Theoretical % of IR Signal	IR Signal for SLB & Bulk	IR Signal for SLB
23 °C	35 %	26% ± 0.8%	30% ± 0.8%
90 mol % of PE <sub>d31</sub>			
	Theoretical % of IR Signal	IR Signal for SLB & Bulk	IR Signal for SLB
23 °C	39 %	38% ± 0.9 %	32% ± 2.2 %
37 °C	39 %	40% ± 3.7 %	41% ± 1.7 %

Table 2-1. Summary of ATR-FTIR results of three high mole percentage POPE bilayers. Bilayers were formed using chain perdeuterated POPE, where the saturated tail was deuterated and the unsaturated tail was hydrogenated. The theoretical percentage of IR signal was calculated considering the full structures of both POPC and POPE, as well as the relative amounts of each. The vesicles were introduced and incubated into the cell, and the signal was recorded to obtain a “bulk” reading. Then the excess vesicles were flushed out and the reading taken again, this time only measuring what was left on the surface. These experiments were conducted on separate bilayers at two different temperatures.

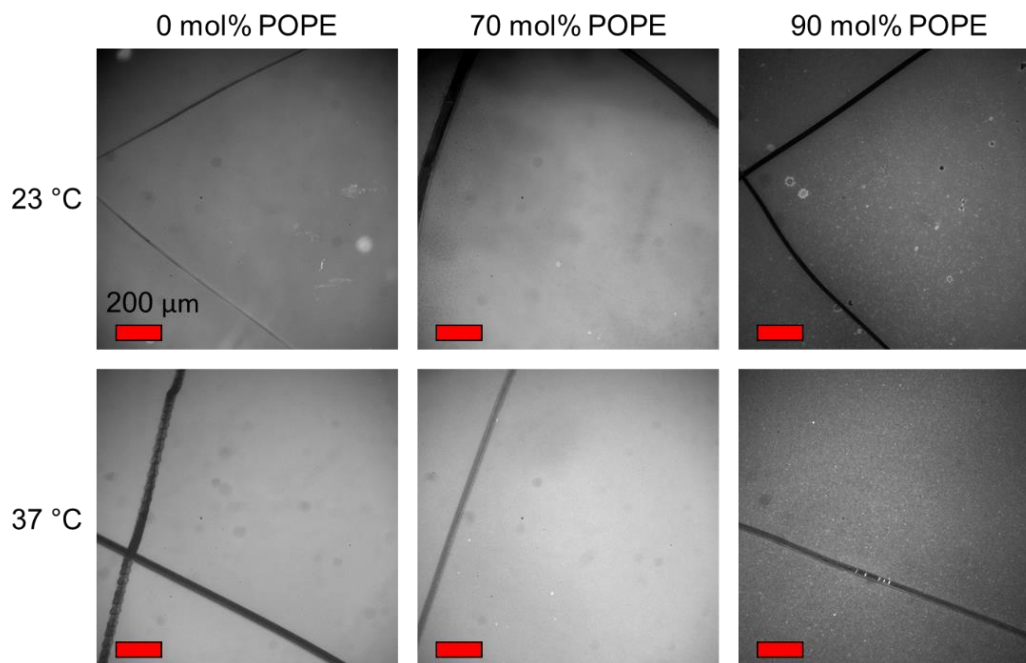


Figure 2-10. Fluorescent images of SLBs of various mol% of POPE that were formed at either 23 °C or 37 °C. The bilayers formed at 23 °C had more visible defects than those formed at 37 °C. Dark lines are scratches made by tweezers removing bilayer material to create contrast.

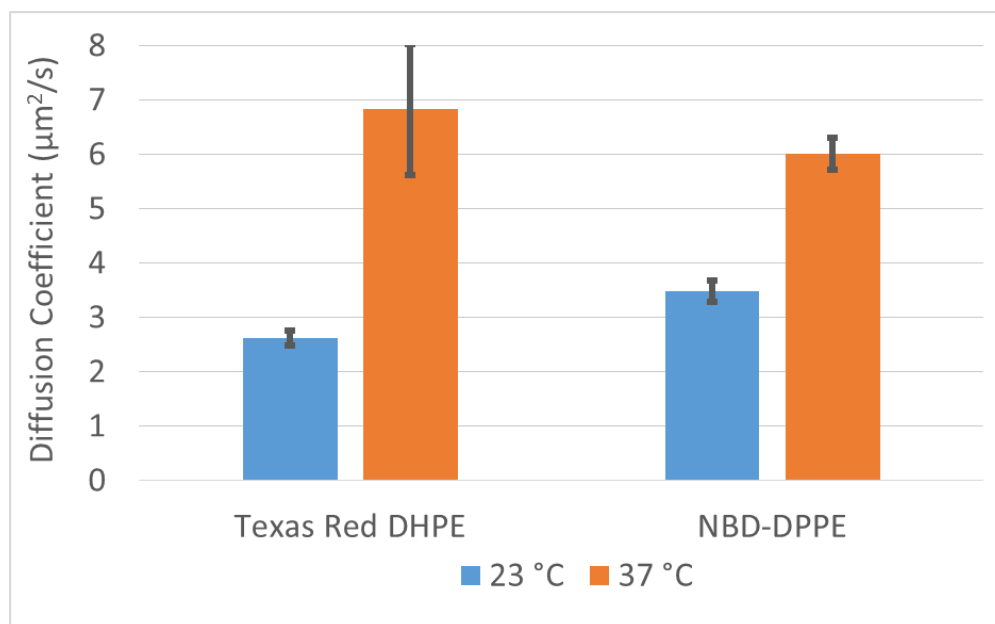


Figure 2-11. Comparison of two different fluorophores at room temperature and 37 °C in a POPC bilayer. Both probes used showed a significant increase in diffusion coefficient with the increase in temperature.

## Chapter 3 Copper Binds to PE and Increases Lipid Oxidation

### Introduction

Two common hallmarks of neurodegenerative diseases are lipid oxidation and increased concentrations of transition metal ions.<sup>71,72</sup> Transition metal ions, such as copper, are capable of undergoing redox cycling between its 1+ and 2+ oxidation states. When exposed to hydrogen peroxide, the redox cycling results in the production of reactive oxygen species (ROS), which can cause damage throughout the cells.<sup>73</sup> The ROS have very short lifetimes, typically traveling only a few molecular lengths before encountering a moiety that can be oxidized.<sup>74</sup> Therefore, the site of generation of the ROS is very important. We hypothesize that copper bound to the membrane surface leads to increased lipid oxidation (Figure 3-1).

Phosphatidylethanolamine (PE) is enriched in the brain, where it can make up as high as 45 mol% of lipid content.<sup>75</sup> The primary amine in the head group has a pKa of ~9.6, and only a fraction is deprotonated at neutral pH.<sup>76</sup> However, the deprotonated amine presents a binding site for the copper, as we demonstrate herein. The affinity of Cu<sup>2+</sup> to PE is measured as a function of PE at both neutral and basic pH. Additionally, a preliminary assay showing that even at neutral pH, increasing the amount of PE in the membrane leads to increased oxidation of a membrane-embedded oxidation probe.

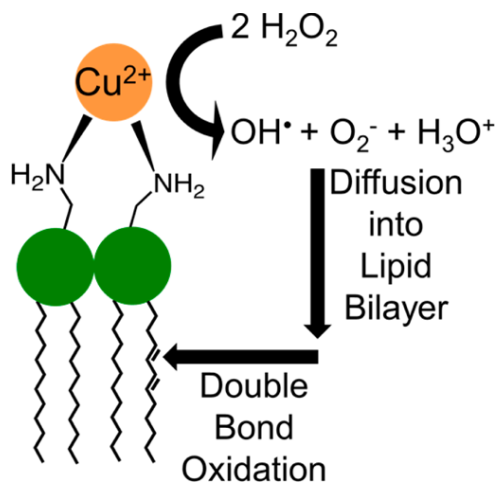


Figure 3-1. Schematic illustration of Cu<sup>2+</sup> binding to the amine moieties on PE head groups. Once bound, Cu<sup>2+</sup> participates in Fenton-like chemistry to produce ROS such as hydroxyl radicals and superoxide, which can oxidize double bonds within the membrane.

## Materials and Methods

### *Materials*

All phospholipids were purchased from Avanti Polar Lipids (Alabaster, AL). Texas Red 1,2-dihexadecanoyl-*sn*-glycero-3-phosphoethanolamine, triethylammonium salt (Texas Red DHPE) was purchased from Life Technologies (Grand Island, NY). Poly(dimethylsiloxane) (PDMS) was obtained from Dow Corning (Sylgard, silicone elastomer-184).

### *Lipid Vesicle Preparation*

Small unilamellar vesicles (SUVs) were made by the freeze-thaw extrusion method.<sup>7,13</sup> Briefly, the lipids were mixed at the desired ratio in chloroform, then placed under vacuum for 1.5 hrs. The lipid film was rehydrated to a density of 1 mg/mL in aqueous buffer containing 10 mM dibasic sodium phosphate (PBS) and 100 mM NaCl at pH 7.4 and sonicated for 20 min. They were then subjected to ten freeze-thaw cycles and extruded through a filter with 100 nm pores. All vesicles were used within 7 days of preparation.

### ***Microfluidic Device Fabrication***

SLBs were formed in PDMS devices on borosilicate glass (Fisher Scientific, Pittsburgh, PA). The glass was first cleaned in a detergent solution of 1:7 7X (BP Biomedicals) and 18.2 M $\Omega$  water, rinsed copiously with 18.2 M $\Omega$  water, dried with compressed nitrogen gas, and finally annealed at 530 °C for 5 hrs. This preparation rendered the glass surface hydrophilic. The microfluidic devices used for the titration were made from PDMS. Briefly, photolithography was used to pattern a photoresist on a glass slide, which was then etched using HF and cleaned to form a master. PDMS was mixed using 1 part crosslinker to 10 parts monomer, placed under vacuum for 1.5 hrs, then poured over the master before being placed in the oven at 55°C overnight. Inlets and outlets for each channel were punched through the PDMS block using a polished needle. The PDMS was attached to the cleaned glass following cleaning in an oxygen plasma cleaner (PDC-32G, Harrick, Pleasantville, NY) for 30 seconds. They were immediately pressed together and held in place for 1 minute, then heated for 1 minute at 100°C.

### ***Titration Measurements***

10  $\mu$ L of the desired vesicle solution was introduced into each microfluidic channel and incubated for 30 min. Buffer containing 10 mM PBS and 100 mM NaCl at pH 7.4 or pH 10 was used throughout the experiment. Buffer with increasing concentrations of CuCl<sub>2</sub> was introduced through plastic tubing, with each solution given at least one hour to equilibrate before measuring the fluorescence. Then the tubing at the inlet was removed, drained of solution, and the next solution was drawn through, and the tubing reinserted. The background fluorescence was subtracted from the average fluorescence of each channel, and was normalized to the initial fluorescence before the addition of CuCl<sub>2</sub>.

### ***Fluorescence Recovery after Photobleaching (FRAP)***

FRAP<sup>25,26</sup> experiments were carried out with a Nikon Eclipse TE-2000-U inverted microscope through a 10x objective. A 532 nm 300 mW solid state laser (Dragon Lasers) was used to bleach Texas Red-DHPE with a power averaging 5 mW for 1 s at the sample. The average diameter of the laser beam was 20  $\mu\text{m}$ , giving 0.016 mW/ $\mu\text{m}^2$  as the power per unit area. The average fluorescence intensity of the spot was analyzed over time as the bleached fluorophores diffused out and unbleached fluorophores took their place. Images were initially taken every 3 seconds, until the fluorescence in the bleached area no longer visually appeared to change, and then switched to every 30 or 60 seconds to minimize photobleaching. The fluorescence of the bleached spot was normalized to an unbleached reference spot, and the percentage recovery was plotted over time,

$$F(t) = \frac{F_t - F_0}{1 - F_0}$$

where  $F_t$  is the normalized fluorescence at time  $t$ , and  $F_0$  is the normalized fluorescence at  $t = 0$ .

The results were fit to a single exponential:

$$y = A(1 - e^{-bx})$$

where A corresponds to the mobile fraction (i.e. percentage of the bilayer able to recover) and b was used to calculate the diffusion coefficient D (how quickly the bilayer recovered):

$$\tau_{1/2} = \frac{\ln(2)}{b} \quad D = \frac{w^2}{4\tau_{1/2}} * \gamma$$

where  $w$  is the diameter of the laser beam and  $\gamma = 0.88$ .

### ***Bulk Fluorimetry Experiments***

The fluorescence spectra of vesicles in solution were collected using a QE 65000-FL scientific grade spectrometer with a DH-2000 deuterium tungsten halogen light source (Ocean Optics, Dunedin, FL). For vesicle oxidation experiments, vesicles composed of varying

concentrations of POPE, POPC, and 0.5 mol% of the fluorescent dye C11-BODIPY 581/591 (C11-BODIPY) were diluted in Tris buffer so that the total concentration of lipid in each experiment was held constant at 100  $\mu$ M, the concentration of C11-BODIPY in each experiment was 500 nM, and the concentration of POPE and POPC varied depending upon their relative mole percentages. The vesicles were exposed to various oxidizing and non-oxidizing conditions, and fluorescence spectra were recorded using an excitation wavelength of 560 nm and an integration time of 30 seconds. Measurements were taken every 30 seconds for fifteen minutes. No measurable photobleaching was observed over the course of the experiment. The fluorescence spectrum showed three peaks, a scattering peak at 560 nm, and two C11-BODIPY peaks at 594 nm and 630 nm. The 630 nm peak was very broad and had low intensity, so only the area of the 594 nm peak was used to calculate the oxidation rate. To calculate the area under the 594 nm peak, the spectrum was fit with three Gaussian peaks using Origin v7.

## Results

### *Dissociation Constant and Quenching Efficiency of $\text{Cu}^{2+}$ –PE*

The binding of  $\text{Cu}^{2+}$  to POPE was measured by microfluidic titration. Including 0.5 mol% TR-DHPE in the bilayer provides a way to directly measure the binding without labeling the binding site (PE) or the analyte ( $\text{Cu}^{2+}$ ), as the  $\text{Cu}^{2+}$  bound to the surface quenches nearby fluorophores by an energy transfer mechanism.<sup>27</sup> The fluorescence was measured with increasing concentration of  $\text{Cu}^{2+}$  for a series of PE bilayers at pH 7.4 (Figure 3-2). With 0 mol% POPE, the fluorescence was unaffected by the  $\text{Cu}^{2+}$ . As the amount of PE was increased, the quenching increased, although the measured  $K_{\text{DApp}}$  was not dependent on PE concentration, and were all in the range of 1-4  $\mu$ M. The depth of quenching is dependent on the number of binding sites and is

indicative of the  $\text{Cu}^{2+}$  loading. The  $\text{Cu}^{2+}$ -PE complex quenches by absorbing the fluorescence emitted by the TR-DHPE.<sup>36</sup> As the probe concentration is kept constant, the quenching efficiency is dependent on the distance between a  $\text{Cu}^{2+}$ -PE complex and the probe. When there is more PE present in the bilayer, there are more potential binding sites for  $\text{Cu}^{2+}$ , and the average distance between the bound complex and the TR-DHPE is decreased. Therefore the amount of quenching is increased without a change in the  $K_{D\text{App}}$ .

Overall, the quenching is relatively low, only quenching 10% even at 70 mol% PE. This is due to a combination of two factors: bilayer inhomogeneity and deprotonation of PE. First, the heterogeneity observed with increasing amounts of PE in SLBs, detailed in Chapter 2, causes lateral segregation of PE and TR-DHPE. It is known that TR-DHPE preferentially partitions into liquid-disordered phases,<sup>77</sup> while POPE is enriched in liquid-ordered phases. As the quenching efficiency depends on the distance between the  $\text{Cu}^{2+}$ -PE complex and TR-DHPE, this compartmentalizing reduces the quenched fraction. Therefore, as the PE concentration is increased and lipid domains begin to form, there is a less significant increase in quenching than expected.

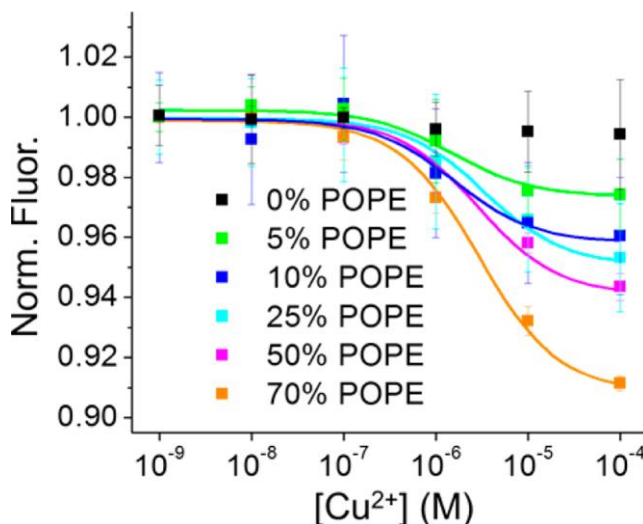


Figure 3-2. Normalized fluorescence intensity (Norm. Fluor.) from SLBs containing 0 to 70 mol % POPE with increasing concentrations of  $\text{Cu}^{2+}$ . The squares are data points and the solid curves represent least-squares fits to Langmuir isotherms. The error bars represent standard deviations from 6 independent measurements.

The second factor is the pH dependence. At pH 7.4, we are well below the intrinsic pKa of PE (9.6), so only a small fraction (~1 %) of the PE are deprotonated. Figure 3-3 shows the pH-dependent binding of  $\text{Cu}^{2+}$  to PE. In A, the binding of  $\text{Cu}^{2+}$  to 70 mol% PE SLBs was conducted at increasing pH. At pH 7.0, no appreciable binding was observed. As the pH was increased to pH 10.0, the binding profiles show an increase in the depth of quenching. The  $K_{\text{DApp}}$  is not significantly affected up to pH 9.0, but when the pH is raised above the pKa to pH 10, it is tightened by an order of magnitude. By increasing the pH, more PE is deprotonated, which renders it both negatively charged and increases the available binding sites. The negative charge attracts  $\text{Cu}^{2+}$  to the surface and changes the morphology of the membrane, decreasing the phase separation and therefore eliminating the sequestering of TR-DHPE from the PE.

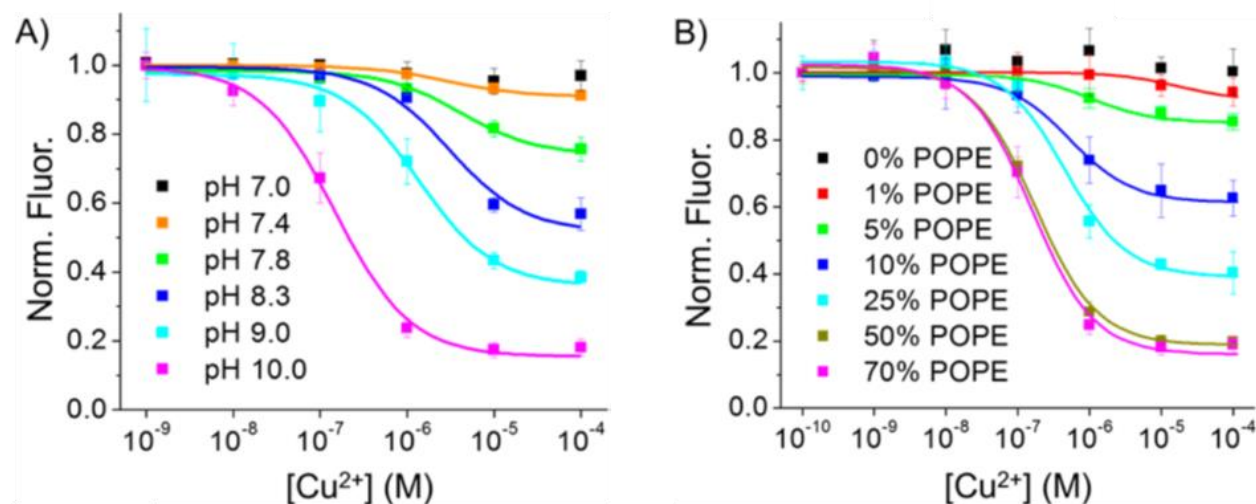


Figure 3-3. (A) Normalized fluorescence intensity from SLBs containing 70 mol% POPE, 29.5 mol% POPC, and 0.5 mol% TR-DHPE from pH 7.0 to 10.0. (B) Normalized fluorescence intensity from SLBs containing 0 to 70 mol% POPE at pH 10.0. The solid lines in each graph represent least-squares fits to a Langmuir isotherm. The error bars represent standard deviations from 6 independent measurements.

Figure 3-3B shows  $\text{Cu}^{2+}$  titrations of SLBs with various mol% of PE conducted at pH 10.0. As with 70 mol% PE, there is greater depth of quenching as more amines are deprotonated and able to serve as binding sites. It is also evident that there is a gradual tightening of the  $K_{\text{DApp}}$ . This can be explained by an increase of negative charge from the deprotonated PE. The negative charge recruits additional  $\text{Cu}^{2+}$  to the double layer, making the apparent binding constant tighter. Using Gouy-Chapman theory, it is possible to take the negative surface potential into account and calculate the intrinsic dissociation constant,  $K_{\text{DInt}}$ , for each.<sup>15,78</sup> These were again at low  $\mu\text{M}$ , and were comparable to the ones measured at pH 7.4.

Figure 3-4 shows the integrity of the PE SLBs at pH 10. Fluorescence recovery after photobleaching data showed high mobile fractions and diffusion coefficients typical of TR-DHPE in a fluid SLB that is largely unimpaired by increasing PE concentration. The small decrease in mobile fraction for bilayers containing 70 mol% POPE is likely due to the bilayer beginning to transition into the gel phase from the liquid crystalline phase.<sup>55</sup> Overall, the increased negative charge and smaller head group area resulting from the deprotonation of the amine did not impair the bilayer stability. In fact, comparison of fluorescence images at both pH values shows a decrease in inhomogeneities (Figure 3-5). As detailed in Chapter 2, higher concentrations of PE in the membrane leads to lateral phase segregation, in which the gel phase lipid POPE, is packed into liquid-ordered domains. However, when the PE lipids are deprotonated, the negative charges on the head groups repel one another, breaking up the lipid domains.

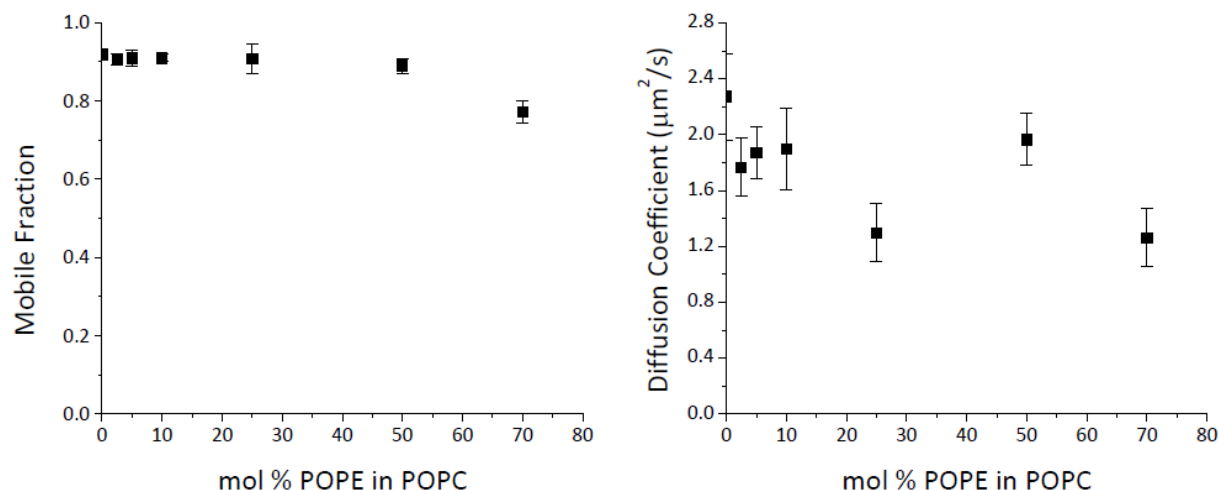


Figure 3-4. Fluorescence recovery after photobleaching data (FRAP) for 0-70 mol% POPE in POPC containing 0.5 mol% TR-DHPE at pH 10. The left graph shows the mobile fraction of each bilayer, whereas the graph on the right contains the measured diffusion coefficients.

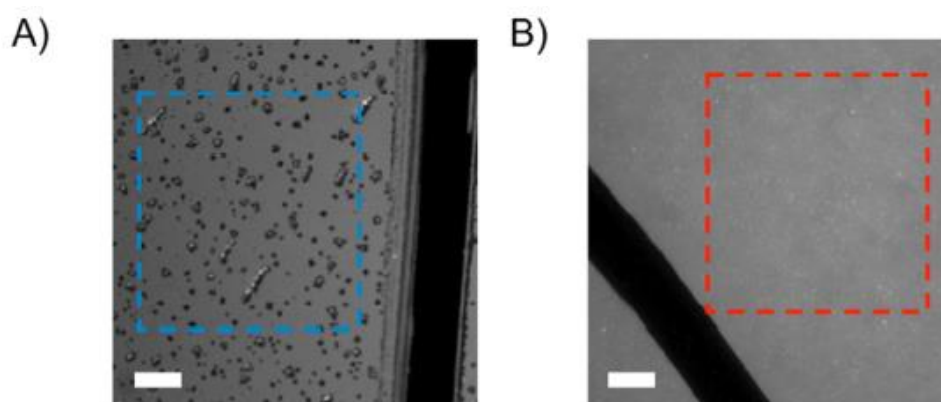


Figure 3-5. Fluorescent images taken under 20x magnification of 70 mol% POPE, 29.5 mol% POPC, 0.5 mol% TR-DHPE bilayers. A) pH 7.4 clearly shows lateral phase segregation. B) pH 10 is absent of phase segregation. The dark lines are scratches made by tweezers to remove bilayer material to provide contrast. Scale bars = 50  $\mu\text{m}$ .

### ***Membrane Species are Oxidized More Rapidly in the Presence of $\text{Cu}^{2+}$ -PE Complexes.***

The next step was to measure if the  $\text{Cu}^{2+}$ -PE complexes had an effect on oxidation of the membrane. This was done using an oxidation-sensitive fluorophore, C11-Bodipy,<sup>79</sup> which was incorporated into lipid vesicles. They were then exposed to  $\text{Cu}^{2+}$  and  $\text{H}_2\text{O}_2$  to induce oxidation,<sup>80,81</sup> which cleaves the fluorophore and changes the emission wavelength from 590 to 520 nm.<sup>79</sup> By

monitoring the decrease of fluorescence at 590 nm over time, which had better signal-to-noise than the peak growing in at 520 nm, it was possible to measure the kinetics of oxidation. The rate of oxidation depended on the amount of POPE included in the vesicles (Figure 3-6). Vesicles that contained 0 mol% POPE resulted in a small amount of oxidation of the fluorophore, while vesicles containing 70 mol% POPE had a much greater decrease in fluorescence over the same time period.

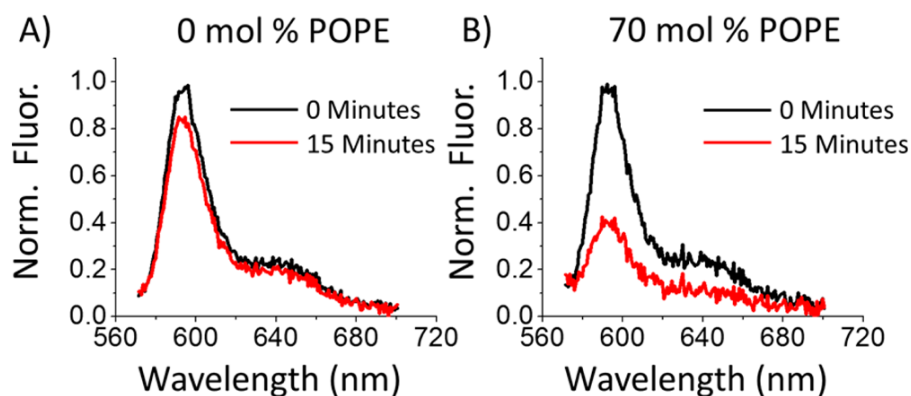


Figure 3-6. Fluorescence emission spectra of C11-BODIPY in lipid vesicle solutions composed of (A) 99.5 mol % POPC and 0.5% C11-BODIPY and (B) 70 mol % POPE, 29.5% POPC, and 0.5 mol % C11-BODIPY. The black lines represent fluorescence spectra taken immediately after the addition of 10 mM H<sub>2</sub>O<sub>2</sub> and 70  $\mu$ M Cu<sup>2+</sup>, while the red lines are from fluorescence spectra after 15 min have elapsed.

A more detailed study of the kinetics is shown in Figure 3-7. The red and blue squares represent controls, in which either H<sub>2</sub>O<sub>2</sub> or Cu<sup>2+</sup> was added, and the resulting slight decrease in fluorescence is likely due to photobleaching. The black, light blue, green, and gold squares represent vesicles exposed to oxidizing conditions with increasing amounts of POPE in the membrane. As can be seen, the rate of oxidation increase as more and more POPE is present. This supports the hypothesis that the Cu<sup>2+</sup>-PE complex causes an increase in oxidation. By using excess amounts of H<sub>2</sub>O<sub>2</sub>, it is possible to fit the data shown in Figure 3-7 using pseudo-first order kinetics. By plotting the natural log of the absorbance over time, it was possible to calculate apparent rate constants. The rate of oxidation of the probe was approximately 8 times higher for bilayers containing 70 mol% PE than for bilayers containing 0 mol% PE.

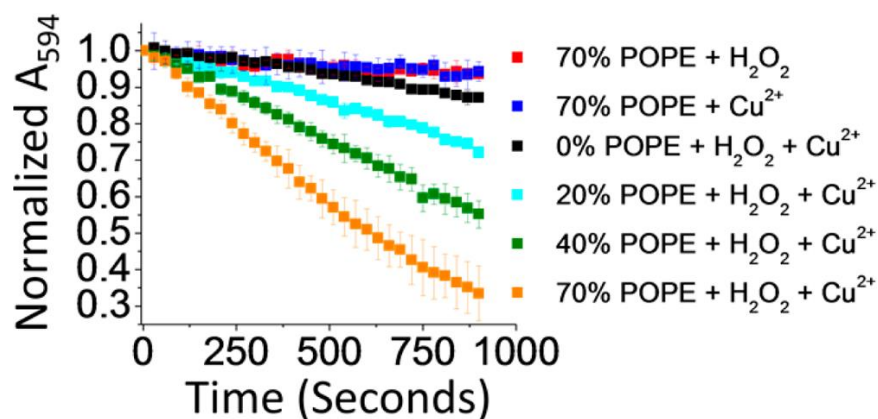


Figure 3-7. Change in the area of the 594 nm peak (Normalized A<sub>594</sub>) as a function of time for the conditions provided in the key. The Cu<sup>2+</sup> and H<sub>2</sub>O<sub>2</sub> concentrations were 70 μM and 10 mM, respectively, when these species were present.

## Discussion

This experiment represents an initial effort to link the increased metal content and lipid oxidation seen together in neurodegenerative diseases, but much remains to solidify this. First, the experiment does not measure the oxidation of a biological lipid. The fluorescence change best represents an increase in reactive oxygen species produced at the membrane surface.<sup>82</sup> The part of the fluorophore that is oxidized sits near the head groups of the lipids, and may not be an accurate indication of lipid oxidation in the body, which usually involves the oxidation within the lipid tail region. Additionally, biological media is much more complex than the simplified buffer conditions used here, and there would be many other potential targets for the reactive oxygen species to oxidize. Therefore, the Cu<sup>2+</sup>-PE complex becomes even more important, as radicals produced by Cu<sup>2+</sup> further away from the surface will be even less likely to cause damage to the membrane. The next step is to move to *in vitro* cell studies to see if this holds true.

In healthy cells, PE is predominately on the inner leaflet of the plasma membrane,<sup>83</sup> where the concentration of free Cu<sup>2+</sup> is essentially 0, making it unlikely to have a Cu<sup>2+</sup>-PE complex form. However, many disease states disrupt one or both of these. For instance, during apoptosis, PE flips

to the outer leaflet of cells,<sup>83</sup> where it can interact with much higher  $\text{Cu}^{2+}$  concentrations. We hypothesize that binding of  $\text{Cu}^{2+}$  to exposed PE could cause increased oxidation and actually cause necrosis, in which the normal apoptotic clearance is unable to happen and the cells end up lysing their contents and perpetuating the disease state.<sup>84</sup> Other possible scenarios arise when metal homeostasis is disrupted,<sup>71</sup> and there is more copper present in the cell than usual, leading to lipid oxidation without apoptosis. Further understanding of these processes can provide targets for neurological treatments.

## Chapter 4 Effect of Metal-Lipid Complexes on Lipid Domains Containing Phosphatidylserine

### Introduction

Lipid rafts in the plasma membrane are suspected to be critical organizers of integral membrane proteins and membrane receptors, but there is no consensus as to the size and duration (or even existence) of these structures *in vivo*.<sup>3,32</sup> This has led to a number of studies in simplified, model bilayer systems in order to better understand the biophysics that result in lipid phase behavior. Many simplified model systems, such as supported lipid bilayers and unilamellar vesicles, have been employed to study domain formation.<sup>30</sup> It is known that in model systems, a mixture of lipids containing saturated and unsaturated acyl chains will laterally phase segregate within a bilayer into liquid-ordered and liquid-disordered domains.<sup>31</sup> This creates a nonhomogeneous bilayer with regions of different composition and packing density of the component lipids. However, the influence of lipid head group interactions on raft formation has been less explored. Even less well understood is the role of transition metal cations in modulating the phase behavior due to head group interactions.

Cations are known to interact with phospholipid head groups. Such interactions have been shown to affect lipid domain formation. For example, millimolar concentrations of  $\text{Ca}^{2+}$  can induce domain formation in bilayers containing negatively charged lipids such as phosphatidylserine (PS) by electrostatic interactions.<sup>29,34</sup> Similarly, domains can be induced by dimerization of artificial lipids utilizing  $\text{Cu}^{2+}$  at micromolar concentrations or even lower.<sup>85</sup> It has been speculated that divalent cations act as electrostatic glue, holding the head groups together and increasing the local packing density to create a liquid ordered phase. Recently, we discovered a similar system with PS and  $\text{Cu}^{2+}$  that should have a more dramatic effect due to a far tighter binding of the lipids to the cation.<sup>14,15</sup>

Such a reorganization of the membrane could prove important during cell apoptosis. In healthy cells, PS is preferentially partitioned to the inner leaflet of the plasma membrane, where the concentration of free  $\text{Cu}^{2+}$  inside the cell is effectively zero.<sup>86</sup> During apoptosis, PS flips to the outer leaflet, where it is exposed to higher concentrations of labile  $\text{Cu}^{2+}$ .<sup>1</sup> The appearance of PS- $\text{Cu}^{2+}$  domains could therefore play a role in normal apoptotic cell clearance or participate in disease states.

Using model supported lipid bilayers, we have shown that PS binds directly to copper (II) to form a 2:1 lipid:metal complex, as opposed to solely electrostatic attraction.<sup>14,15</sup> The dissociation constant is dependent on PS density in the bilayer. The apparent dissociation constant is  $6.4 \times 10^{-12}$  M at 20 mol% PS in a PC bilayer. This is much tighter than the reported millimolar  $\text{Ca}^{2+}$ -PS binding.<sup>29,34</sup> The mode of binding for  $\text{Cu}^{2+}$  is very different than that of  $\text{Ca}^{2+}$ .  $\text{Ca}^{2+}$  binds electrostatically to the phosphate or carboxylate moieties on PS lipid head groups, encouraging membrane reorganization and domain formation, and recent data from our group suggests that  $\text{Zn}^{2+}$  binds similarly to  $\text{Ca}^{2+}$ .<sup>36</sup> In contrast,  $\text{Cu}^{2+}$  binds in a bidentate fashion to the deprotonated amine and carboxyl groups on two separate PS lipids, forming a four-coordinate metal center. This results in no change in the overall charge on the membrane, as two protons are released in the process.<sup>14</sup> It can therefore be hypothesized that this binding should change membrane structure in a markedly different manner than  $\text{Ca}^{2+}$  or  $\text{Zn}^{2+}$ , which interact electrostatically and neutralize the charge on the surface. (Figure 4-1)

Normally, domain formation is observed with a fluorophore that preferentially partitions into one of the domains, but this is not feasible here due to  $\text{Cu}^{2+}$  quenching.<sup>27</sup> The  $\text{Cu}^{2+}$ -PS lipid complex quenches nearby fluorescent lipids in vesicles and supported bilayers through an energy transfer mechanism, which allows for facile measurements of binding.<sup>14,15</sup> However, it makes

detecting domain formation using fluorescence microscopy very challenging, especially if the domains are smaller than the diffraction limit of light. This chapter explores the use of alternative techniques, small angle neutron scattering (SANS) and differential scanning calorimetry (DSC), for detection and characterization of lipid domains. SANS, done in collaboration with the Katsaras group at Oak Ridge National Laboratory, has been used to measure nm-sized domains in bulk lipid vesicles.<sup>32,87,88</sup> DSC, taken at the Automated Biological Calorimetry facility here at Penn State, was used to measure the melting temperature and enthalpy required for the lipid domains to form a homogeneous bilayer.<sup>89</sup> The experiments described herein involve domain systems including the negatively charged head group PS, which are then exposed to transition metal ions such as  $\text{Cu}^{2+}$  and  $\text{Zn}^{2+}$ . Overall, these lipid-cation interactions display a limited effect, especially at sub-mM concentrations. At mM concentrations, there is evidence of a  $\text{PS-Zn}^{2+}$  effect similar to a  $\text{PS-Ca}^{2+}$  effect, although further experiments are needed to conclusively determine what is happening.

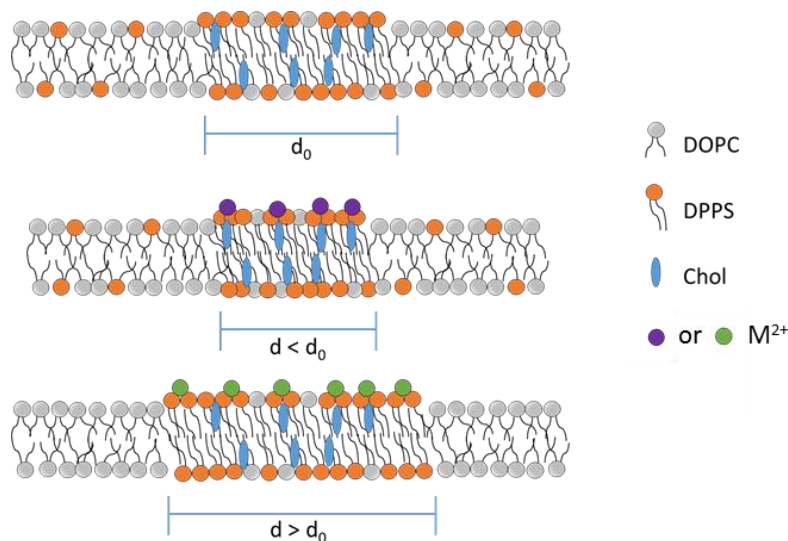


Figure 4-1. Schematic of lipid domains within a membrane. Top shows phase segregation with cholesterol and lipids with saturated tails closely packed in the liquid ordered domains, and lipids with unsaturated tails in the liquid disordered domains. Middle shows a possible result of binding a divalent cation to the negatively charged PS head groups, which could shrink the size of the ordered domains. Bottom shows an alternative result that changes the partitioning coefficient of the PS lipids to the different domains, causing the ordered domains to enlarge.

## Materials and Methods

### ***Materials***

1,2-dipalmitoyl-*sn*-glycero-3-phospho-L-serine (DPPS), 1,2-dioleoyl-*sn*-glycero-3-phospho-L-serine (DOPS), 1,2-dilauroyl-*sn*-glycero-3-phospho-L-serine (DLPS), 1,2-dipalmitoyl-*sn*-glycero-3-phosphocholine, (DPPC), 1,2-dioleoyl-*sn*-glycero-3-phosphocholine (DOPC), 1-palmitoyl-2-oleoyl-*sn*-glycero-3-phosphocholine (POPC), and cholesterol all were purchased from Avanti Polar Lipids (Alabaster, AL). Table 4-1 has the individual melting temperatures for the gel-to-liquid phase transition for each phospholipid.

### ***Lipid Vesicle Preparation***

Small unilamellar vesicles (SUVs) were made by the freeze-thaw extrusion method.<sup>7,13</sup> Briefly, the lipids were mixed at the desired ratio in chloroform, then placed under vacuum for 1.5 hrs. The lipid film was rehydrated to a density of 10 mg/mL in aqueous buffer containing 10 mM Tris (SANS) or MOPS (DSC) buffer at pH 7.4 and sonicated for 20 min. They were then subjected to ten freeze-thaw cycles and extruded through a filter with 60 nm (SANS) or 200 nm (DSC) pores. Vesicles were extruded at ~50 °C. All vesicles were used within 7 days of preparation.

### ***SANS Experiments***

Experiments were designed so that if the lipids were homogeneously distributed within the vesicles, then they would have the same scattering length density (SLD) of the solvent, making them effectively invisible (Figure 4-2).<sup>88</sup> To do this, the hydrogen to deuterium ratio (H/D) of the solvent, head groups, and lipid tails had to be calculated and optimized before the experiments

were begun. This was done by using a mixture of H<sub>2</sub>O and D<sub>2</sub>O, chain perdeuterated DPPS, and the expected exchange of hydrogen for deuterium on the primary amine in the head group of PS. That calculations directed us to use 46% D<sub>2</sub>O and to have all of the DPPS perdeuterated, rather than a mixture of h-DPPS and d-DPPS.

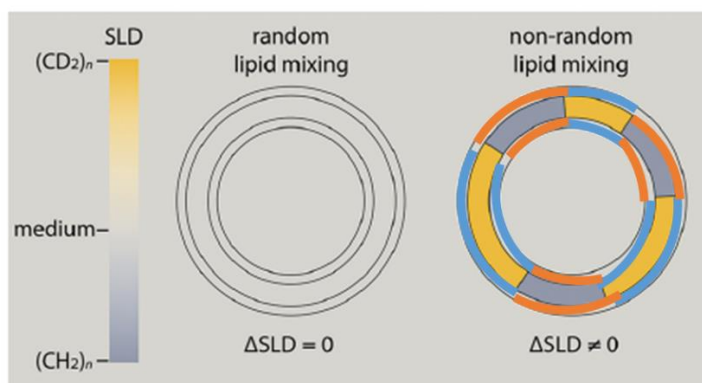


Figure 4-2. Schematic showing the tuning of H/D ratio to customize what is measured using SANS. Differences in the scattering length density (SLD) give rise to signal, so in an ideal lipid mixing without domains, the three areas: head group, tails, and solvent, can be tuned to match each other. This is akin to heating the samples to melt the domains, and no signal should be seen at higher temperatures. When there is phase separation, the different regions each have their own SLD, giving rise to signal. Adapted from Reference 88.

On the EQ-SANS beamline at the Spallation Neutron Source at Oak Ridge National Laboratory, the prepared vesicle solutions were loaded into 1-mm banjo cells and placed in the sample holder. The neutrons, generated from a liquid mercury target, were focused as a beam with a wavelength of 4 Å through to sample and onto the detector, which was at a 1.3 m distance from the sample. The neutrons are scattered very small angles (often <1°) and hit the detector at some distance from the center (where a neutron that was not deflected would hit). The scattering data are integrated and presented as a vector  $\vec{q}$ . The absolute value,  $q$ , is related to a physical distance in the sample  $d$  by the equation  $q = \frac{2\pi}{d}$ . (Figure 4-9)  $d$  can represent any characteristic distance

related to the sample, such as the thickness of the bilayer, the size of the vesicle, the diameter of a domain, the distance between domains, etc. Therefore, any feature with a SLD that does not match the SLD of the solvent, taken as the background, will give rise to SANS intensity.<sup>88</sup>

## Differential Scanning Calorimetry

Vesicle samples were loaded into a 96-well plate and brought to the Automated Biological Calorimetry facility and placed in the MicroCal VP-Capillary DSC (Malvern Instruments Inc., United Kingdom). The samples were run from 4 °C to 65 °C at a scan rate of 30 °C/hour. In Origin, buffer scans were background subtracted from the samples, which were then all normalized to the same concentration. The data were then baseline subtracted and fit to one or two peaks as needed.

Gel-to-Liquid Phase Transition Temperatures of Individual Lipids		
		T <sub>m</sub> (°C)
PC Lipids	DPPC	41
	DOPC	-17
	POPC	-2
PS Lipids	DPPS	54
	DOPS	-11
	DLPS	18

Table 4-1. Gel-to-liquid phase transition temperatures of the individual lipid components used in this study.

## Results

### ***Cu<sup>2+</sup>-PS: SANS and DSC***

As the Cu<sup>2+</sup>-PS complex has very tight binding constants (nM or lower depending on PS concentration),<sup>15</sup> we hypothesized that this could lead to the biggest changes in lipid domains. We twice attempted to use SANS to detail these changes. The first try, using 100 nm diameter vesicles

made of 36 mol% d-DPPS, 32 mol% DOPC, and 32% cholesterol, was based off the “classic” domain model system studies that used 1:1:1 molar ratios of DPPC:DOPC:cholesterol.<sup>31</sup> Disappointingly, there were no evident features amid the overall scattering in the SANS spectra at 20 °C, and there was still a substantial amount of scattering at 60 °C, at which temperature the domains should be melted and the vesicles’ SLD should match the solvent’s SLD (Figure 4-9). Significant scattering at  $q$  values of  $0.01 \text{ \AA}^{-1}$  and below correspond to the vesicle diameter size (60 nm and above) meant that either our SLD matching was off (whether in the calculations or experimentally making the vesicles), or that the domains are so large that they give contrast to the whole vesicle.

Taking lessons learned from the first attempt, we changed our vesicles to break up large, dominating domains, by moving to smaller, 60 nm vesicles and changing the lipid composition. The lipid ratio was changed to incorporate POPC instead of DOPC, which only has one site of unsaturation in the tails and decreases the driving force for lipid partitioning. However, a recent paper that explored the effect of POPC and DOPC on domains using SANS showed that when all of the DOPC is replaced with POPC, then there is not enough signal arising from the domains.<sup>88</sup> Therefore, we used a four component system shown in the table in the right of Figure 4-3. As expected, there was less overall scattering across the interested range of  $q$  values, and the scattering at 60 °C was greatly reduced (Figure 4-10). The contribution of scattering from the lateral segregation of domains was calculated by subtracting the scattering at 60 °C from the scattering at 20 °C (Figure 4-11) and the results shown in the spectra in Figure 3. While there is no conclusive evidence of a copper-dependent feature, there appears to be a feature evident at lower copper concentrations around  $q = 0.05 \text{ \AA}^{-1}$ , which has smoothed out at the highest copper concentration (1

$\text{Cu}^{2+}$ : 2 PS). This could indicate that  $\text{Cu}^{2+}$  has increased the size of the domains, but needs further studies for confirmation.

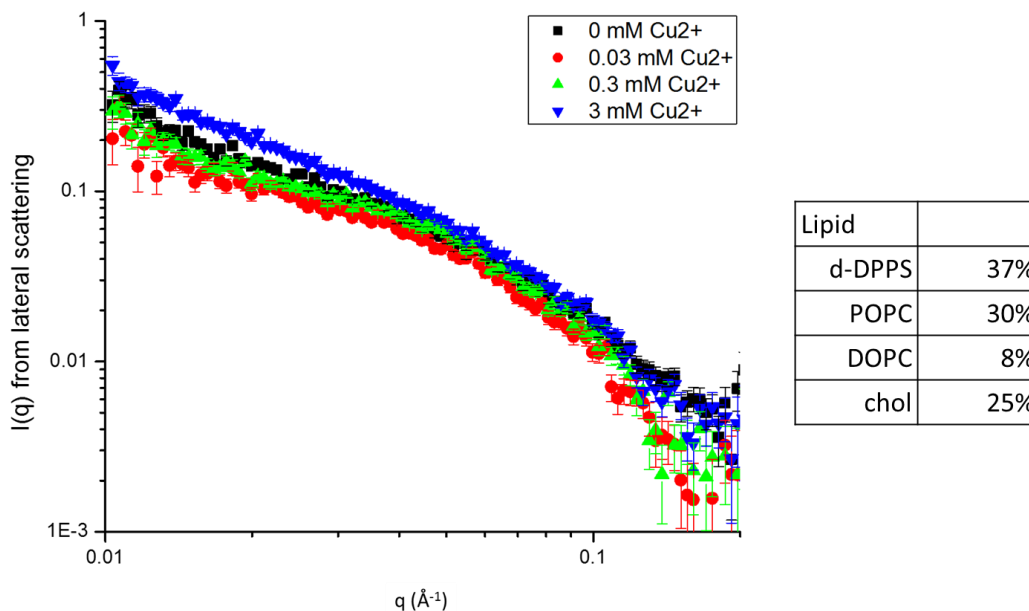


Figure 4-3. SANS intensity that comes from lateral scattering, i.e. domains, after subtraction of other contributions (see Figure S3), as a function of copper concentration. The physical length scales reflected by this spectra go from 6 nm ( $q = 0.1 \text{ \AA}^{-1}$ ) to 60 nm ( $q = 0.01 \text{ \AA}^{-1}$ ). The lipid composition in all samples is shown on the right.

DSC of the same samples used for the SANS experiments are shown in Figure 4-4. Using the same lipid and copper concentrations, we wanted to see if there was a change in the melting temperature,  $T_m$ . Although increasing copper concentration caused a slight shift of  $T_m$  (Table 4-2), it is not significant given the low signal to noise ratio. Together with the SANS data, this suggests the effect of the  $\text{Cu}^{2+}$ -PS complex on lipid domains is negligible.

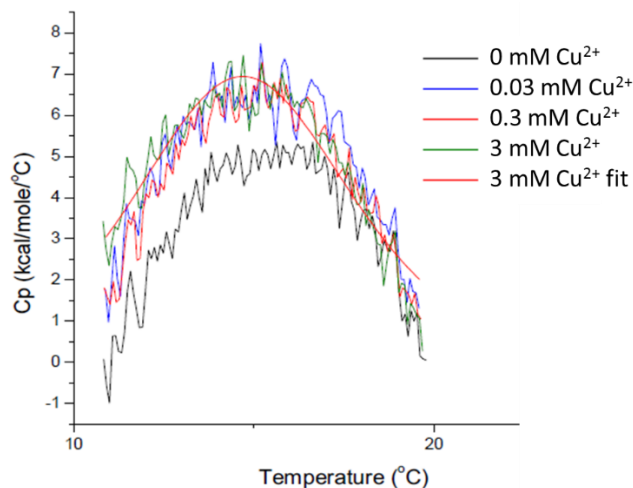


Figure 4-4. DSC results of the same sample composition used in the SANS experiments as a function of copper concentration. The corresponding melting temperatures are shown in Table 4-1 below.

[Cu <sup>2+</sup> ] (mM)	T <sub>m</sub> (°C)
0	15.5
0.03	15.2
0.3	15.1
3	14.8

Table 4-2. Melting temperatures obtained from DSC fits to the data shown in Figure 4.4. The slight decrease in T<sub>m</sub> is not necessarily significant, given the low signal to noise.

### ***Cu<sup>2+</sup> and Zn<sup>2+</sup> have Different Effects on PS Monolayers***

Although the binding of copper to PS did not cause a significant change in the lipid domains, other transition metal ions may have an effect. While copper tends to have tighter binding constant according to the Irving-Williams series,<sup>58,59</sup> other metals, such as zinc, bind differently to PS.<sup>36</sup> Figure 4-5 shows a surface pressure-area isotherm of the condensation of a PS monolayer in the presence of different divalent cations. The black curve represents the compression of PS without ions present, which shows a continuous increase in pressure as the area decreases, meaning there is no phase transition to a liquid condensed phase. However, divalent cations induce a phase

transition dependent on the identity of the cation. At 30 mN/m, considered the pressure experienced within a bilayer, there is not a significant difference in the area per molecule with the addition of copper. We also know that the binding of copper does not change the net charge on the bilayer, as it deprotonates the amines on 2 PS molecules by metal-assisted deprotonation as it binds.<sup>14</sup> Therefore, if there is no net change in charge or head group area, it is perhaps unsurprising that there was no measurable effect. Alternatively,  $\text{Zn}^{2+}$  changes both the charge and the area per headgroup. As can be seen in Figure 4-5, the zinc curve in red shows a reduced area per molecule at 30 mN/m, and recent DFT calculations have shown that  $\text{Zn}^{2+}$  binds electrostatically to the carboxylate and phosphate moieties on PS head groups.<sup>36</sup> It is likely that zinc could show very different effects on the domains than copper.

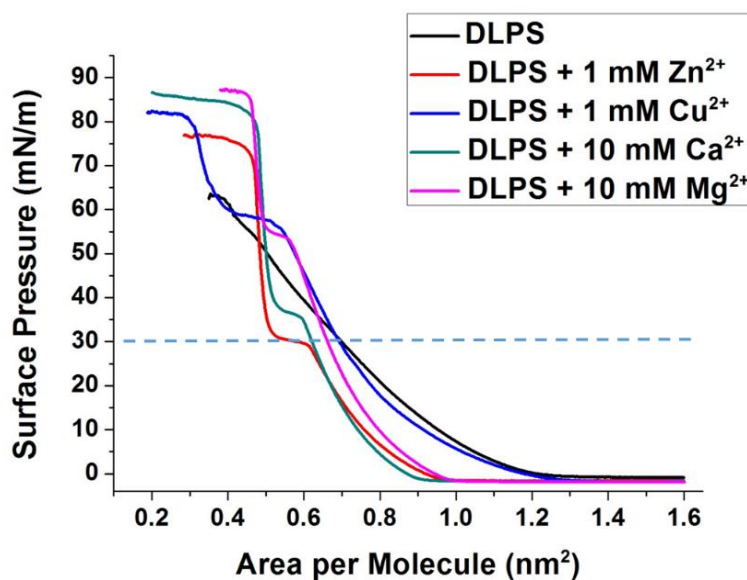


Figure 4-5.  $\pi$ -A diagram of a Langmuir monolayer compression study of DLPS (12:0, 12:0) at an air-water interface in the presence of different divalent cations. The dashed blue line shows the approximate pressure of a lipid bilayer. All were done with 10 mM Tris and 100 mM NaCl at pH 7.4.

## ***Zn<sup>2+</sup>-PS: DSC***

To see the effects of zinc on PS domains, we moved to a simpler three component system using 1:1:1 molar ratios of DPPS:DOPC:chol as the lipid composition. Figure 4-6 shows the results of the zinc series, where the highest concentration of zinc is 2.6 mM, making the Zn<sup>2+</sup>:PS ratio 1:2. At concentrations less than millimolar, the only evident change is an increase in the enthalpy required to melt the domains, and the T<sub>m</sub> of 21 °C is unaffected. However, at the highest concentration, a second peak appears at higher temperatures, with the fitted T<sub>m</sub> given as 51 °C.

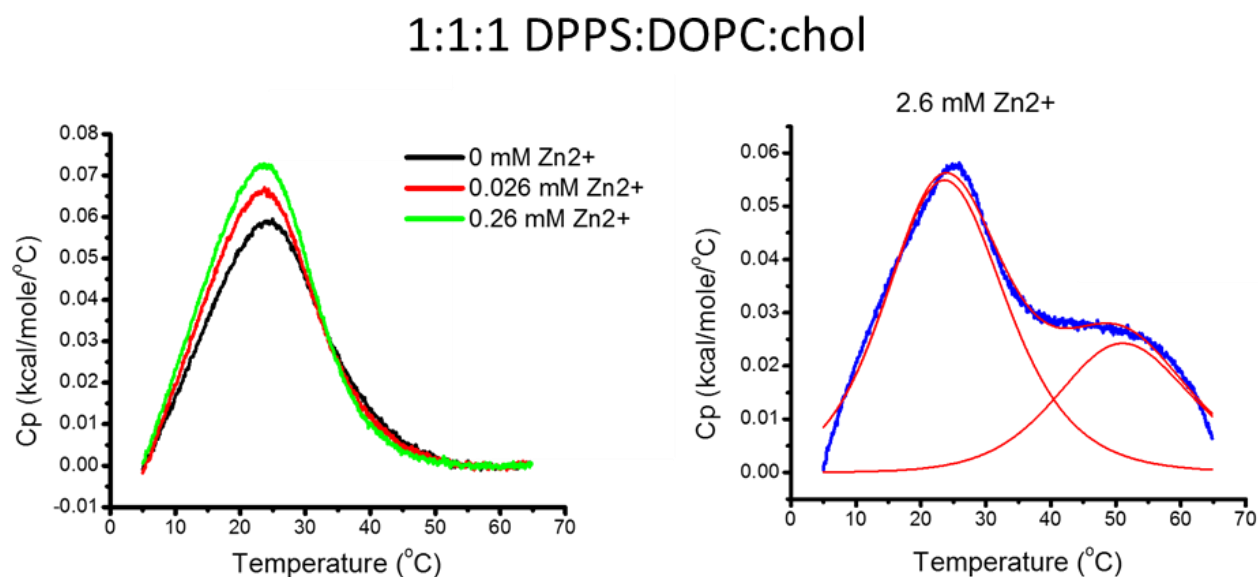


Figure 4-6. DSC peaks showing the melting of DPPS:DOPC:chol in the presence of Zn<sup>2+</sup>. A) At lower concentrations of zinc, more heat is required to melt the domains and no significant change in melting temperature is observed. B) At 2:1 PS:Zn<sup>2+</sup> concentrations, there is a second peak at higher temperature that emerges. The red lines represent the overall fit and the two individual peak fits.

To understand if the second peak that arose was due to a specific Zn<sup>2+</sup>-PS interaction, and not a nonspecific interaction with phosphate groups of any lipid, a control was done with all PC head groups. As shown in Figure 4-7, the same concentrations of zinc did not result in a second peak when DPPC:DOPC:chol vesicles were used. The second peak seen with PS-containing

vesicles could be the result of  $\text{Zn}^{2+}$  gluing only the PS head group together. It is not known at this time whether this happens even before the lipids assemble into vesicles, which could result in two different vesicle populations when the lipid films are rehydrated. If one of the vesicle populations is enriched in DPPS it could account for the double peak, as DPPS has a  $T_m$  of 54 °C. Alternatively, if we assume an even distribution of lipids, then the two peaks could represent more complicated domain structures, such as vesicles with 3 coexisting phases or domains that melt in two stages. Further experiments, such as cycling from cold to hot to observe any hysteresis or fluorescence of giant unilamellar vesicles (GUVs) could help narrow down the possibilities.

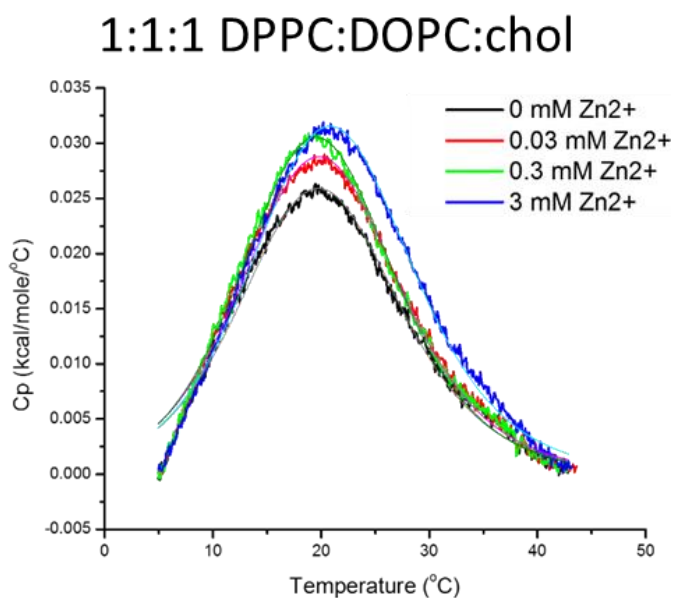


Figure 4-7. DSC results for the PC control for the same concentrations of zinc. Similarly, there is an increase in heat needed to melt the domains, but there is no second peak evident at the highest concentrations of zinc.

Finally, DSC experiments were conducted that switched the location of PS within the domains using 1:1:1 molar ratio DPPC:DOPS:chol vesicles with the same zinc concentrations. The hypothesis was that if zinc is able to shrink the head group area as seen in the  $\pi$ -A diagram in Figure 4-5, then there would be a more noticeable effect on the domains if the PS is located in the

liquid-disordered domains, rather than the liquid-ordered phase where they are already condensed. Therefore it was surprising to see practically the same results as the DPPS:DOPC:chol vesicles (Figure 4-8). As with all other vesicle compositions, the amount of enthalpy required increased with zinc concentration (summary of  $\Delta H$  given in Figure 4-12). And again, the PS containing vesicles had a second peak appear, regardless of whether the PS tails were saturated or unsaturated. There is clear evidence of a  $\text{Zn}^{2+}$ -PS interaction, though further studies are needed to provide a definitive picture.

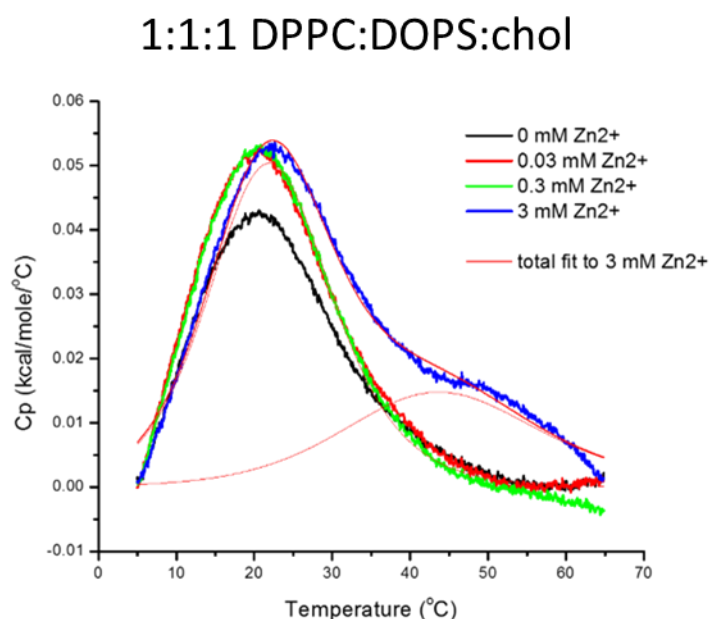


Figure 4-8. DSC results showing the melting of domains with DPPC:DOPS:chol, where PS is now localized in the liquid disordered domains. There is not much difference from when it was in the liquid ordered domains.

## Discussion

The data presented herein is largely preliminary, and can at best only hint at answers. The copper data taken with SANS resulted in too much scattering to make out any conclusive features. Previous domain studies using SANS have only been done with PC head groups,<sup>32,87,88</sup> and the presence or absence of domains does not change the scattering due to the head group region, and

therefore only segregation of the tails matters. In our system, lateral segregation results in two regions within the tails and two more regions within the head groups, as some are enriched in PS and some are enriched in PC. This additional segregation results in more scattering and makes visible other characteristic lengths within the sample, effectively hiding the answers we sought. The DSC showed there was no change in the  $T_m$  or the enthalpy required, but it is possible that the size of the domains were changed without those factors affected.

Similarly, the zinc series resulted in a slight increase of enthalpy regardless of the lipids used, though it was arguably more for the PS-containing vesicles (Figure 4-12), and no shift of the  $T_m$  (Table 4-3). This could be due to the beginnings of electrostatic binding to the phosphate moieties in PS, increasing the energy required to melt the domains. A calcium control is required to confirm this. The only interesting feature was the second peak at millimolar concentrations of zinc that was due to a  $Zn^{2+}$ -PS interaction. While the cause is likely the gluing effect, it would be worthwhile to explore what the physical result is, whether it is affecting the composition of the vesicles themselves or affecting the PS within the vesicles. The second peak that appears is always at higher temperatures, close to the individual melting temperature from the gel to liquid phase for the saturated tail lipid. In the case of DPPS ( $T_m = 54\text{ }^{\circ}\text{C}$ ) in the DPPS:DOPC:chol vesicles, a possible scenario involves gluing the PS head groups together to form gel phase domains, in addition to the liquid-ordered domains seen present at lower  $Zn^{2+}$  concentrations. The liquid-ordered domains would melt as usual, giving rise to the first peak, but the gel phase domains would only melt at higher temperatures, hence the second peak seen at  $51\text{ }^{\circ}\text{C}$ .

However, the double peaks seen with DPPC:DOPS:chol require a different explanation, as the  $T_m$  for DOPS is  $-11\text{ }^{\circ}\text{C}$ . The second peak seen with this composition is slightly lower at  $45\text{ }^{\circ}\text{C}$ , closer to the  $T_m$  of DPPC ( $41\text{ }^{\circ}\text{C}$ ). We know the binding constant of  $Zn^{2+}$  to PC to be above  $1\text{ M}$ ,

and Figure 4-7 confirms there is no direct  $\text{Zn}^{2+}$ -PC interaction. One hypothesis is the binding of one  $\text{Zn}^{2+}$  to two DOPS lipids changes the partitioning of the DOPS lipids. The bound complex would have a total of 4 unsaturated double bonds, one for each lipid tail, decreasing the already small population of DOPS in the liquid-ordered domains and making them more gel-like.  $\text{Zn}^{2+}$  would also neutralize the negative charges on the PS in the liquid-disordered domains and stabilize them. The combination of these effects could give rise to the second peak. It is also a possibility that three-dimensional structures such as protrusions, tubules, multilamellar nested vesicles, etc. are formed. Fluorescence studies of GUVs could be very enlightening.

T <sub>m</sub> of Domains by DSC						
		0 mM Zn <sup>2+</sup>	0.03 mM Zn <sup>2+</sup>	0.3 mM Zn <sup>2+</sup>	3 mM Zn <sup>2+</sup>	
					1st	2nd
DPPS:DOPC:chol		23.8	23.0	22.7	23.0	51.0
	n=2	± 0.6	± 0.6	± 0.6	± 1.4	± 1.4
DPPC:DOPC:chol		22.0	22.0	22.3	22.5	n/a
	n=3	± 2.1	± 1.8	± 1.2	± 1.1	
DPPC:DOPS:chol		22.1	21.6	21.5	22.2	44.5
	n=2	± 0.6	± 0.4	± 0.1	± 0.2	± 0.7

Table 4-3. Summary of melting temperatures of different vesicle compositions in the presence of  $\text{Zn}^{2+}$  as measured by DSC. All lipid molar ratios were 1:1:1.

The largest drawback of both the SANS and DSC techniques is the high lipid concentration required for sufficient signal. Both require  $\sim 10$  mg/mL lipid, and resulted in PS concentrations around 5 mM. Therefore, to reach saturation, assuming a 2:1 lipid:metal stoichiometry, millimolar amounts of cation was required. It is difficult to make samples with higher concentrations, both experimentally in terms of extruding the vesicles and as it approaches known binding constants of cations to PC. Ideally, lower lipid concentrations would allow to get a wider range of lipid:cation ratio.

## Supplemental Figures

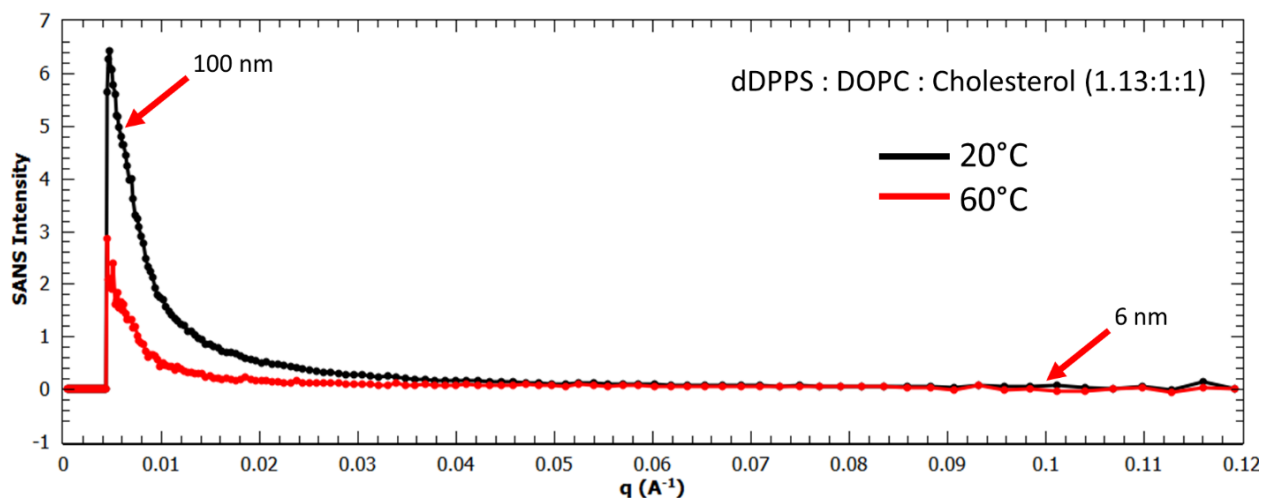


Figure 4-9. SANS data of domains with no metal ions added. The decrease in overall intensity from 20 °C to 60 °C represents the demixing of domains, which results in an SLD designed to match the SLD of the solvent, giving less scattering.

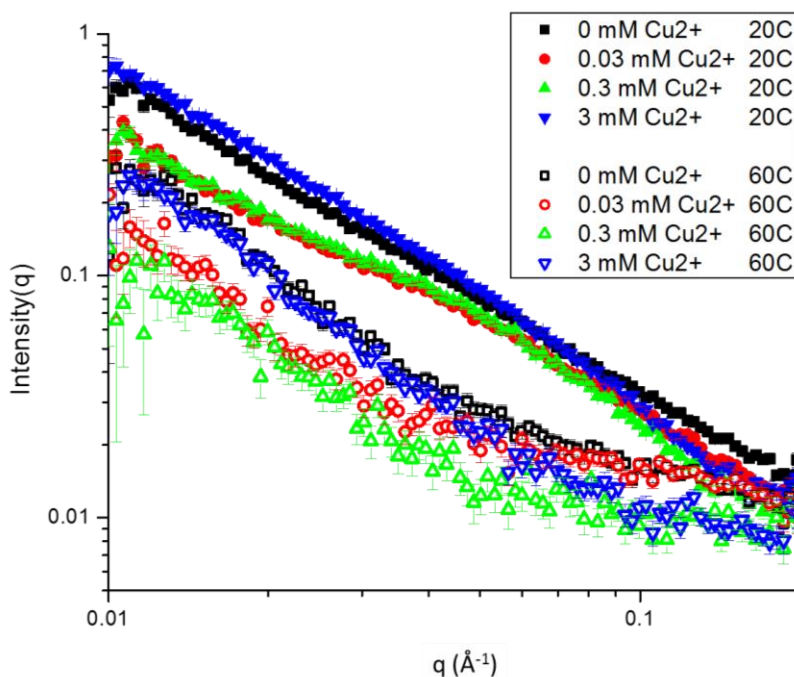


Figure 4-10. SANS data for the  $\text{Cu}^{2+}$  series at both 20 °C and 60 °C, shown with the y-axis in log scale. The leftover scattering shown at 60 °C, at which the domains should be melted and therefore the intensity theoretically 0, is due to experimental error resulting in slight SLD mismatch between the various regions. The subtraction of which is shown in Figure 4-11 below.

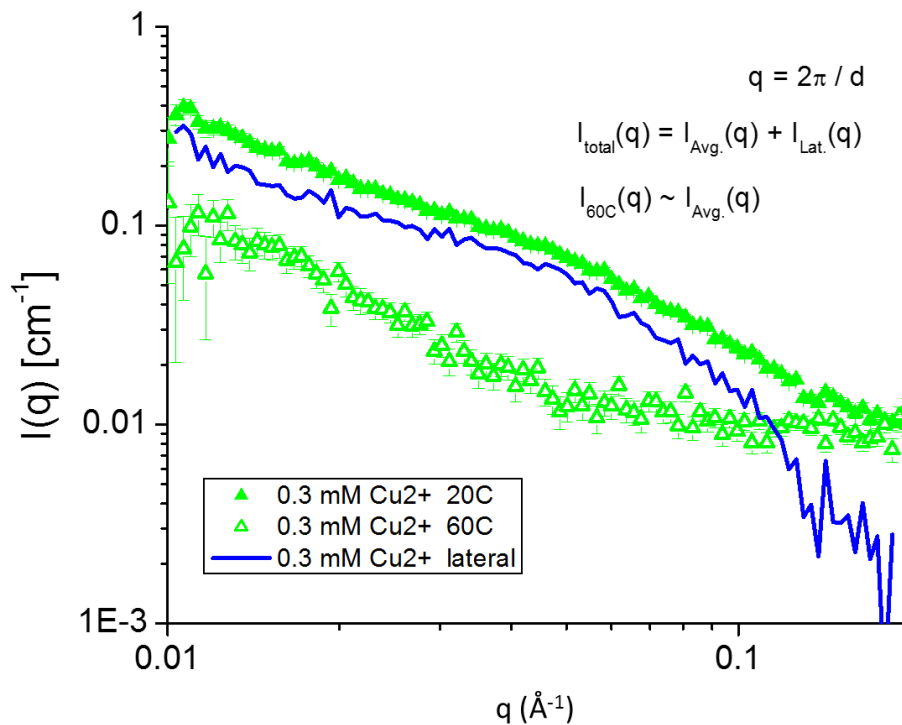


Figure 4-11. Subtraction of the leftover scattering at  $60^\circ\text{C}$  from the total scattering at  $20^\circ\text{C}$  to find the scattering from lateral phase segregation due to domains that are present at  $20^\circ\text{C}$  but not at  $60^\circ\text{C}$ . The resulting data (blue line) is what is plotted in Figure 4-3.

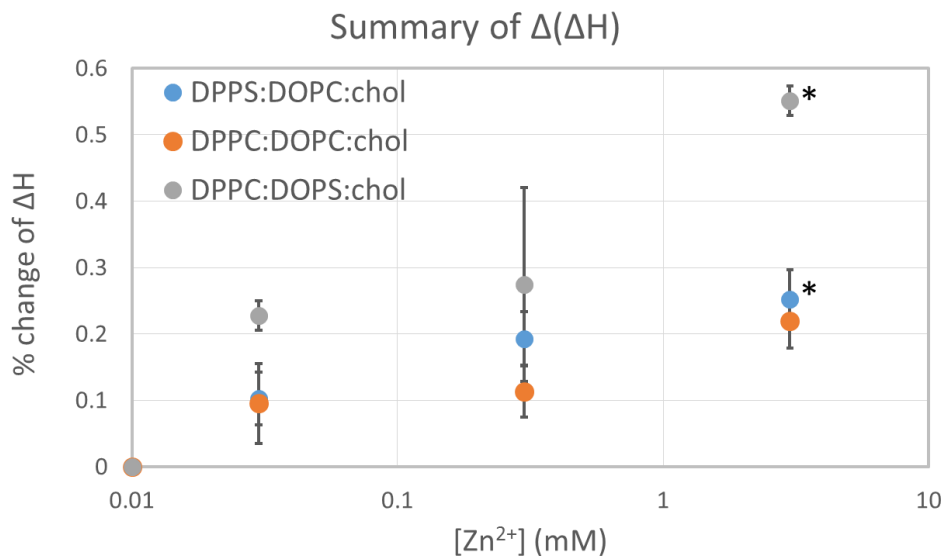


Figure 4-12. Summary of enthalpy data measured by DSC for the three different lipid compositions. All were normalized so that the  $\Delta H$  without divalent cations is equal to  $0$ . The y-axis represents the % increase in  $\Delta H$  that resulted from addition of zinc.

## Chapter 5 Chemotaxis of Small Molecules

### Introduction

Molecular chemotaxis involves the directed motion of a molecule induced by a gradient of an external stimulus. For instance, active enzymes have been shown to chemotax up a concentration gradient of substrate.<sup>90</sup> Here, the enzyme is a molecular motor and the substrate both directs the enzyme and acts as fuel. Though the phenomenon has been observed in various systems, the mechanism is not well understood.<sup>91</sup> Particularly, there has been confusion between chemotaxis and enhanced diffusion. Enhanced diffusion is the increase in diffusion coefficient of an enzyme in the presence of substrate, but the diffusion remains Brownian in nature.<sup>92,93</sup> Separating these two effects would and understanding their distinct mechanisms will improve the implementation of chemotaxis into a variety of potential applications.

Chemotaxis has been demonstrated with catalytic enzymes.<sup>90,94,95</sup> However, it is not clear whether this arises from reaction turnover, conformational changes, or binding and release of substrate and product. Turnover is known to cause enhanced diffusion,<sup>93</sup> although the mechanism of this phenomenon is unknown.<sup>96</sup> A few mechanisms that have been suggested include local or global heating, a chemoacoustic effect, or a conformational change, though no mechanism has been widely accepted yet.<sup>92,96</sup> Enzyme systems that have been explored in this context include catalase/H<sub>2</sub>O<sub>2</sub>,<sup>94</sup> urease/urea,<sup>95</sup> alkaline phosphatase/p-nitrophenylphosphate,<sup>96</sup> and glucose oxidase/glucose,<sup>90</sup> among others. Since the enzyme-substrate systems used demonstrate both enhanced diffusion and chemotaxis, it is not known if one was necessary for the other. In some cases, enhanced diffusion is invoked as a mechanism of chemotaxis, and vice versa.<sup>97</sup>

Towards the goal of elucidating the mechanism, a system was chosen that only involves binding, to remove the complication of enhanced diffusion. Without catalytic turnover or conformational changes, it will be possible to isolate any chemotactic effects of binding alone. The

system chosen uses a zinc porphyrin, which is naturally fluorescent,<sup>98</sup> and can therefore be easily tracked using fluorescence microscopy in microfluidic channels. It binds in a 1:1 fashion with N-containing ligands such as imidazole (Figure 5-1A).<sup>99</sup> The binding has been well established and is known to be labile, with reversible association and dissociation, and the binding constants for imidazole and similar small molecules to the porphyrin are known (typically in the low micromolar range).<sup>100</sup>

Herein, we show that reversible binding between the zinc porphyrin, zinc(II) *meso*-tetra(4-sulfonatophenyl)porphine (ZnTSPP), and N-containing ligands induces chemotaxis but not enhanced diffusion (Figure 5-1B). We make the argument that catalysis is not necessary for chemotaxis, but is required for enhanced diffusion. Further, we can spatially direct the ZnTSPP at will, as well as measure binding constants from the chemotactic motion. This binding-induced chemotaxis should be widely applicable to other systems. We then explore the possibility of using chemotaxis to direct lipid vesicles, but find that there are limitations dependent on the nature of the binding interaction or the size of the chemotaxing species.

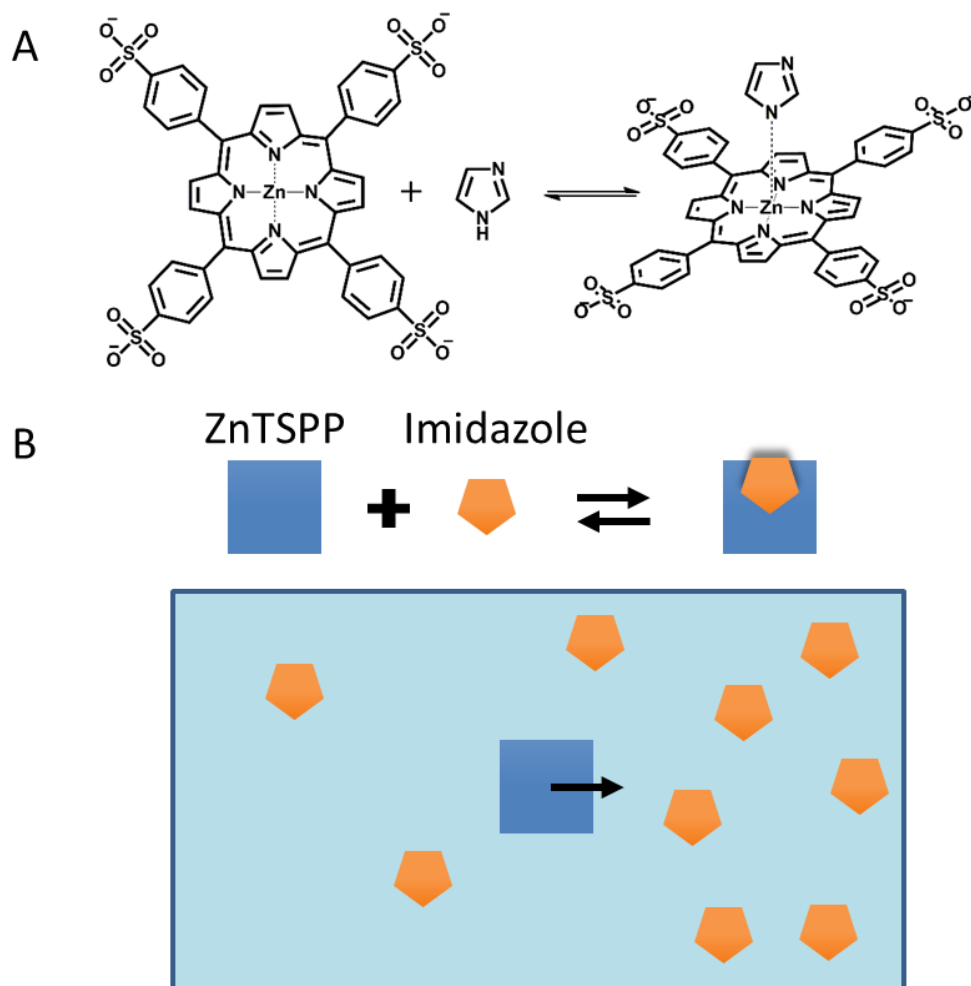


Figure 5-1. Schematic illustration of the reversible binding between ZnTSPP and imidazole inducing chemotaxis. A) Structures of ZnTSPP and imidazole, and the axial ligation. B) Schematic representation of the chemotaxis. An imidazole concentration gradient induces movement of the ZnTSPP up that concentration gradient to maximize binding interactions.

## Materials and Methods

### Materials

Zn(II) *meso*-tetra(4-sulfonatophenyl)porphine tetrasodium salt (ZnTSPP) was purchased from Frontier Scientific, Inc. (Logan, UT). Imidazole, sodium phosphate dibasic, and 2-fluoropyridine were ordered from Sigma–Aldrich Corp. (St. Louis, MO). 1-Methyl- imidazole and

4-aminopyridine were procured from Alfa Aesar Chemicals (Tewksbury, MA). Pyridine and acetonitrile were bought from Honeywell Burdick & Jackson (Muskegon, MI) and OmniSolv, Inc. (Charlotte, NC), respectively. Poly(dimethylsiloxane) (PDMS) was obtained from Dow Corning (Sylgard, silicone elastomer-184).

### Glass Cleaning Preparation

Borosilicate glass from Fisher Scientific was used for all experiments. It was first cleaned in a detergent solution of 1:7 7X (BP Biomedicals) and 18 M $\Omega$  water heated to just below the boiling point. The slides were then removed and rinsed copiously in 18 M $\Omega$  water. The water was then blown off using compressed nitrogen gas. The glass coverslips were then annealed at 530°C for 5 hrs.

### Microfluidic Device Fabrication

Briefly, photolithography was used to pattern a photoresist on a glass slide, which was then etched using HF and cleaned to form a master. Alternatively, the microchannel master was fabricated over a silicon wafer in the Nanofabrication Laboratory of Materials Research Institute, Penn State. PDMS was mixed using 1 part crosslinker to 10 parts monomer, placed under vacuum for 1.5 hrs, poured over the master before being placed in the oven at 55°C overnight. Inlets and outlets for each channel were punched through the PDMS block using a polished needle. The PDMS was attached to the cleaned glass following cleaning in an oxygen plasma cleaner (PDC-32G, Harrick, Pleasantville, NY) for 30 seconds. They were immediately pressed together and then heated for 5 minutes at 100°C.

## Fluorescence Imaging

The collective migration of ZnTSPP compound in response to a gradient of imidazole ligand was characterized using fluorescence imaging. The optical platform consists of an inverted microscope (Nikon Eclipse TE2000–U) with a xenon light source (Lumen Dynamics X–Cite Series 120Q, 100 W). The incident excitation light was focused onto the device via a 10x objective. The background fluorescence was subtracted using MetaMorph software (Universal Imaging), and the maximum intensity was normalized to 1. Fluorescence images were always taken with the channel centered over the CCD, using a series of reference lines to ensure this.

## Vesicle Preparation

Small unilamellar vesicles (SUVs) were made by the freeze-thaw extrusion method.<sup>7,13</sup> 99.5 mol% 1-palmitoyl-2-oleoyl-*sn*-glycero-3-phosphocholine (POPC) was mixed with 0.5 mol% Texas Red 1,2-dihexadecanoyl-*sn*-glycero-3-phosphoethanolamine, triethylammonium salt (Texas Red DHPE) in chloroform, then placed under vacuum for a minimum of 1.5 hrs to remove solvent. The lipid film was then rehydrated in aqueous buffer at pH 7.4 and sonicated for 20 min. They were then subjected to ten freeze-thaw cycles and extruded through a filter with 30 nm or 100 nm pores.

## Microfluidic Experiments

The multiple-inlet microfluidic device was secured over the objective. 1 mg/mL of fibrinogen was introduced to passivate the surface. Plastic tubing was used to introduce the solutions to the device. Solutions were first drawn into a 1 mL plastic syringes and fitted into an automated syringe pump, or in the vesicles experiments, were introduced through gravity flow.

Tubing carried the solutions first to a separate microfluidic device consisting of straight individual channels, designed to slow and even out the flow rate. The solutions then were sent to the multiple-inlet microfluidic device. When solutions were changed, the tubing was unplugged and drained of solution, connected to the syringe full of the new solution (or placed in the container of new solution), and introduced to the throttle device and then the multiple-inlet device. New solutions were allowed to equilibrate over several minutes to ensure a stable flow rate.

## Results

### *Chemotaxis Counteracts Diffusion*

Previous microfluidic experiments were unable to differentiate between chemotaxis and enhanced diffusion.<sup>90,94</sup> To remedy this, experiments were conducted using 3-inlet microfluidic devices. 1 mM of ZnTSPP in buffer (10 mM PBS, pH 7.4) would be introduced into the center inlet, with only buffer introduced in the side inlets (Figure 5-2A). Under laminar flow conditions controlled by a syringe pump (50  $\mu\text{L/hr}$ ), the solutions meet at the junction and flow side by side towards the outlet. There is no direct mixing of the solutions, only lateral Fickian diffusion. The line profile of the fluorescence intensity of the ZnTSPP can be measured perpendicular to the channel, representing the distribution of the ZnTSPP molecules across the channel (Figure 5-2B, black). As the solutions flow through the channel to the outlet (i.e. as time progresses), the line profile broadens (Figure 5-2C, black). Therefore, to separate enhanced diffusion from chemotaxis, 100  $\mu\text{M}$  of imidazole was introduced into the center inlet along with the ZnTSPP. If enhanced diffusion occurred, the line profile at the outlet would be even broader than without imidazole present. Instead, we observed a contraction of the line profile when imidazole was present (Figure

5-2C, red). This is strong evidence for a chemotactic effect. The imidazole is at highest concentration in the center of the channel, and keeps the ZnTSPP from diffusing as far from the center. This experiment represents the first demonstration of bulk chemotaxis without any possibility of enhanced diffusion, catalytic turnover, or significant conformational changes.

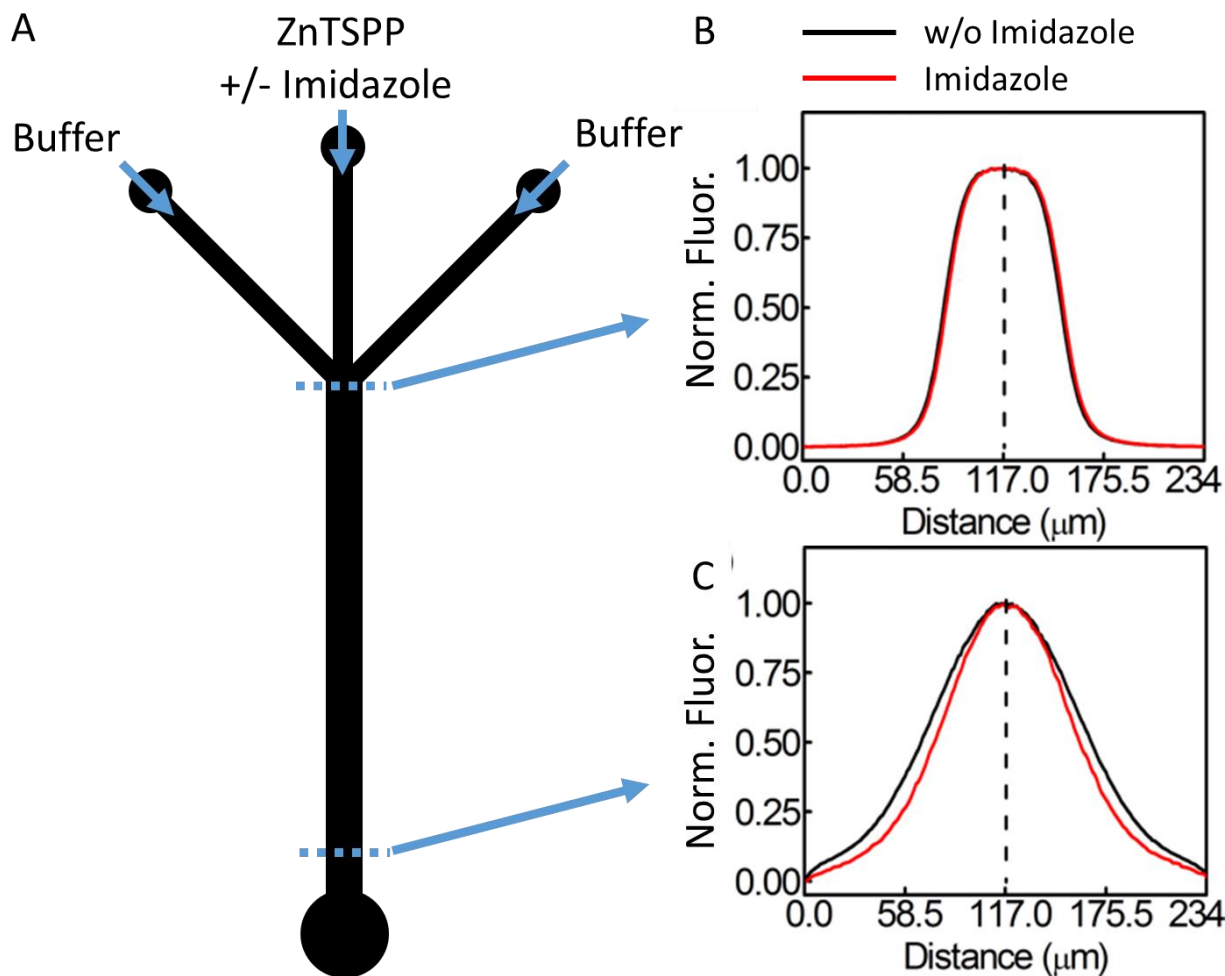


Figure 5-2. Proof of concept experimental setup and results. A) Diagram of three-inlet microfluidic channel. In this experiment, ZnTSPP was introduced into the center channel with or without imidazole. The resulting fluorescence line profiles show the position of the ZnTSPP in the channel, which is 234  $\mu\text{m}$  wide. Dashed line indicates the position of the maximum fluorescence intensity within the channel. B) The initial line profiles with or without imidazole are identical, proving the experimental conditions are kept constant. C) Near the outlet of the channel, the black line profile of the ZnTSPP alone has broadened significantly due to Fickian diffusion. The red line profile shows that in the presence of imidazole, diffusion occurs to a lesser extent, indicating an opposing chemotactic force.

### ***Directed Chemotactic Migration***

In the next set of experiments, the ability of chemotaxis to direct motion was demonstrated. Fluorescent ZnTSPP was again introduced into the center inlet of a three-inlet microfluidic device, and fluorescence line profiles indicating the position of ZnTSPP within the channel were taken near the inlet and outlet of the channel under different side conditions. When buffer is introduced in both side inlets, the line profile shows symmetric broadening between the by the time the ZnTSPP reached the outlet of the channel due to Fickian diffusion of the ZnTSPP (Figure 5-3, black). When imidazole is introduced into one of the side inlets, there is a collective migration of ZnTSPP towards the side imidazole was introduced into (Figure 5-3, red).

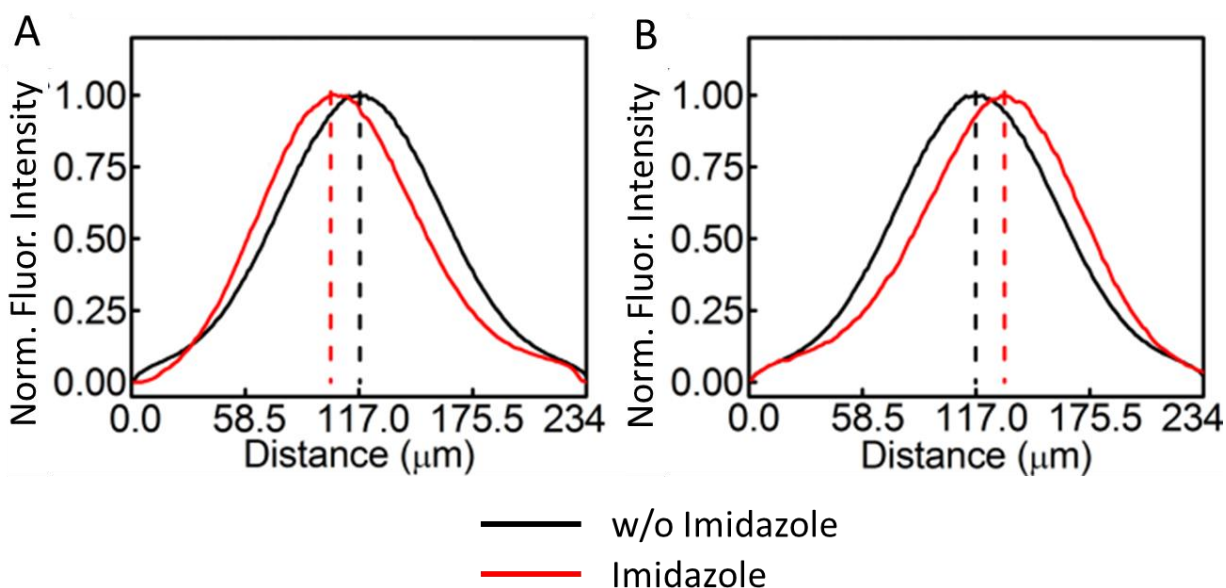


Figure 5-3. Collective migrations of 10  $\mu\text{M}$  ZnTSPP in the presence of 100  $\mu\text{M}$  imidazole. The line profiles are measured near the outlet of the channel. A) Imidazole was introduced into the left inlet, and the ZnTSPP shifts to the left. B) Imidazole was introduced into the right inlet, making ZnTSPP shift to the right.

### Chemotactic Determination of Binding Constants

Using the same setup as described above, it was possible to titrate in increasing concentrations of imidazole into a side inlet and measure the chemotactic shift (Figure 5-4A). The chemotactic shift is defined by the leftward shift of the peak maxima from the original starting position with no imidazole. When plotted against the imidazole concentration, it was possible to fit the chemotactic shift to a Langmuir isotherm and calculate a dissociation constant of 2.2  $\mu\text{M}$  (Figure 5-4B). The binding constant was also confirmed using bulk fluorimetry.

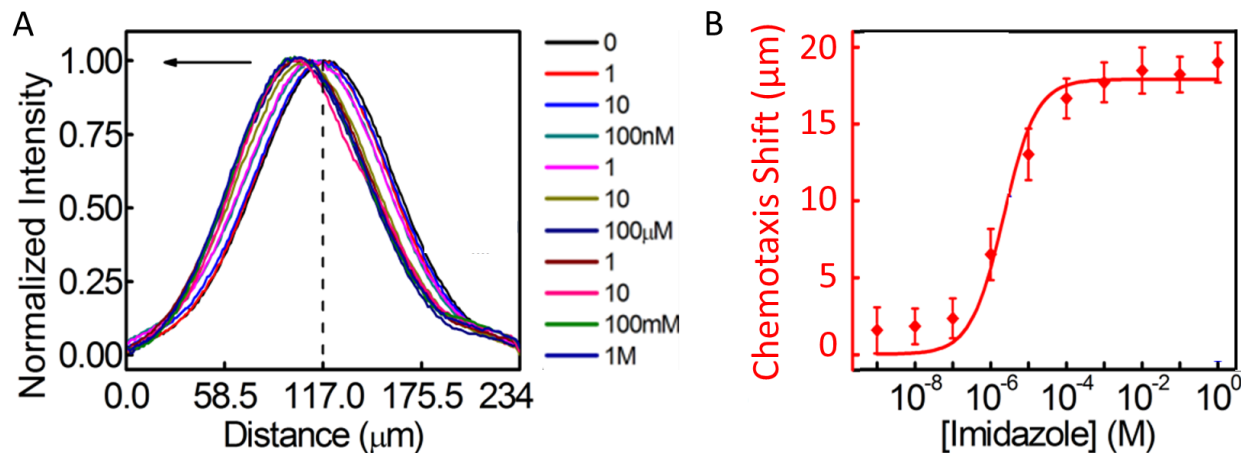


Figure 5-4. A) Plots of mean normalized fluorescence intensity profiles as a function of the lateral position along the width of the channel show shifts for 10  $\mu\text{M}$  ZnTSPP toward increasing concentrations of imidazole. B) Net chemotaxis shift of the peak maxima in A from the center of the channel as a function of the concentration of imidazole. The line is a fit to a Langmuir binding isotherm.

These experiments demonstrate chemotaxis resulting from a labile binding interaction. It is clear that catalysis and enhanced diffusion are not necessary for chemotaxis, but a molecular mechanism for chemotaxis is still not evident. Generic systems based on cosolute binding have been modeled by others,<sup>91</sup> who include a chemotactic force term, sometimes referred to as “cross-diffusion,” which broadly means when the diffusion of the molecule is affected by the presence of

a cosolute. Under these principles, any attractive interaction should lead to chemotaxis. However, it is not clear from one experimental system and the theoretical models what the magnitude of the chemotactic force would be, as well as the physical distance that the molecule would chemotax.

### ***No Chemotaxis Observed with Vesicle-Small Molecule Systems***

In an effort to work towards a drug delivery application, we attempted to demonstrate chemotaxis with a lipid vesicle system. Lipid vesicles are an attractive system for encapsulating drugs because they are biocompatible and easy to customize with different lipids or proteins.<sup>37,38</sup> They also have many known interactions with a range of biomolecules that may be applied for chemotaxis.<sup>16-18</sup> Our lab has done extensive work studying the interactions of small drug molecules such as ibuprofen and tetracaine with phospholipid bilayers.<sup>16</sup> Both ibuprofen, which is negatively charged, and tetracaine, which is positively charged, bind to phosphatidylcholine (PC) bilayers with dissociation constants in the  $\mu\text{M}$  range, although the kinetics of the binding have not been established (Figure 5-5A).<sup>16</sup> In a two-inlet microfluidic device, 30 nm diameter PC vesicles containing 0.5 mol% of a fluorescent-tagged lipid were introduced in the left inlet, and the drug molecule introduced into the right inlet (Figure 5-5B). A two-inlet device was used to simplify experimental setup, despite the fact that either enhanced diffusion or chemotaxis would result in a shifting of the vesicles towards the side with the drug. In fact, no enhanced diffusion was expected as the system only involves binding, and this was confirmed using fluorescence correlation spectroscopy. Therefore, any movement observed in the two-inlet device could be attributed to chemotaxis.

The vesicle-ibuprofen system did not exhibit chemotaxis within the experimental error. The line profiles (Figure 5-5C) show that at a sufficiently slow flow rate (on the order of 1  $\mu\text{L/hr}$ ) the vesicles exhibit Fickian diffusion under buffer conditions (black line scans), evidenced by broadening of the linescan toward the right side of the channel. When 20  $\mu\text{M}$  ibuprofen was introduced, there was no significant change in the line profile (red line scans). As can be seen in Figure 5-5B, the vesicle solution contained large, bright aggregates that could be either clumps of vesicles or dust, leading to the spikes in the plateaus of the line profiles shown in Figure 5-5C. These did not seem to impair the flow or affect the interface where the solutions from the left and right inlets met.

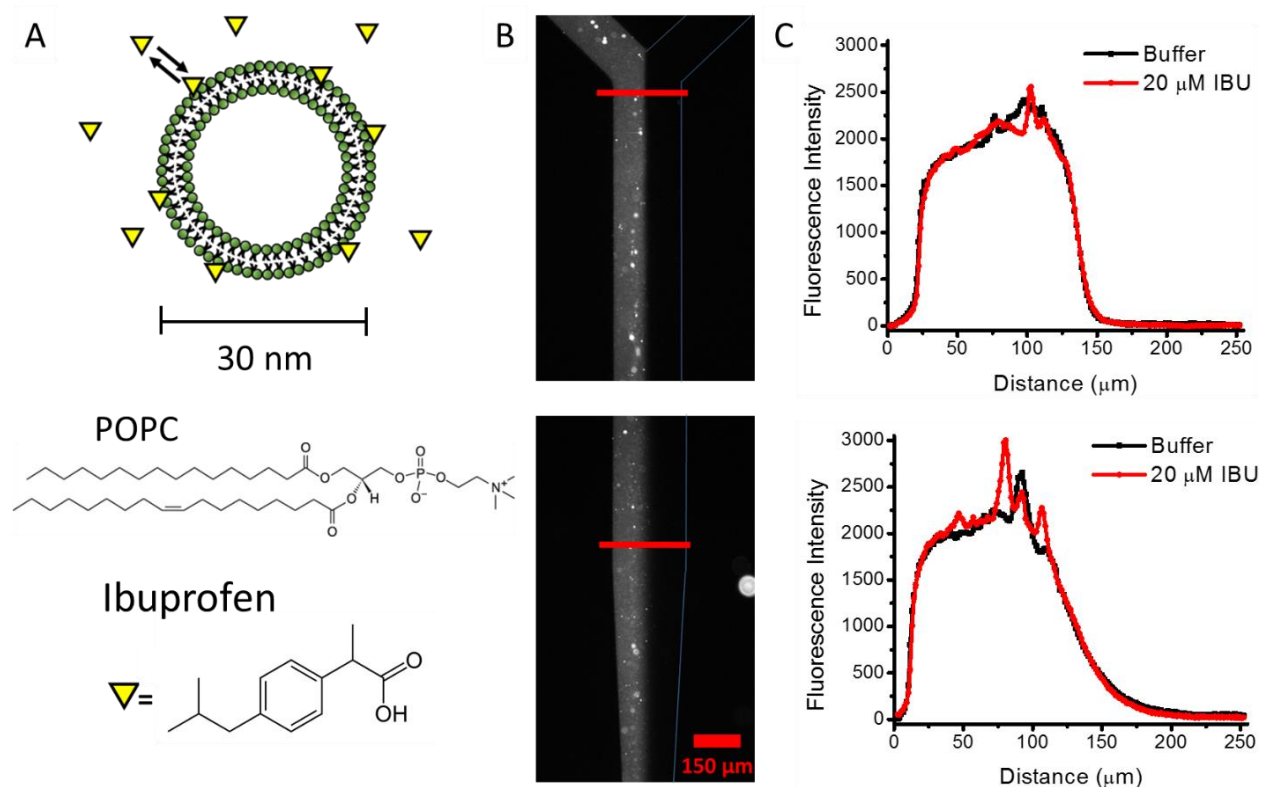


Figure 5-5. Vesicle binding system did not exhibit chemotaxis. A) Schematic illustration of ibuprofen binding to a POPC vesicle. B) Fluorescence images of a two-inlet microfluidic device. Vesicles were introduced into the left inlet, and buffer or ibuprofen was introduced in the right inlet, but did not change the fluorescence. Top. Image taken near the inlets and junction. Bottom. Image taken near the outlet of the channel. C) Fluorescence line profiles taken in the presence and absence of ibuprofen at the position of the red lines drawn in B. Top. Line profiles from near the inlet. Bottom. Line profiles taken near the outlet.

## Discussion

Despite having a favorable binding interaction, the vesicles did not show any chemotaxis. A variety of conditions were employed, including positive (tetracaine) and negative (ibuprofen) small drug molecules, different sizes of vesicles (extruded through 30 nm or 100 nm pores), and concentrations of the drug molecule both near the  $K_D$  ( $\mu\text{M}$ ) and above the  $K_D$  (mM), but none exhibited chemotaxis. While disappointing from the point of view of applications, it provides useful insight into the mechanism. If we assume that in principle, any molecule in a gradient of cosolute experiences a chemotactic force due to an attractive interaction between the molecule and the cosolute,<sup>91</sup> then we can hypothesize what factors modulate that force, such as the size and diffusivity of the molecule, or the lability of binding.

The effect of size is an important consideration. It is important to note that there is less lateral diffusion under buffer conditions for the vesicles than there was for the porphyrin system, even with significantly slower flow rates (it took the ZnTSPP  $\sim 3$  s to flow the length of the channel, and  $\sim 180$  s for the vesicles to travel the same distance). Experimentally, the vesicle experiments were done with gravity flow, rather than a syringe pump, which can make the flow within the device choppy at slow flow rates, and so it was possible to get flow rates  $\sim 60\times$  slower. However, the diffusion coefficient of ZnTSPP was found to be approximately two orders of magnitude higher than the vesicles, compensating for the differences in flow rates. This can be seen when comparing the Fickian diffusion of the ZnTSPP (Figure 5-2B) and vesicles (Figure 5-5C) in the presence of buffer; both show a comparable spreading of the line profile from inlet to outlet. Therefore vesicles did have sufficient time to experience diffusion, but still showed no evidence of a chemotactic force.

The question becomes, does the larger size render the chemotactic force ineffective, or is the chemotactic force generated by the vesicle-ibuprofen interaction less than the force generated by the porphyrin-small molecule binding? Previously, Dey et. al. demonstrated the directed movement of 0.8  $\mu\text{m}$  polystyrene beads decorated with enzymes in the presence of a substrate concentration gradient.<sup>95</sup> The enzyme catalyzed reaction from substrate to product resulted in an enhanced diffusion of the microbeads, and directed movement of the beads. In their setup, the enhanced diffusion and chemotaxis worked together to move the large beads. It would be interesting to try the same experiment with the microbeads decorated with ZnTSPP, to see if the chemotactic force is enough to move them on its own. However, it does suggest that the size of the vesicle itself is not a major factor, and the binding interaction must be the reason no chemotaxis is observed.

The dissociation constants of both binding-only systems are relatively similar, but the kinetics and mode of binding are quite different. The binding of imidazole to ZnTSPP involves the axial ligation of an amine to the zinc center.<sup>98</sup> The formation and breaking of one point of interaction contributes to the lability of the bond, promoting quick association/dissociation kinetics.<sup>99</sup> This is thought to be crucial to chemotaxis, especially when there is only one binding site. The hypothesis is that if probe molecule wants to maximize the energetically favorable binding, then it should move to areas with highest concentration of ligand. For a system with tight, practically irreversible binding, such as a biotin-streptavidin system, no chemotaxis would be expected as the complex would not dissociate under relevant timescales. It follows that even a less tight binding that still demonstrates slow on/off rates would not show appreciable chemotaxis. This is likely the case for the vesicle-ibuprofen system. While we have measured the binding constants of ibuprofen to POPC bilayers, we have not measured the kinetics of the binding. It is

likely that the interaction is slower, as the ibuprofen adsorbs to the surface and then inserts itself into the hydrophobic tail region.<sup>101</sup> Despite the large surface area of the vesicle, offering many potential binding sites for the ibuprofen, the chemotactic driving force generated by the slow binding and unbinding of ibuprofen was insubstantial.

Luckily, in terms of applications we can turn this to our advantage. Just as others have decorated polystyrene beads, we can easily decorate vesicles with enzymes for drug delivery applications.<sup>102</sup> Enzymes can be attached to vesicles using a biotin-streptavidin linker, and the drug of choice can be loaded into the interior of the vesicle.<sup>103</sup> The enzyme-substrate interaction will dominate any small effects from interactions of biomolecules with the vesicle. Therefore the vesicle acts as an inert compartment while the enzymes can be customized to direct the cargo to the desired location.

## Chapter 6 Conclusions

The work presented in this system consists of fundamental research conducted in model systems, but always geared towards potential applications. Model cell membranes such as supported lipid bilayers (SLBs) or vesicles are useful tools, and have allowed our group and others to gain important insight into the individual roles of phospholipids. The tight binding of transition metal ions to lipid head groups has opened up the world of metallomembranes, and the question becomes, what impact do these complexes have? Where might they exist in the body and affect cellular processes? It seems likely that copper bound to the membrane surface would increase lipid oxidation, and further studies on live cells are the next logical step.

This thesis also pushed the limits of the model systems and the available techniques to study them. SLBs have long been considered a two-dimensional fluid, but the tubules arising from the phosphatidylethanolamine (PE) work have pushed into a new dimension. Taken with the domains seen at high mol% PE, it is highly unusual to see such structures in a two component system, much less one that only differs by the methylation of a head group amine. Three dimensional tubules, budding, and other morphology changes in giant unilamellar vesicles have been observed, often under the influence of osmotic pressure<sup>104</sup> or a protein that bends the membrane.<sup>105</sup> To observe tubules in a more simple system presents a new way to study the contributions of individual lipids.

The expansion of small angle neutron scattering (SANS) to more complicated vesicle systems is also exciting. In the past decade, it has been used more frequently to study changes in nanoscopic domains.<sup>32</sup> However, studies have largely focused on changes in lipid tails, keeping phosphatidylcholine (PC) head groups.<sup>77,87,88</sup> The incorporation of a phosphatidylserine (PS) added

experimental challenges. First, the hydrogen/deuterium exchange had to be taken into account, adding another variable to the calculations. Secondly, having a head group region that could laterally segregate to result in regions of different scattering length density (SLD) introduced a lot more contrast to the system. With all PC head groups, the SLD is unaffected by lateral segregation and always matches the solvent, therefore making the tails the only “visible” part of the system. Adding another region that gives contrast made it difficult to recognize from SANS alone whether the binding of  $\text{Cu}^{2+}$  had any effect. In the future, an easier approach to studying head group interactions would be use the same lipid tails for both the PS and PC head groups. By matching the SLD of the tails to the solvent, only changes in the head group region might be observed. This is only one possibility out of many. A recent paper using SANS introduced altered the SLD of live bacteria using isotopic labeling, and were able to detect small lateral features that are consistent with lipid rafts.<sup>106</sup> With the right experimental design, SANS could be a powerful tool for observing nanometer-sized features.

## References

- (1) Fadok, V. A.; Bratton, D. L.; Rose, D. M.; Pearson, A.; Ezekewitz, R. A. B.; Henson, P. M., A receptor for phosphatidylserine-specific clearance of apoptotic cells. *Nature* **2000**, *405* (6782), 85-90.
- (2) Osman, C.; Voelker, D. R.; Langer, T., Making heads or tails of phospholipids in mitochondria. *J. Cell Biol.* **2011**, *192* (1), 7-16.
- (3) Lingwood, D.; Simons, K., Lipid Rafts As a Membrane-Organizing Principle. *Science* **2010**, *327* (5961), 46-50.
- (4) Dowhan, W., Molecular basis for membrane phospholipid diversity: Why are there so many lipids? *Annu. Rev. Biochem.* **1997**, *66*, 199-232.
- (5) Sackmann, E., Supported membranes: Scientific and practical applications. *Science* **1996**, *271* (5245), 43-48.
- (6) Szoka, F.; Papahadjopoulos, D., Comparative Properties and Methods of Preparation of Lipid Vesicles (Liposomes). *Annual Review of Biophysics and Bioengineering* **1980**, *9*, 467-508.
- (7) Mayer, L. D.; Hope, M. J.; Cullis, P. R. Vesicles of variable sizes produced by a rapid extrusion procedure. *Biochim. Biophys. Acta.* **1986**, *858* (1), 161-168.
- (8) Castellana, E. T.; Cremer, P. S., Solid supported lipid bilayers: From biophysical studies to sensor design. *Surf. Sci. Rep.* **2006**, *61* (10), 429-444.
- (9) Cremer, P. S.; Boxer, S. G., Formation and spreading of lipid bilayers on planar glass supports. *J. Phys. Chem. B* **1999**, *103* (13), 2554-2559.
- (10) Winterhalter, M., Black lipid membranes. *Curr. Opin. Colloid Interface Sci.* **2000**, *5* (3-4), 250-255.
- (11) Kaganer, V. M.; Mohwald, H.; Dutta, P., Structure and phase transitions in Langmuir monolayers. *Rev. Mod. Phys.* **1999**, *71* (3), 779-819.
- (12) McConnell, H. M., Structures and Transitions in Lipid Monolayers at the Air-Water Interface. *Annu. Rev. Phys. Chem.* **1991**, *42*, 171-195.
- (13) Hope, M. J.; Bally, M. B.; Webb, G.; Cullis, P. R. Production of large unilamellar vesicles by a rapid extrusion procedure: Characterization of size distribution, trapped volume and ability to maintain a membrane potential. *Biochim. Biophys. Acta.* **1985**, *812* (1), 55-65.

- (14) Monson, C. F.; Cong, X.; Robison, A. D.; Pace, H. P.; Liu, C. M.; Poyton, M. F.; Cremer, P. S., Phosphatidylserine Reversibly Binds Cu<sup>2+</sup> with Extremely High Affinity. *J. Am. Chem. Soc.* **2012**, *134* (18), 7773-7779.
- (15) Cong, X.; Poyton, M. F.; Baxter, A. J.; Pullanchery, S.; Cremer, P. S. Unquenchable Surface Potential Dramatically Enhances Cu<sup>2+</sup> Binding to Phosphatidylserine Lipids. *J. Am. Chem. Soc.* **2015**, *137* (24), 7785-7792.
- (16) Huang, D.; Zhao, T.; Xu, W.; Yang, T. L.; Cremer, P. S., Sensing Small Molecule Interactions with Lipid Membranes by Local pH Modulation. *Anal. Chem.* **2013**, *85* (21), 10240-10248.
- (17) Robison, A. D.; Huang, D.; Jung, H.; Cremer, P. S., Fluorescence modulation sensing of positively and negatively charged proteins on lipid bilayers. *Biointerphases* **2013**, *8*.
- (18) Jung, H.; Robison, A. D.; Cremer, P. S., Detecting Protein-Ligand Binding on Supported Bilayers by Local pH Modulation. *J. Am. Chem. Soc.* **2009**, *131* (3), 1006-1014.
- (19) Holden, M. A.; Jung, S. Y.; Yang, T. L.; Castellana, E. T.; Cremer, P. S., Creating fluid and air-stable solid supported lipid bilayers. *J. Am. Chem. Soc.* **2004**, *126* (21), 6512-6513.
- (20) Yang, T. L.; Baryshnikova, O. K.; Mao, H. B.; Holden, M. A.; Cremer, P. S., Investigations of bivalent antibody binding on fluid-supported phospholipid membranes: The effect of hapten density. *J. Am. Chem. Soc.* **2003**, *125* (16), 4779-4784.
- (21) Boggs, J. M. Lipid intermolecular hydrogen-bonding: influence on structural organization and membrane function. *Biochim. Biophys. Acta.* **1987**, *906* (3), 353-404.
- (22) Tate, M. W.; Eikenberry, E. F.; Turner, D. C.; Shyamsunder, E.; Gruner, S. M. Nonbilayer phases of membrane lipids. *Chem. Phys. Lipids* **1991**, *57* (2-3), 147-164.
- (23) Shoemaker, S. D.; Vanderlick, T. K., Intramembrane electrostatic interactions destabilize lipid vesicles. *Biophys. J.* **2002**, *83* (4), 2007-2014.
- (24) Zhang, C. J.; Sitt, A.; Koo, H. J.; Waynant, K. V.; Hess, H.; Pate, B. D.; Braun, P. V., Autonomic Molecular Transport by Polymer Films Containing Programmed Chemical Potential Gradients. *J. Am. Chem. Soc.* **2015**, *137* (15), 5066-5073.
- (25) Axelrod, D.; Koppel, D. E.; Schlessinger, J.; Elson, E.; Webb, W. W. Mobility Measurement by Analysis of Fluorescence Photobleaching Recovery Kinetics. *Biophys. J.* **1976**, *16* (9), 1055-1069.
- (26) Soumpasis, D. M. Theoretical Analysis of Fluorescence Photobleaching Recovery Experiments. *Biophys. J.* **1983**, *41* (1), 95-97.

- (27) Gordon, S. E.; Senning, E. N.; Aman, T. K.; Zagotta, W. N. Transition metal ion FRET to measure short-range distances at the intracellular surface of the plasma membrane. *J. Gen. Physiol.* **2016**, *147* (2), 189-200.
- (28) Poyton, M. F.; Sendeki, A. M.; Cong, X.; Cremer, P. S. Cu<sup>2+</sup> Binds to Phosphatidylethanolamine and Increases Oxidation in Lipid Membranes. *J. Am. Chem. Soc.* **2016**, *138* (5), 1584-1590.
- (29) Haverstick, D. M.; Glaser, M., Visualization of Ca<sup>2+</sup>-Induced Phospholipid Domains. *Proc. Natl. Acad. Sci. U. S. A.* **1987**, *84* (13), 4475-4479.
- (30) Munro, S., Lipid rafts: Elusive or illusive? *Cell* **2003**, *115* (4), 377-388.
- (31) Veatch, S. L.; Keller, S. L., Separation of liquid phases in giant vesicles of ternary mixtures of phospholipids and cholesterol. *Biophys. J.* **2003**, *85* (5), 3074-3083.
- (32) Pan, J. J.; Heberle, F. A.; Petruzielo, R. S.; Katsaras, J., Using small-angle neutron scattering to detect nanoscopic lipid domains. *Chem. Phys. Lipids* **2013**, *170*, 19-32.
- (33) Shimokawa, N.; Hishida, M.; Seto, H.; Yoshikawa, K., Phase separation of a mixture of charged and neutral lipids on a giant vesicle induced by small cations. *Chem. Phys. Lett.* **2010**, *496* (1-3), 59-63.
- (34) Papahadjopoulos, D.; Portis, A.; Pangborn, W., Calcium-induced lipid phase transitions and membrane fusion. *Annals of the New York Academy of Sciences* **1978**, *308*, 50-66.
- (35) Ross, M.; Steinem, C.; Galla, H. J.; Janshoff, A., Visualization of chemical and physical properties of calcium-induced domains in DPPC/DPPS Langmuir-Blodgett layers. *Langmuir* **2001**, *17* (8), 2437-2445.
- (36) Poyton, M. F.; Pullanchery, S.; Sun, S.; Kusler, K.; Yang, T.; Gagliardi, L.; Cremer, P. S. Manuscript in preparation
- (37) Daniel, S.; Albertorio, F.; Cremer, P. S., Making lipid membranes rough, tough, and ready to hit the road. *MRS Bull.* **2006**, *31* (7), 536-540.
- (38) Allen, T. M.; Cullis, P. R., Liposomal drug delivery systems: From concept to clinical applications. *Adv. Drug Deliv. Rev.* **2013**, *65* (1), 36-48.
- (39) Lindner, L. H.; Eichhorn, M. E.; Eibl, H.; Teichert, N.; Schmitt-Sody, M.; Issels, R. D.; Dellian, M., Novel temperature-sensitive liposomes with prolonged circulation time. *Clin. Cancer Res.* **2004**, *10* (6), 2168-2178.
- (40) Slater, S. J.; Kelly, M. B.; Taddeo, F. J.; Ho, C. J.; Rubin, E.; Stubbs, C. D. The Modulation of Protein Kinase C Activity by Membrane Lipid Bilayer Structure. *J. Biol. Chem.* **1994**, *269* (7), 4866-4871.

- (41) Thurmond, R. L.; Dodd, S. W.; Brown, M. F. Molecular areas of phospholipids as determined by <sup>2</sup>H NMR spectroscopy: Comparison of phosphatidylethanolamines and phosphatidylcholines. *Biophys. J.* **1991**, 59 (1), 108-113.
- (42) Bogdanov, M.; Sun, J. Z.; Kaback, H. R.; Dowhan, W. A Phospholipid Acts as a Chaperone in Assembly of a Membrane Transport Protein. *J. Biol. Chem.* **1996**, 271 (20), 11615-11618.
- (43) Keller, S. L.; Bezrukov, S. M.; Gruner, S. M.; Tate, M. W.; Vodyanoy, I.; Parsegian, V. A. Probability of Alamethicin Conductance States Varies with Nonlamellar Tendency of Bilayer Phospholipids. *Biophys. J.* **1993**, 65 (1), 23-27.
- (44) Vance, J. E. Thematic review series: Glycerolipids. Phosphatidylserine and phosphatidylethanolamine in mammalian cells: two metabolically related aminophospholipids. *J. Lipid Res.* **2008**, 49 (7), 1377-1387.
- (45) Deleault, N. R.; Piro, J. R.; Walsh, D. J.; Wang, F.; Ma, J. Y.; Geoghegan, J. C.; Supattapone, S. Isolation of phosphatidylethanolamine as a solitary cofactor for prion formation in the absence of nucleic acids. *Proc. Natl. Acad. Sci. U. S. A.* **2012**, 109 (22), 8546-8551.
- (46) Morein, S.; Andersson, A. S.; Rilfors, L.; Lindblom, G. Wild-type *Escherichia coli* Cells Regulate the Membrane Lipid Composition in a "Window" between Gel and Non-lamellar Structures. *J. Biol. Chem.* **1996**, 271 (12), 6801-6809.
- (47) van der Does, C.; Swaving, J.; van Klompenburg, W.; Driessen, A. J. M. Non-bilayer Lipids Stimulate the Activity of the Reconstituted Bacterial Protein Translocase. *J. Biol. Chem.* **2000**, 275 (4), 2472-2478.
- (48) Siegel, D. P.; Epand, R. M. The Mechanism of Lamellar-to-Inverted Hexagonal Phase Transitions in Phosphatidylethanolamine: Implications for Membrane Fusion Mechanisms. *Biophys. J.* **1997**, 73 (6), 3089-3111.
- (49) Hamai, C.; Yang, T. L.; Kataoka, S.; Cremer, P. S.; Musser, S. M. Effect of Average Phospholipid Curvature on Supported Bilayer Formation on Glass by Vesicle Fusion. *Biophys. J.* **2006**, 90 (4), 1241-1248.
- (50) Kollmitzer, B.; Heftberger, P.; Rappolt, M.; Pabst, G. Monolayer Spontaneous Curvature of Raft-Forming Membrane Lipids. *Soft Matter* **2013**, 9 (45), 10877-10884.
- (51) Strandberg, E.; Tiltak, D.; Ehni, S.; Wadhwani, P.; Ulrich, A. S. Lipid shape is a key factor for membrane interactions of amphipathic helical peptides. *Biochim. Biophys. Acta-Biomembr.* **2012**, 1818 (7), 1764-1776.
- (52) Sakuma, Y.; Imai, M. From Vesicles to Protocells: The Roles of Amphiphilic Molecules. *Life* **2015**, 5 (1), 651.

- (53) Koynova, R.; Caffrey, M. Phases and phase transitions of the hydrated phosphatidylethanolamines. *Chem. Phys. Lipids* **1994**, *69* (1), 1-34.
- (54) Seddon, J. M.; Cevc, G.; Kaye, R. D.; Marsh, D. X-Ray Diffraction Study of the Polymorphism of Hydrated Diacyl- and Dialkylphosphatidylethanolamines. *Biochemistry* **1984**, *23* (12), 2634-2644.
- (55) Cannon, B.; Hermansson, M.; Gyorke, S.; Somerharju, P.; Virtanen, J. A.; Cheng, K. H. Regulation of Calcium Channel Activity by Lipid Domain Formation in Planar Lipid Bilayers. *Biophys. J.* **2003**, *85* (2), 933-942.
- (56) Bao, P.; Cheetham, M. R.; Roth, J. S.; Blakeston, A. C.; Bushby, R. J.; Evans, S. D. On-Chip Alternating Current Electrophoresis in Supported Lipid Bilayer Membranes. *Anal. Chem.* **2012**, *84* (24), 10702-10707.
- (57) Callan-Jones, A.; Sorre, B.; Bassereau, P. Curvature-Driven Lipid Sorting in Biomembranes. *Cold Spring Harbor Perspect. Biol.* **2011**, *3* (2).
- (58) Irving, H.; Williams, R. J. P. Order of Stability of Metal Complexes. *Nature* **1948**, *162* (4123), 746-747.
- (59) Irving, H.; Williams, R. J. P. The Stability of Transition-metal Complexes. *Journal of the Chemical Society* **1953**, (OCT), 3192-3210.
- (60) Poyton, M. F.; Pullanchery, S.; Butler, P. J.; Cremer, P. S. unpublished results, Pennsylvania State University, 2016
- (61) McLaughlin, A.; Grathwohl, C.; McLaughlin, S. Adsorption of Divalent Cations to Phosphatidylcholine Bilayer Membranes. *Biochimica Et Biophysica Acta* **1978**, *513* (3), 338-357.
- (62) Anglin, T. C.; Conboy, J. C. Kinetics and Thermodynamics of Flip-Flop in Binary Phospholipid Membranes Measured by Sum-Frequency Vibrational Spectroscopy. *Biochemistry* **2009**, *48* (43), 10220-10234.
- (63) Simonsson, L.; Hook, F. Formation and Diffusivity Characterization of Supported Lipid Bilayers with Complex Lipid Compositions. *Langmuir* **2012**, *28* (28), 10528-10533.
- (64) Slater, S. J.; Ho, C.; Taddeo, F. J.; Kelly, M. B.; Stubbs, C. D. Contribution of Hydrogen Bonding to Lipid-Lipid Interactions in Membranes and the Role of Lipid Order: Effects of Cholesterol, Increased Phospholipid Unsaturation, and Ethanol. *Biochemistry* **1993**, *32* (14), 3714-3721.
- (65) Murzyn, K.; Rog, T.; Pasenkiewicz-Gierula, M. Phosphatidylethanolamine-Phosphatidylglycerol Bilayer as a Model of the Inner Bacterial Membrane. *Biophys. J.* **2005**, *88* (2), 1091-1103.

- (66) Jendrasiak, G. L. The hydration of phospholipids and its biological significance. *J. Nutr. Biochem.* **1996**, 7 (11), 599-609.
- (67) Garidel, P.; Blume, A. Miscibility of phosphatidylethanolamine-phosphatidylglycerol mixtures as a function of pH and acyl chain length. *Eur. Biophys. J. Biophys. Lett.* **2000**, 28 (8), 629-638.
- (68) Teixeira, V.; Feio, M. J.; Bastos, M. Role of lipids in the interaction of antimicrobial peptides with membranes. *Progress in Lipid Research* **2012**, 51 (2), 149-177.
- (69) Haney, E. F.; Nathoo, S.; Vogel, H. J.; Prenner, E. J. Induction of non-lamellar lipid phases by antimicrobial peptides: a potential link to mode of action. *Chem. Phys. Lipids* **2010**, 163 (1), 82-93.
- (70) Arouri, A.; Dathe, M.; Blume, A. Peptide induced demixing in PG/PE lipid mixtures: A mechanism for the specificity of antimicrobial peptides towards bacterial membranes? *Biochim. Biophys. Acta-Biomembr.* **2009**, 1788 (3), 650-659.
- (71) Reed, T. T., Lipid peroxidation and neurodegenerative disease. *Free Radic. Biol. Med.* **2011**, 51 (7), 1302-1319.
- (72) Desai, V.; Kaler, S. G., Role of copper in human neurological disorders. *Am. J. Clin. Nutr.* **2008**, 88 (3), 855S-858S.
- (73) Dix, T. A.; Aikens, J., Mechanisms and Biological Relevance of Lipid-Peroxidation Initiation. *Chem. Res. Toxicol.* **1993**, 6 (1), 2-18.
- (74) Bergendi, L.; Benes, L.; Durackova, Z.; Ferencik, M., Chemistry, physiology and pathology of free radicals. *Life Sci.* **1999**, 65 (18-19), 1865-1874.
- (75) Vance, J. E.; Tasseva, G., Formation and function of phosphatidylserine and phosphatidylethanolamine in mammalian cells. *Biochim. Biophys. Acta Mol. Cell Biol. Lipids* **2013**, 1831 (3), 543-554.
- (76) Tsui, F. C.; Ojcius, D. M.; Hubbell, W. L., The intrinsic pKa values for phosphatidylserine and phosphatidylethanolamine in phosphatidylcholine host bilayers. *Biophys. J.* **1986**, 49 (2), 459-468.
- (77) Baumgart, T.; Hunt, G.; Farkas, E. R.; Webb, W. W.; Feigenson, G. W., Fluorescence probe partitioning between L-o/L-d phases in lipid membranes. *Biochim. Biophys. Acta-Biomembr.* **2007**, 1768 (9), 2182-2194.
- (78) Israelachvili, J. N., *Intermolecular and Surface Forces, 3rd Edition*. Elsevier Academic Press Inc: San Diego, 2011; p 1-674.

- (79) Pap, E. H. W.; Drummen, G. P. C.; Winter, V. J.; Kooij, T. W. A.; Rijken, P.; Wirtz, K. W. A.; Op den Kamp, J. A. F.; Hage, W. J.; Post, J. A., Ratio-fluorescence microscopy of lipid oxidation in living cells using C11-BODIPY581/591. *FEBS Lett.* **1999**, 453 (3), 278-282.
- (80) Pham, A. N.; Xing, G. W.; Miller, C. J.; Waite, T. D., Fenton-like copper redox chemistry revisited: Hydrogen peroxide and superoxide mediation of copper-catalyzed oxidant production. *J. Catal.* **2013**, 301, 54-64.
- (81) Gutteridge, J. M. C., Lipid peroxidation initiated by superoxide-dependent hydroxyl radicals using complexed iron and hydrogen peroxide. *FEBS Lett.* **1984**, 172 (2), 245-249.
- (82) MacDonald, M. L.; Murray, I. V. J.; Axelsen, P. H., Mass spectrometric analysis demonstrates that BODIPY 581/591 C11 overestimates and inhibits oxidative lipid damage. *Free Radic. Biol. Med.* **2007**, 42 (9), 1392-1397.
- (83) Maulik, N.; Kagan, V. E.; Tyurin, V. A.; Das, D. K., Redistribution of phosphatidylethanolamine and phosphatidylserine precedes reperfusion-induced apoptosis. *Am. J. Physiol.-Heart Circul. Physiol.* **1998**, 274 (1), H242-H248.
- (84) Nikolettou, V.; Markaki, M.; Palikaras, K.; Tavernarakis, N., Crosstalk between apoptosis, necrosis and autophagy. *Biochim. Biophys. Acta-Mol. Cell Res.* **2013**, 1833 (12), 3448-3459.
- (85) Hayden, C. C.; Hwang, J. S.; Abate, E. A.; Kent, M. S.; Sasaki, D. Y., Directed Formation of Lipid Membrane Microdomains as High Affinity Sites for His-Tagged Proteins. *J. Am. Chem. Soc.* **2009**, 131 (25), 8728-8729.
- (86) Rae, T. D.; Schmidt, P. J.; Pufahl, R. A.; Culotta, V. C.; O'Halloran, T. V., Undetectable intracellular free copper: The requirement of a copper chaperone for superoxide dismutase. *Science* **1999**, 284 (5415), 805-808.
- (87) Heberle, F. A.; Doktorova, M.; Goh, S. L.; Standaert, R. F.; Katsaras, J.; Feigenson, G. W., Hybrid and Nonhybrid Lipids Exert Common Effects on Membrane Raft Size and Morphology. *J. Am. Chem. Soc.* **2013**, 135 (40), 14932-14935.
- (88) Heberle, F. A.; Petruziello, R. S.; Pan, J.; Drazba, P.; Kucerka, N.; Standaert, R. F.; Feigenson, G. W.; Katsaras, J., Bilayer Thickness Mismatch Controls Domain Size in Model Membranes. *J. Am. Chem. Soc.* **2013**, 135 (18), 6853-6859.
- (89) Holopainen, J. M.; Lehtonen, J. Y. A.; Kinnunen, P. K. J., Lipid microdomains in dimyristoylphosphatidylcholine-ceramide liposomes. *Chem. Phys. Lipids* **1997**, 88 (1), 1-13.
- (90) Sengupta, S.; Dey, K. K.; Muddana, H. S.; Tabouillot, T.; Ibele, M. E.; Butler, P. J.; Sen, A., Enzyme Molecules as Nanomotors. *J. Am. Chem. Soc.* **2013**, 135 (4), 1406-1414.

- (91) Schurr, J. M.; Fujimoto, B. S.; Huynh, L.; Chiu, D. T., A Theory of Macromolecular Chemotaxis. *J. Phys. Chem. B* **2013**, *117* (25), 7626-7652.
- (92) Golestanian, R., Enhanced Diffusion of Enzymes that Catalyze Exothermic Reactions. *Phys. Rev. Lett.* **2015**, *115* (10).
- (93) Muddana, H. S.; Sengupta, S.; Mallouk, T. E.; Sen, A.; Butler, P. J., Substrate Catalysis Enhances Single-Enzyme Diffusion. *J. Am. Chem. Soc.* 2010, *132* (7), 2110-2111.
- (94) Dey, K. K.; Das, S.; Poyton, M. F.; Sengupta, S.; Butler, P. J.; Cremer, P. S.; Sen, A., Chemotactic Separation of Enzymes. *ACS Nano* **2014**, *8* (12), 11941-11949.
- (95) Dey, K. K.; Zhao, X.; Tansi, B. M.; Mendez-Ortiz, W. J.; Cordova-Figueroa, U. M.; Golestanian, R.; Sen, A., Micromotors Powered by Enzyme Catalysis. *Nano Lett.* **2015**, *15* (12), 8311-8315.
- (96) Riedel, C.; Gabizon, R.; Wilson, C. A. M.; Hamadani, K.; Tsekouras, K.; Marqusee, S.; Presse, S.; Bustamante, C., The heat released during catalytic turnover enhances the diffusion of an enzyme. *Nature* **2015**, *517* (7533), 227-230.
- (97) Astumian, R. D., Enhanced Diffusion, Chemotaxis, and Pumping by Active Enzymes: Progress toward an Organizing Principle of Molecular Machines. *ACS Nano* **2014**, *8* (12), 11917-11924.
- (98) Ensign, A. A.; Jo, I.; Yildirim, I.; Krauss, T. D.; Bren, K. L., Zinc porphyrin: A fluorescent acceptor in studies of Zn-cytochrome c unfolding by fluorescence resonance energy transfer. *Proc. Natl. Acad. Sci. U. S. A.* **2008**, *105* (31), 10779-10784.
- (99) Mizutani, T.; Wada, K.; Kitagawa, S., Molecular recognition of amines and amino esters by zinc porphyrin receptors: Binding mechanisms and solvent effects. *J. Org. Chem.* **2000**, *65* (19), 6097-6106.
- (100) Simanek, E. E.; Isaacs, L.; Li, X. H.; Wang, C. C. C.; Whitesides, G. M., Self-assembly of zinc porphyrins around the periphery of hydrogen-bonded aggregates that bear imidazole groups. *J. Org. Chem.* **1997**, *62* (26), 8994-9000.
- (101) Simou, S.; Sendekci, A. M.; Pullanchery, S.; Huang, D.; Yang, T.; Cremer, P. S. Manuscript in preparation.
- (102) Kooijmans, S. A. A.; Fliervoet, L. A. L.; van der Meel, R.; Fens, M.; Heijnen, H. F. G.; Henegouwen, P.; Vader, P.; Schiffelers, R. M., PEGylated and targeted extracellular vesicles display enhanced cell specificity and circulation time. *J. Control. Release* **2016**, *224*, 77-85.
- (103) Walker, S. A.; Kennedy, M. T.; Zasadzinski, J. A., Encapsulation of bilayer vesicles by self-assembly. *Nature* **1997**, *387* (6628), 61-64.

- (104) Oglecka, K.; Sanborn, J.; Parikh, A. N.; Kraut, R. S., Osmotic gradients induce bio-reminiscent morphological transformations in giant unilamellar vesicles. *Front. Physiol.* **2012**, *3*.
- (105) Baumgart, T.; Capraro, B. R.; Zhu, C.; Das, S. L., Thermodynamics and Mechanics of Membrane Curvature Generation and Sensing by Proteins and Lipids. *Annual Review of Physical Chemistry*, **2011**; Vol. 62, pp 483-506.
- (106) Nickels, J. D.; Chatterjee, S.; Stanley, C. B.; Qian, S.; Cheng, X.; et al. The in vivo structure of biological membranes and evidence for lipid domains. *PLOS Biology* **2017** *15*(5): e2002214

## VITA

Name: Anne Sendeki

Address: Department of Chemistry  
Pennsylvania State University, 211 South Frear  
University Park, PA, 16802

Email: ams5827@psu.edu

Education: B.S., Chemistry, B.S., Mathematics  
University of Pittsburgh, Pittsburgh, PA, 2012

Ph.D., Chemistry  
Pennsylvania State University, University Park, PA, 2017

### Publications:

**Sendeki, A. M.**; Poyton, M. F.; Baxter, A. J.; Cremer, P. S., Fluid Supported Lipid Bilayers with Phosphatidylethanolamine as the Major Component. (Submitted 2017)

Deng, S.; **Sendeki, A. M.**; Yan, C.; Son, S.; Li, Y.; Yang, T.; Butler, P. J.; Noid, W. G.; Sen, A.; Mallouk, T. E.; Cremer, P. S., Ligand Binding Induces Chemotaxis of Small Molecules. (in preparation)

Poyton, M. F.; **Sendeki, A. M.**; Cong, X.; Cremer, P. S., Cu<sup>2+</sup> Binds to Phosphatidylethanolamine and Increases Oxidation in Lipid Membranes. *J. Am. Chem. Soc.* **2016**, *138* (5), 1584-1590.

Truitt, R.; Hermes, I.; Main, A.; **Sendeki, A.**; Lind, C., Low Temperature Synthesis and Characterization of AlScMo<sub>3</sub>O<sub>12</sub>. *Materials* **2015**, *8* (2), 700-716.

Ricardo, K. B.; **Sendeki, A.**; Liu, H. T., "Surfactant-free exfoliation of graphite in aqueous solutions," *Chem. Comm.* **2014**, 50 (21), 2751-2754